

# Radio Frequency Channel Characterization for Energy Harvesting in Factory Environments

By

**Elijah Adegoke**

A doctoral thesis submitted in partial fulfilment of the requirements  
for the award of a Doctor of Philosophy  
at Loughborough University

5G Research Centre  
Wolfson School of Mechanical, Electrical and Manufacturing Engineering  
Loughborough University

April, 2018

# Certificate of Originality

This is to certify that I am responsible for the work submitted in this thesis, that the original work is my own except as specified in acknowledgements or in footnotes, and that neither the thesis nor the original work contained therein has been submitted to this or any other institution for a degree.

\_\_\_\_\_ (signed)

\_\_\_\_\_ (candidate)

# Abstract

This thesis presents ambient energy data obtained from a measurement campaign carried out at an automobile plant. At the automobile plant, ambient light, ambient temperature and ambient radio frequency were measured during the day time over two days. The measurement results showed that ambient light generated the highest DC power. For plant and operation managers at the automobile plant, the measurement data can be used in system design considerations for future energy harvesting wireless sensor nodes at the plant.

In addition, wideband measurements obtained from a machine workshop are presented in this thesis. The power delay profile of the wireless channel was obtained by using a frequency domain channel sounding technique. The measurements were compared with an equivalent ray tracing model in order to validate the suitability of the commercial propagation software used in this work.

Furthermore, a novel technique for mathematically recreating the time dispersion created by factory inventory in a radio frequency channel is discussed. As a wireless receiver design parameter, delay spread characterizes the amplitude and phase response of the radio channel. In wireless sensor devices, this becomes paramount, as it determines the complexity of the receiver. In reality, it is sometimes difficult to obtain full detail floor plans of factories for deterministic modelling or carry out spot measurements during building construction. As a result, radio provision may be suboptimal. The method presented in this thesis is based on 3-D fractal geometry. By employing the fractal overlaying algorithm presented, metallic objects can be placed on a floor plan so as to obtain similar radio frequency channel effects. The environment created using the fractal approach was used to estimate the amount of energy a harvesting device can accumulate in a University machine workshop space.

# Dedication

Now to him who is able to do exceedingly abundantly above all that we ask or think,  
according to the power that works in us.

# Acknowledgements

I will like to express my sincere gratitude to my supervisors, Dr. Robert Edwards, Dr. William Whittow and Dr. Axel Bindel for their invaluable guidance, advice and knowledge shared throughout this research. I will also like express my thanks to my colleagues (Mr. John Brister, Dr. Dina Al-Saffar, Mr. Zack Wang and Mr. Yu Zeng) at the 5G Research Centre for their assistance during my measurement campaigns.

I am also grateful to the Engineering and Physical Sciences Research Council (EPSRC) and the High Speed Sustainable Manufacturing Institute (HSSMI) who provided the financial support for this research, without this studentship, the work reported in this thesis would not have been possible.

Last but not the least, I would like to thank my parents, brother, and sisters for their support and encouragement throughout the project.

# List of Publications

The original contributions of the work produced in this report is partially supported by the following publications.

## Conference Publications:

- E. I. Adegoke, R. M. Edwards, W. Whittow, and A. Bindel, “RF Power Density Measurements for RF Energy Harvesting in Automobile Factories”, in *Loughborough Antennas and Propagation Conference*, 2015, Loughborough, UK.
- E. I. Adegoke, R. M. Edwards, W. Whittow, A. Bindel and M. Peca, “Opportunities for Energy Harvesting in Automobile Factories”, in *SPIE Smart Structures and Materials + Nondestructive Evaluation and Health Monitoring*, 2016, Las Vegas, USA.
- E. I. Adegoke, R. M. Edwards, W. Whittow, and A. Bindel, “Evaluating 2-D Grid Interpolation Techniques for Predicting Ambient RF Power Density in Automobile Factories”, in *The 10th European Conference on Antennas and Propagation (Eu-CAP)*, 2016, Davos, Switzerland.
- H. Su, R. M. Edwards, E. I. Adegoke;, “Coupled Dipole Antennas for on/off-body Communications at 2.45 GHz”, in *The 11th European Conference on Antennas and Propagation (Eu-CAP)*, 2017, Paris, France.

## Journal Publication:

- E. I. Adegoke, R. M. Edwards, W. Whittow, and A. Bindel, “A Fractal Based Approach for Modelling Delay Spread in Factory Environments”, submitted to *IEEE Transactions on Wireless Communications*, June 2018.

# List of Symbols

$\kappa$	Ray arrival rate ( 1/nsec)
$\varepsilon$	Permittivity (F/m)
$\mu_r$	Relative permeability
$\mu_o$	Permeability of free space $4\pi \times 10^{-7}$ (H/m)
$\sigma$	Conductivity (S/m)
$X_{\vartheta}$	Gaussian distributed random variable
$\lambda$	Wavelength (m)
$f_m$	Maximum Doppler shift (Hz)
$f_d$	Doppler shift (Hz)
$f$	Frequency (MHz)
$c$	Speed of light (m/s)
$\eta_{PV}$	Efficiency of a PV cell
$\eta_{RF-DC}$	RF-DC conversion efficiency
$\Lambda$	Cluster arrival rate (1/nsec)
$\Gamma$	Cluster decay constant
$\gamma$	Ray decay constant
$\varphi_r$	Radial basis function
$\gamma(h)$	Semivariance
$\Delta F$	Frequency shift
$\tau_{max}$	Maximum detectable delay
$t_{\eta}$	Maximum excess delay
$\tau_{rms}$	RMS delay spread

# List of Acronyms

3-D	Three-dimensional
4G	Fourth generation
5G	Fifth generation
AC	Alternating current
AF	Antenna factor
AFD	Average fade duration
AoA	Angle of arrival
AP	Access Point
APDP	Average power delay profile
$B_c$	Coherent bandwidth
BER	Bit error rate
CAD	Computer-aided design
CDF	Cumulative distribution function
CIR	Channel impulse response
COST	The european co-operative for scientific and technical research
COTS	Commercial off-the-shelf
CPS	Cyber-physical systems
CTF	Channel transfer function
DAQ	Data acquisition device
DC	Direct current
DSO	Digital storage oscilloscope
DSSC	Dye-sensitized solar cells
EIRP	Equivalent isotropically radiated power
EM	Electromagnetic



FAF	Floor attenuation factor
FDM	Frequency division multiplexing
GIS	Geographic information systems
GSM	Global system for mobile communications
HVAC	Heating, ventilating and air-conditioning
IDW	Inverse distance weighting
IF	Intermediate frequency
LAN	Local area network
LCR	Level-crossing rate
LoS	Line-of-sight
MAC	Media access control
MAPE	Mean absolute percentage error
MCU	Microcontroller unit
MIMO	Multiple-input multiple-output
MPC	Multipath component
NLoS	Non Line-of-sight
OFDM	Orthogonal frequency division multiplexing
PC	Personal computer
PDP	Power delay profile
PEC	Perfect electrical conductor
PHY	Physical layer
PMM	Power management module
PN	Pseudo-noise
PV	Photovoltaic
RAT	Radio access technologies
RBF	Radial basis function
RBW	Resolution bandwidth
RF	Radio frequency
RFEH	Radio frequency energy harvester
RFID	Radio frequency identification
RGB	Red, green, blue

SBR	Shooting bouncing ray
SNR	Signal-to-noise ratio
SV	Saleh-Valenzuela
TEG	Thermoelectric generators
$T_x \rightarrow R_x$	Transmitter-Receiver
ULA	Uniform linear array
ULP	Ultra-low power
URA	Uniform rectangular array
UTD	Uniform theory of diffraction
UWB	Ultra wideband
VEH	Vibration energy harvester
VNA	Vector network analyser
WSN	Wireless sensor nodes

# List of Figures

1.1	Resonant coupling (non-radiative). . . . .	6
1.2	Radiative RF power transfer system. The dashed box is widely known as a rectenna. . . . .	6
2.1	Wireless communication channel [33]. . . . .	13
2.2	Illustration of the 802.15.4a UWB channel model for 2 - 10 GHz. . . .	14
2.3	Illustration of constructive and destructive interference [35]. . . . .	15
2.4	Illustration of large-scale and small-scale fading effects versus distance. Path loss and shadowing account for large-scale effects, while multipath accounts for small-scale effects [31]. . . . .	15
2.5	A Rayleigh signal envelope at 900 MHz. . . . .	23
2.6	Saleh-Valenzuela channel impulse response model. The visually identified clusters are represented with red solid lines with corresponding decay rate ( $\gamma$ ), and the envelope decay constant ( $\Gamma$ ) is represented by the dashed solid line. . . . .	24
2.7	The shooting and bouncing ray (SBR) launching schematic. W1 and W2 are arbitrary reflecting surfaces. [57]. . . . .	25
2.8	Image ray tracing method. . . . .	26
3.1	SP Lite pyranometer [84]. This device was used to obtain irradiance values at the DEP. . . . .	34
3.2	Squirrel SQ2020-2F16 data logger [85]. This device was used to log data from the pyranometer. . . . .	35

3.3	Irradiance measurement at a center location at the automobile plant. This measurement was taken between 10:45 AM and 3:30 PM. The Figure shows irradiance values with interruptions excluded. . . . .	36
3.4	Second Irradiance measurement at the automobile plant. This measurement was taken between 11:00 AM and 5:00 PM. The Figure shows irradiance values with interruptions excluded. . . . .	36
3.5	Calex PYROPEN-E infrared thermometer [87]. . . . .	37
3.6	Input RF power density measurement setup at the DEP. . . . .	40
3.7	Sketch of RF power density measurement points at the automobile factory.	41
3.8	Input RF Power density at Location 1 at the DEP. This result shows the vector combination of horizontal and vertical polarization for average and max-hold modes. . . . .	43
3.9	Input RF Power density at Location 2 at the DEP. This result shows the vector combination of horizontal and vertical polarization for average and max-hold modes. . . . .	43
3.10	Input RF Power density at Location 3 at the DEP. This result shows the vector combination of horizontal and vertical polarization for average and max-hold modes. . . . .	44
3.11	Input RF Power density at Location 4 at the DEP. This result shows the vector combination of horizontal and vertical polarization for average and max-hold modes. . . . .	44
3.12	Input RF Power density at Location 5 at the DEP. This result shows the vector combination of horizontal and vertical polarization for average and max-hold modes. . . . .	45
4.1	Three-dimensional visualisation of direct, reflected and diffracted rays in a LoS setup from $T_x$ (blue) to $R_x$ (red). . . . .	52
4.2	Direct RF pulse time domain channel sounding measurement system. .	53
4.3	Sliding correlator channel sounding measurement system. . . . .	55
4.4	Frequency domain channel sounding measurement system. . . . .	56
4.5	Channel measurement system block diagram. . . . .	57

4.6	Pictorial illustration of the channel measurement setup for a LoS point. .	58
4.7	Loughborough University Machine Workshop Layout. The floor plan shows the transmitter and receiver locations. The six LoS and NLoS receiver locations are represented as $L_i$ and $N_i$ . . . . .	60
4.8	Top view of Loughborough University machine workshop ray tracing model. In the figure, blue objects are defined as PEC, brown objects are defined as wood and the yellow line represents a glass partition. . . . .	61
4.9	RMS delay spread as a function of distance for all VNA measurement and ray tracing simulations. . . . .	64
5.1	A Sierpinski carpet after four iterations [140]. . . . .	67
5.2	A Sierpinski triangle after four iterations [141]. . . . .	68
5.3	A Cantor set after five iterations [142]. . . . .	68
5.4	Clemson University Machine Workshop adapted from [139]. Blue objects represent PEC and wooden objects are coloured in brown. . . . .	70
5.5	a) Clemson University Sierpinski square fractal layout for 9m cell, b) Clemson University Sierpinski square fractal overlay for 9m, 10m and 11m cells. The red dots are receivers and green dots are transmitters. . .	71
5.6	a) Clemson University Sierpinski triangle fractal layout for 9 m cell, b) Clemson University Sierpinski triangle fractal overlay for 9 m, 10 m and 11 m cells. . . . .	72
5.7	Loughborough University Cantor set fractal overlay layout. Due to the pattern of the Cantor set, objects for different cell sizes overlap. . . . .	73
5.8	Transmitter and receiver locations used for fractal APDP analysis on the Loughborough University workshop floor plan. . . . .	73
5.9	Virtual antenna array setup. . . . .	74
5.10	Simulation of delay spread CDF at 2.4 GHz using Cantor set and Sierpinski triangle fractal overlays a) NLoS b) LoS. All objects in the simulation were PEC. . . . .	76

5.11	Simulation of NLoS delay spread CDF using Sierpinski square fractal overlay and overlay mixture. a) Clemson University workshop and b) Loughborough University workshop. . . . .	77
5.12	Simulation of LoS delay spread CDF using Sierpinski square fractal overlay and overlay mixture. a) Clemson University workshop and b) Loughborough University workshop. . . . .	78
5.13	Simulation of NLoS delay spread CDF using Triangular objects fractal overlay and overlay mixture. a) Clemson University workshop and b) Loughborough University workshop. . . . .	80
5.14	Simulation of LoS delay spread CDF using Triangular objects fractal overlay and overlay mixture. a) Clemson University workshop and b) Loughborough University workshop. . . . .	81
6.1	Illustration of semivariance pairing using coloured points [170]. . . . .	90
6.2	Comparison of IDW, Kriging, RBF with the measured value at DEP (Location 1). . . . .	93
6.3	Comparison of IDW, Kriging, RBF with the measured value at DEP (Location 2). . . . .	93
6.4	Comparison of IDW, Kriging, RBF with the measured value at DEP (Location 3). . . . .	94
6.5	Comparison of IDW, Kriging, RBF with the measured value at DEP (Location 4). . . . .	94
6.6	Comparison of IDW, Kriging, RBF with the measured value at DEP (Location 5). . . . .	95
6.7	Depiction of conceptual paths on the DEP rectangular floor plan. . . . .	98
6.8	Received power distribution for Loughborough University workshop (XY grid). The blue shapes indicate the top view of the machines in the deterministic model . . . . .	100
6.9	Scenario 2 use case energy path profile. . . . .	100
A.1	Irradiance measurement at HSSMI main office . . . . .	130
A.2	Irradiance measurement at 5GRC, Loughborough University . . . . .	131

B.1	Horizontal and vertical polarization measurements for average mode at the DEP (Location 1) . . . . .	132
B.2	Horizontal and vertical polarization measurements for max-hold at the DEP (Location 1) . . . . .	133
B.3	Horizontal and vertical polarization measurements for average mode at the DEP (Location 2) . . . . .	133
B.4	Horizontal and vertical polarization measurements for max-hold at the DEP (Location 2) . . . . .	134
B.5	Horizontal and vertical polarization measurements for average mode at the DEP (Location 3) . . . . .	134
B.6	Horizontal and vertical polarization measurements for max-hold at the DEP (Location 3) . . . . .	135
B.7	Horizontal and vertical polarization measurements for average mode at the DEP (Location 4) . . . . .	135
B.8	Horizontal and vertical polarization measurements for max-hold at the DEP (Location 4) . . . . .	136
B.9	Horizontal and vertical polarization measurements for average mode at the DEP (Location 5) . . . . .	136
B.10	Horizontal and vertical polarization measurements for max-hold at the DEP (Location 5) . . . . .	137
B.11	Horizontal and vertical polarization measurements for average mode at CEME reception . . . . .	138
B.12	Horizontal and vertical polarization measurements for max-hold at CEME reception . . . . .	138
B.13	Horizontal and vertical polarization measurements for average mode at CEME reception . . . . .	139
B.14	Horizontal and vertical polarization measurements for max-hold at CEME reception . . . . .	139
C.1	Frequency vs dB loss for 3 m MW cable . . . . .	141
C.2	Frequency vs dB loss for 13 m MW cable . . . . .	141

C.3	Frequency vs dB loss for 20 m MW cable . . . . .	142
E.1	Measurement power delay profile at receiver location $L_1$ . . . . .	144
E.2	Ray tracing profile at receiver location $L_1$ . . . . .	145
E.3	Measurement power delay profile at receiver location $L_2$ . . . . .	145
E.4	Ray tracing profile at receiver location $L_2$ . . . . .	146
E.5	Measurement power delay profile at receiver location $L_3$ . . . . .	146
E.6	Ray tracing profile at receiver location $L_3$ . . . . .	147
E.7	Measurement power delay profile at receiver location $L_4$ . . . . .	147
E.8	Ray tracing profile at receiver location $L_4$ . . . . .	148
E.9	Measurement power delay profile at receiver location $L_5$ . . . . .	148
E.10	Ray tracing profile at receiver location $L_5$ . . . . .	149
E.11	Measurement power delay profile at receiver location $L_6$ . . . . .	149
E.12	Ray tracing profile at receiver location $L_6$ . . . . .	150
E.13	Measurement power delay profile at receiver location $N_1$ . . . . .	150
E.14	Ray tracing profile at receiver location $N_1$ . . . . .	151
E.15	Measurement power delay profile at receiver location $N_2$ . . . . .	151
E.16	Ray tracing profile at receiver location $N_2$ . . . . .	152
E.17	Measurement power delay profile at receiver location $N_3$ . . . . .	152
E.18	Ray tracing profile at receiver location $N_3$ . . . . .	153
E.19	Measurement power delay profile at receiver location $N_4$ . . . . .	153
E.20	Ray tracing profile at receiver location $N_4$ . . . . .	154
E.21	Measurement power delay profile at receiver location $N_5$ . . . . .	154
E.22	Ray tracing profile at receiver location $N_5$ . . . . .	155
E.23	Measurement power delay profile at receiver location $N_6$ . . . . .	155
E.24	Ray tracing profile at receiver location $N_6$ . . . . .	156
F.1	APDP at receiver location 1 (2.4 GHz). . . . .	158
F.2	APDP at receiver location 2 (2.4 GHz). . . . .	158
F.3	APDP at receiver location 3 (2.4 GHz). . . . .	159
F.4	APDP at receiver location 4 (2.4 GHz). . . . .	159
F.5	APDP at receiver location 5 (2.4 GHz). . . . .	160



F.6	APDP at receiver location 6 (2.4 GHz).	160
F.7	APDP at receiver location 7 (2.4 GHz).	161
F.8	APDP at receiver location 8 (2.4 GHz).	161
F.9	APDP at receiver location 9 (2.4 GHz).	162
F.10	APDP at receiver location 10 (2.4 GHz).	162
F.11	APDP at receiver location 1 (60 GHz).	163
F.12	APDP at receiver location 2 (60 GHz).	163
F.13	APDP at receiver location 3 (60 GHz).	164
F.14	APDP at receiver location 4 (60 GHz).	164
F.15	APDP at receiver location 5 (60 GHz).	165
F.16	APDP at receiver location 6 (60 GHz).	165
F.17	APDP at receiver location 7 (60 GHz).	166
F.18	APDP at receiver location 8 (60 GHz).	166
F.19	APDP at receiver location 9 (60 GHz).	167
F.20	APDP at receiver location 10 (60 GHz).	167

# List of Tables

3.1	Summary of temperature measurements at the DEP . . . . .	38
3.2	Comparison of maximum indoor RF power density levels at the DEP . .	41
3.3	Banded Input RF Power density at Location 1 . . . . .	46
3.4	Banded Input RF Power density at Location 2 . . . . .	46
3.5	Banded Input RF Power density at Location 3 . . . . .	46
3.6	Banded Input RF Power density at Location 4 . . . . .	47
3.7	Banded Input RF Power density at Location 5 . . . . .	47
4.1	Measurement setup parameters . . . . .	58
4.2	Link budget for the frequency domain channel sounder. A 13 m MW cable is connected to the receiver and a 3 m MW cable is connected to the transmitter . . . . .	59
4.3	Ray tracing model parameters . . . . .	61
4.4	Comparison of rms delay spread obtained from VNA and ray tracing model	63
4.5	Error measure comparison for measurement and ray tracing prediction .	63
5.1	Summary of mean RMS delay spread, standard deviation and maximum at 2.4 GHz and 60 GHz for the fractal overlay combinations used at Clemson University model and Loughborough University workshops. Triangular objects in the Sierpinski square layout are represented as TO	82
5.2	Summary of receiver point classification using Loughborough and Clem- son University models . . . . .	83
5.3	S-V Channel parameters from Loughborough University machine work- shop at 2.4 and 60 GHz . . . . .	84

5.4	Fractal overlay (Triangular solids) and S-V model delay spread comparison for Loughborough University machine workshop . . . . .	84
6.1	Features of interpolation techniques adopted [164] . . . . .	88
6.2	MAPE comparison of interpolated values for RATs at the DEP . . . . .	95
6.3	MAPE performance comparison of the spatial interpolation methods used in predicting XY grid receiver power in the LU workshop model (2.4 GHz)	96
6.4	Summary of energy profile a pallet travelling a conceptual path at the DEP at 2.4 GHz . . . . .	98
6.5	XY received power grid for Loughborough University workshop using IDW ( $p = 2$ ). The grid shows 16 by 10 grid points which represent the receiver locations in the deterministic model . . . . .	101
6.6	XY received power grid for Loughborough University workshop using kriging Gaussian. The grid shows 16 by 10 grid points which represent the receiver locations in the deterministic model . . . . .	101
6.7	XY received power grid for Loughborough University workshop using RBF Gaussian. The grid shows 16 by 10 grid points which represent the receiver locations in the deterministic model . . . . .	101
C.1	Electro-Metrics EM6116 . . . . .	140
D.1	Workshop inventory . . . . .	143

# Contents

<b>Certificate of Originality</b>	<b>i</b>
<b>Abstract</b>	<b>ii</b>
<b>Dedication</b>	<b>iii</b>
<b>Acknowledgements</b>	<b>iv</b>
<b>List of Publications</b>	<b>v</b>
<b>List of Symbols</b>	<b>v</b>
<b>List of Acronyms</b>	<b>vii</b>
<b>List of Figures</b>	<b>ix</b>
<b>List of Tables</b>	<b>xvi</b>
<b>1 Energy Harvesting for Low-power Devices</b>	<b>1</b>
1.1 Internet of Things for Industry . . . . .	1
1.2 Energy Harvesting Techniques . . . . .	3
1.2.1 Ambient Vibration Energy Harvesting . . . . .	4
1.2.2 Ambient Light Energy Harvesting . . . . .	4
1.2.3 Ambient Temperature Energy Harvesting . . . . .	5
1.2.4 Ambient Radio frequency Energy Harvesting . . . . .	5
1.3 Co-located Energy Harvesters . . . . .	7
1.4 Research Motivation . . . . .	8
1.5 Research Contribution . . . . .	8

1.6	Organisation of this thesis . . . . .	9
<b>2</b>	<b>The Industrial Wireless Channel</b>	<b>11</b>
2.1	Introduction . . . . .	12
2.2	Characterizing the Wireless Channel . . . . .	14
2.3	Multipath Fading in Wireless Communication . . . . .	16
2.3.1	Flat Fading . . . . .	17
2.3.2	Frequency Selective Fading . . . . .	17
2.3.3	Fast Fading . . . . .	17
2.3.4	Slow Fading . . . . .	17
2.4	Narrowband Channel Characteristics . . . . .	18
2.4.1	Theoretical Methods (Narrowband) . . . . .	18
2.4.2	Measurement-based Stochastic Models (Narrowband) . . . . .	19
2.5	Wideband Channel Characteristics . . . . .	21
2.5.1	Stochastic Wideband Models . . . . .	22
2.5.2	Measurement-based Stochastic Models (Wideband) . . . . .	23
2.6	Ray Tracing for Wireless Channel Characteristics . . . . .	24
2.6.1	Basic Ray Tracing Algorithms . . . . .	25
2.6.2	Evaluating Wireless Channel Characteristics . . . . .	26
2.7	Summary . . . . .	27
<b>3</b>	<b>Ambient Energy Characterisation</b>	<b>29</b>
3.1	Introduction . . . . .	30
3.2	Ambient Light Measurements . . . . .	34
3.2.1	Methodology and Instrumentation (Ambient Light) . . . . .	34
3.2.2	Measurement Campaign Results (Ambient Light) . . . . .	35
3.3	Ambient Temperature Measurements . . . . .	37
3.3.1	Ambient Temperature Measurement Procedure . . . . .	37
3.3.2	Measurement Campaign Results (Ambient Temperature) . . . . .	37
3.4	Ambient Radio Frequency Measurements . . . . .	38
3.4.1	Radio Frequency Measurement Procedure . . . . .	38
3.4.2	Radio Frequency Measurement Campaign Results . . . . .	40

3.5	Summary . . . . .	47
<b>4</b>	<b>Wideband Channel Measurement</b>	<b>49</b>
4.1	Introduction . . . . .	50
4.2	Channel Sounding Techniques . . . . .	52
4.2.1	Direct RF Pulse (Time Domain) Channel Sounding . . . . .	53
4.2.2	Spread spectrum Channel Sounding . . . . .	53
4.2.3	Frequency Domain Channel Sounding . . . . .	54
4.3	Wireless Channel Measurement System . . . . .	56
4.4	Measurement Environment and Procedure . . . . .	59
4.5	Machine Workshop Ray Tracing Model . . . . .	60
4.6	Measurement Results and Ray Tracing Comparison . . . . .	62
4.7	Summary . . . . .	64
<b>5</b>	<b>Fractal Based Radio Propagation Modelling</b>	<b>65</b>
5.1	Introduction . . . . .	66
5.2	2-Dimensional Fractals . . . . .	67
5.3	Fractal Based Modelling . . . . .	68
5.4	Fractal Overlay Statistical Features . . . . .	74
5.5	Time Dispersion Prediction Using Fractal Overlays . . . . .	75
5.6	Validation of Fractal Overlay Model . . . . .	83
5.7	Summary . . . . .	84
<b>6</b>	<b>Predicting Received Power and Energy Profiles Using 2-D Interpolation</b>	<b>85</b>
6.1	Introduction . . . . .	86
6.2	2-D Grid Interpolation Techniques . . . . .	87
6.2.1	Inverse Distance Weighting . . . . .	88
6.2.2	Radial Basis Function . . . . .	89
6.2.3	Kriging . . . . .	90
6.3	Evaluating Interpolation Techniques in Multipath Rich Environments . .	92
6.3.1	Evaluating Interpolation Techniques at Dagenham Engine Plant	92

6.3.2	Evaluating Interpolation Techniques at Loughborough University workshop . . . . .	95
6.4	Estimating Ambient Energy Profiles Using Interpolated Grids . . . . .	96
6.4.1	Predicting Energy Profiles at Dagenham Engine Plant . . . . .	98
6.4.2	Predicting Energy Profiles at Loughborough University workshop	99
6.5	Summary . . . . .	102
<b>7</b>	<b>Conclusions and Future Work</b>	<b>103</b>
7.1	Summary of Research Novelty . . . . .	103
7.2	Industrial Applications . . . . .	104
7.3	Suggestions for Future Work . . . . .	104
	References . . . . .	106
	<b>References</b>	<b>106</b>
	<b>Appendices</b>	<b>128</b>
<b>A</b>	<b>Irradiance Measurements at HSSMI and 5GRC</b>	<b>129</b>
<b>B</b>	<b>Horizontal and Vertical Polarization Power Density Measurements</b>	<b>132</b>
<b>C</b>	<b>Measurement Cable and Antenna Parameters</b>	<b>140</b>
<b>D</b>	<b>Inventory of Loughborough University Machine Workshop</b>	<b>143</b>
<b>E</b>	<b>Power Delay Profiles for Computing Delay Spread</b>	<b>144</b>
<b>F</b>	<b>APDPs Obtained from Virtual Arrays for Fractal Overlay Model</b>	<b>157</b>

# Chapter 1

## Energy Harvesting for Low-power Devices

### 1.1 Internet of Things for Industry

With industrial information communication technologies evolving from the embedded systems to cyber-physical systems (CPS), it is envisaged that CPS will enable the provision of services such as augmented reality, machine-to-machine communications, data analytics and simulation of manufacturing processes [1]. In order to achieve this aim, research and innovation is required in the following categories [2]:

1. Embedded systems focused on electronics, communication technologies and microsystems
2. Virtual/augmented reality, ambient intelligence and high-performance computing
3. Human/machine interaction with language technologies and service robotics

With respect to communication technologies and electronics, twenty-first century industries use wireless sensor nodes (WSN) for condition monitoring. One of the challenges associated with the current deployment is that they are predominantly powered via a battery, which constitute a significant percentage of the volume and weight [3]. In most cases, the batteries adopted in these nodes usually have a limited lifetime in the range of months to a few years, and will eventually require frequent replacement [4]. This



reoccurring maintenance process introduces significant operational cost when there are a large number of sensor nodes on the factory shop floor [5]. As a profitable alternative, energy harvesting techniques can be used to power up sensor nodes or to extend the lifespan of the batteries. The radio communication subsystem in WSN and wireless industrial microsystems determine the battery life, and in order to extend their operational lifetime [6], low power radio communication technologies such as Zigbee [7] and Picoradio [8] can be adopted in the radio front ends of these devices. In order to address the disadvantages associated with battery power for these devices, there are three known techniques that can be adopted [9–11].

1. Improve the energy density of storage systems;
2. Develop schemes for distributing and providing power;
3. Harvest energy from ambient sources.

Ongoing research into energy density improvement can be found in the literature. Some of which include miniaturized fuel cells [10, 11]. The second approach requires power to be transmitted wirelessly. One of the techniques adopted in this domain is powering devices through radio frequency (RF), such as radio frequency identification (RFID) tags. However, careful design is required to ensure interference is kept minimal and exposure limits are not exceeded [9]. Moreover, they only work over a short range. On the other hand, energy harvesting (EH) can provide a means of powering sensor nodes and other low power electronics.

Maintenance of critical assets in manufacturing plants today is typically done via condition monitoring. Industrial monitoring systems such as the NI CompactRIO, depend on a large number of sensor inputs measuring various parameters on the shop floor (for example temperature, vibration, rotation, and resource usage). To operate a highly reliable maintenance network, it is essential that these sensor nodes are self-sustainable during their lifetime. In this introductory chapter, energy harvesting techniques and co-located energy harvesters for WSN are discussed.

## 1.2 Energy Harvesting Techniques

Energy harvesting also known as energy scavenging is converting other forms of energy available within a given environment into electrical energy. The power consumption of sensor nodes is dependent on diverse parameters and features such as the transmitter/receiver radio electronics, wireless channel power loss (free space or multipath fading), data packet size, communication distance, current drawn for data transmission and reception, data rate and duty cycle [12–15]. As a result, there is no specific power consumption value [4]. With respect to commercial off-the-shelf (COTS) sensor nodes (such as Rockwell’s WINS and Medusa II), the power requirement for WSN can vary from 25 mW in a low-end sensor node to 1000 mW in a high-end device [4]. This wide variation can be associated to the sensor node electronics. For example, the power consumption of the microprocessor in the Rockwell’s WINS is 400 mW and 16.5 mW in the Medusa II <sup>1</sup>. Harvesting energy from the environment can be done through the following mainstream forms:

1. Vibration/motion
2. Light (solar)
3. Thermal
4. Radio frequency

Due to the time-varying nature of ambient energy, power management circuits are usually required to maintain continuous operation [10]. Thus, the essential connection blocks in an energy harvesting system will include an energy harvester, storage unit, power management circuitry (with boost converter), ultra-low power (ULP) microcontroller unit (MCU) and a wireless interface. Typically, in an energy harvesting device, the energy storage unit powers the entire system (MCU, sensor, and wireless interface) [17].

---

<sup>1</sup>Adopting the energy consumption model presented in [16], the power consumption of a typical sensor node can be estimated at 250 mW.

### 1.2.1 Ambient Vibration Energy Harvesting

According to [18], “vibration energy harvesting is the process by which otherwise wasted vibration (from a piece of industrial machinery for example) is harvested and converted to useful electrical energy to power miniature devices”. In order for a vibrating source to be suitable for energy harvesting, two important characteristics must be present in the vibrating structure [18]. These are: resonant frequency and vibration level. Provided a resonant or dominant frequency component is present in the frequency analysis of the target mass, a vibration energy harvester (VEH) can be tuned to this frequency to ensure the highest operational efficiency. VEHs are usually modeled as a mass spring damper system. The vibration level can be measured in terms of displacement (m), velocity (m/s) or acceleration ( $\text{m/s}^2$ ). However, acceleration also known as “g” is widely used. There are three widely known methods for harvesting mechanical/human motion. They are: Electromagnetic (inductive), Electrostatic (capacitive), and Piezoelectric [6, 10, 11].

### 1.2.2 Ambient Light Energy Harvesting

Photovoltaic (PV) cells (also known as solar cells) are made of semiconductor materials and are used for transducing sunlight (or artificial light) to useable electrical power. The operating principle of solar cells is based on the *Photoelectric effect*, whereby semiconductor materials release electrons when exposed to photons of light. These loose electrons are then used to generate electric current by attaching conductors to the positive and negative sides of the semiconductor. The amount of harvestable power from a PV cell is dependent on several factors. Some of which include: the location (indoor or outdoor), type of lighting (florescent or incandescent), type of PV cell used, available irradiance, PV cell size, operating temperature and the conversion efficiency. The spectral composition of the light source is a vital criterion in selecting a suitable PV cell, as different light sources have unique spectral components [5]. For example, a DSSC is more suitable for locations with low irradiance and artificial light sources than a thin-film solar cell. The efficiencies of COTS PV cells ranges from 5% to 30% [9]. The harvestable ambient energy data presented in [9] corroborates the intuition that indoor irradiance levels are substantially reduced when compared to outdoor values.

### 1.2.3 Ambient Temperature Energy Harvesting

Temperature difference offers an opportunity for energy harvesting using thermoelectric devices. The operating principle for these devices is the *Seebeck effect* [19]. This occurs when a temperature difference exists between two different conductors in contact. With the introduction of an electrical circuit, a direct current (DC) is produced as a result of the movement of electrons from the hot material to the cold material. The core element in a thermoelectric device is the thermopile, which is an array of thermocouples connected thermally in parallel or electrically in series. This interconnection becomes necessary due to the low voltage range produced by a thermocouple per temperature difference in Kelvin. Additionally, these devices can have a heat-sink or radiator attached to ensure that the heat is dissipated to the environment effectively [9]. Thermoelectric generators (TEG) are generally suitable for environments where high temperature sources exist, for example a hot exhaust pipe [20]. The open circuit voltage generated by a thermoelectric generator is directly proportional to the number of thermocouple pairs, temperature gradient and Seebeck coefficients [9].

### 1.2.4 Ambient Radio frequency Energy Harvesting

Wireless power transfer is essentially in two forms: non-radiative and radiative. In the former, resonant coupling is used to transfer energy between two coils without contact and are known to have a high power conversion efficiency over a very short range [27]. A resonant coupling circuit is shown in Figure 1.1, where a RF source ( $V_1$ ) is connected to a resonant circuit that is made up of  $L_1$  and  $C_2$ . The receiving resonator (represented by  $L_2$  and  $C_1$ ) is then used to power a load  $R_2$ . The losses in the transmitting and receiving coils are represented by  $R_3$  and  $R_1$ . In the latter, a source (intentional or unintentional) sends electromagnetic (EM) waves through space. The waves are then captured by a receiving antenna (located at a distance) and a RF- DC conversion circuit is used to rectify the alternating current (AC) voltage to useable direct current (DC) voltage (see Figure 1.2). The proximity of the source determines if it is regarded as ambient RF energy harvesting or RF wireless power transport. For example, harvesting RF in the far-field of a GSM base station will be classified as RF energy harvesting, while harvest-

ing RF waves in the far-field of a dedicated RF source a few meters away is known as RF energy transport [28]. The input matching circuit in Figure 1.2 is required for maximum power transfer between the antenna and the input impedance of the rectifier circuit (which can be obtained via harmonic balance simulations). Harmonics generated from the non-linear rectifying circuit impair the conversion efficiency. Thus an output matching circuit can be introduced, such that the circuit elements are selected to maximize the rectifying efficiency. The effect on an output matching/filter network was investigated in [21]. The power spectrum results showed that rather than allowing the harmonics generated by the rectifier device to be absorbed by the load, filtering out these harmonics with a low pass filter after the rectifier can increase the RF- DC conversion efficiency.

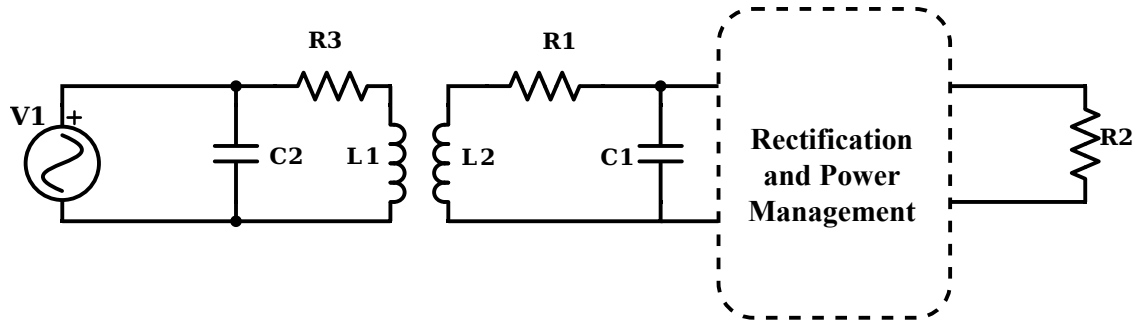


Figure 1.1: Resonant coupling (non-radiative).

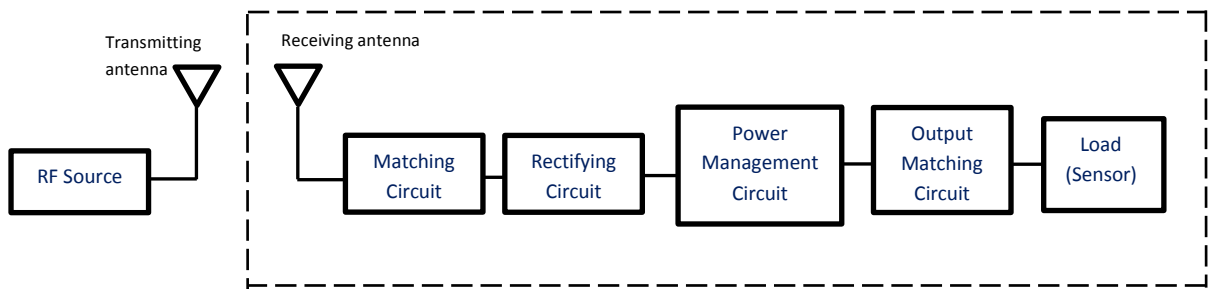


Figure 1.2: Radiative RF power transfer system. The dashed box is widely known as a rectenna.

### 1.3 Co-located Energy Harvesters

Wireless sensors today exist in environments that have multiple ambient energy sources. In such situations, it is possible to increase the amount of power absorbed from the ambient and system reliability by combining multiple ambient energy sources, thus reducing blackout time due to the variations associated with harvestable sources [22, 23]. From the multi-source architecture, AC sources are rectified prior to DC combining. One of the major drawbacks of combining multiple sources is the backward coupling associated with the circuit dynamics. An example is energy being transferred from a vibrating structure to the energy storage system, which in turn impedes the maximum strain obtainable [22]. However, if electrical isolation can be achieved, then these ambient sources (especially vibration) can be tuned individually [22]. There are two connection topologies available in the literature for combining ambient sources: they are parallel topology and series topology [22, 24]. In reality, these systems can operate suboptimally; especially when the individual sources are connected in parallel and are generating different open circuit voltages. Some examples of collocated energy harvesters in the literature include:

1. Wickenheiser et al.: A thermoelectric generator was combined with a piezoelectric vibration energy harvester [22].
2. Carli et al. and Park et al.: A wind energy harvesting system was combined with solar PV cells [23, 25].
3. Schlichting et al.: A solar PV cell was combined with a piezoelectric generator in series and parallel. Also investigated was an array of piezoelectric generators [24].
4. Collado et al.: Solar cells were combined with rectennas for energy harvesting [26].

## 1.4 Research Motivation

To effectively transport radio waves in a factory for the purpose of harvesting, it is essential to understand the behaviour and propagation mechanisms present at the site. This can be done by site-specific measurements or deterministic modelling. The challenge with measurement campaigns is the associated cost and in some cases operation logistics involved in accessing the site. On the other hand, deterministic models require exact floor plans in order to use diffraction theories to evaluate the electric field at interacting surfaces. However, in some cases, floor plans carry sensitive detail that sometime requires a lengthy clearance/security processes. In the literature, very few authors [27] have investigated modelling factory like spaces without exact detail of the inventory. In this project, a purely deterministic technique that models small-scale propagation effects has been investigated and used to determine the suitability of ambient RF energy harvesting in factory environments.

## 1.5 Research Contribution

The novel contribution of this thesis are:

1. Evaluating ambient energy harvesting sources at the Ford Dagenham Engine Plant. The key findings of the measurement campaign were that ambient RF from radio access technologies (RATs) around the site was not sufficient for RF energy harvesting; temperature differences between the machines and room temperature was sufficient for COTS TEGs and indoor lighting could be harvested using COTS PV cells. The outcome of the measurement campaign can be made useful for the plant manager as a feasibility study for energy harvesting at the plant. The measurement data from the three energy domains characterized was published in [28, 29].
2. Measuring delay spread in a factory environment. Using the University machine workshop which has equipment similar to a factory, delay spread measurements were carried out between 2300 - 2500 MHz using a frequency domain measurement system. The results were used to validate the commercial deterministic mod-

elling software used in this thesis.

3. Developing a deterministic model that recreates the time dispersion (delay spread) of multipath rich environments. With the aid of fractal geometry, this thesis has been able to estimate delay spread in factory environments using ray tracing techniques without details of the inventory.
4. Evaluating 2-dimensional spatial interpolation techniques for predicting received power and received power density at unsampled locations in an indoor environment. The RF measurement campaign at the automobile was carried out at five scattered locations, and in order to obtain a broader distribution of RF power density, spatial interpolation methods were used to estimate the power density in form of a 2-dimensional grid. The prediction errors of the interpolation methods used showed that inverse distance weighting (IDW) and kriging were suitable. The results of this study were published in [30]. With the aid of a power density grid, an estimate of the accumulated power over time was calculated for a mobile sensor device travelling predefined paths.

## **1.6 Organisation of this thesis**

Chapter 2 presents a background study of the wireless channel. Based on radio propagation mechanisms, narrowband and wideband characteristics of the wireless channel can be determined for a given location. A detailed overview of how to obtain these channel characteristics is also presented.

Chapter 3 will discuss the results of the measurement campaign carried out at an automobile plant. Using the measurement data, an energy harvesting system engineer can design a suitable harvester that works optimally using the available ambient energy. A survey of measurement techniques and adopted measurement procedures are also discussed.

Chapter 4 presents the results of a measurement campaign carried out at a machine workshop at Loughborough University. The wireless channel measurement data obtained from the workshop was used to validate the commercial ray tracing software. Also



discussed in this chapter is an overview of wideband channel sounding techniques for indoor locations.

Chapter 5 presents details on a novel deterministic approach for modelling wideband characteristics of a factory like wireless channel. In this chapter, fractal geometry is used to mathematically generate metallic inventory for a machine workshop. Using the environment created by the fractal overlaying algorithm, the time dispersion wideband characteristic of the channel was deterministically modelled and compared with the result obtained using the deterministic model of the floor plan and exact inventory at the machine workshop. It also discusses the comparison of the delay spread obtained from the fractal model for line-of-sight (LoS) and non line-of-sight (NLoS) topographies with a widely known wideband statistical model.

Chapter 6 demonstrates how spatial interpolation techniques can be used to predict received power density. In this chapter, three widely known scattered interpolation methods were used and were evaluated using an error measure. Using the deterministic model from Chapter 5 and the sparse measurement locations in Chapter 3, spatial interpolation can then be used to obtain an approximate distribution of the energy profile in a specified location. Chapter 6 also presents a mathematical model for estimating the accumulated energy a radio frequency energy harvesting device is exposed to while travelling a pre-defined path.

Chapter 7 concludes this thesis by highlighting the key findings, the industrial applications and suggestions for future research work.

## **Chapter 2**

# **The Industrial Wireless Channel**

This chapter discusses the theory relating to wireless channel characterization. It also discusses propagation effects encountered in the wireless channel which alter the orientation and characteristics of the EM wave detected at the receiver. In order to design an effective radio communications system for any wireless device or network system, the wireless channel needs to be studied and understood via measurements surveys or channel models. In actuality, the channel state information obtained is usually fed back to the transmitter and/or receiver design so that information is transferred with the least interference, distortion or loss. In Section 2.3, multipath fading is discussed with respect to variations in the wireless channel and the preservation of the spectral characteristics of the signal. Sections 2.4 and 2.5 discuss how narrowband and wideband characteristics of a wireless channel are obtained. In Section 2.6, ray tracing as a deterministic method for obtaining wireless channel characteristics is discussed. By presenting a detailed description of the behaviour of the wireless channel and radio propagation, the complexities associated with RF front end system design can be appreciated.

## 2.1 Introduction

Wireless communications has been described as the fastest growing segment of the telecommunications industry in [31]. This has been corroborated by Cisco's visual networking index (2016), which states that mobile traffic has grown over 18-fold between 2011 and 2016. Moreover, it is anticipated that mobile internet traffic will account for 20% of total IP traffic by 2021 [32]. When an EM wave is transmitted from a transmitter to a receiver, the signal travels through an unguided channel that experiences fluctuations when the transmitter, receiver or objects within the channel move. These fluctuations cause uncertainty in predicting the received signal, which subsequently impairs the ability of the system designer to evaluate parameters such as wireless coverage, bit error rate (BER) and supportable data rates.

In Figure 2.1, the wireless communication channel within an industrial environment is depicted. The figure clearly shows a realistic implementation whereby objects of different material definition and heights are present between and around the transmitter and receiver. These objects (also known as scatterers) present within the wireless channel interact with the EM wave and cause the transmitted EM wave to travel via multiple paths. This "multiple path" scenario causes the signals to arrive at the receiver terminal with different phase, amplitude and time, consequently introducing rapid variations in the amplitude of the received power. This phenomenon is known as *Multipath Propagation* and the individual arriving signals are referred to as multipath components (MPC).

Generally, wireless channel characteristics vary from one site to another. For a specified operating frequency, this characteristic difference can be due to site inventory, building materials, presence and mobility of humans and the building layout. In order to understand the channel behaviour, measurements are usually carried out in either the frequency, time domain or by using spread spectrum techniques. In the time domain, an RF pulse with specified pulse width and repetition period is sent across the channel. Frequency domain techniques employ swept sinusoids with known parameters across the channel bandwidth and spread spectrum techniques cross correlate spread signals.

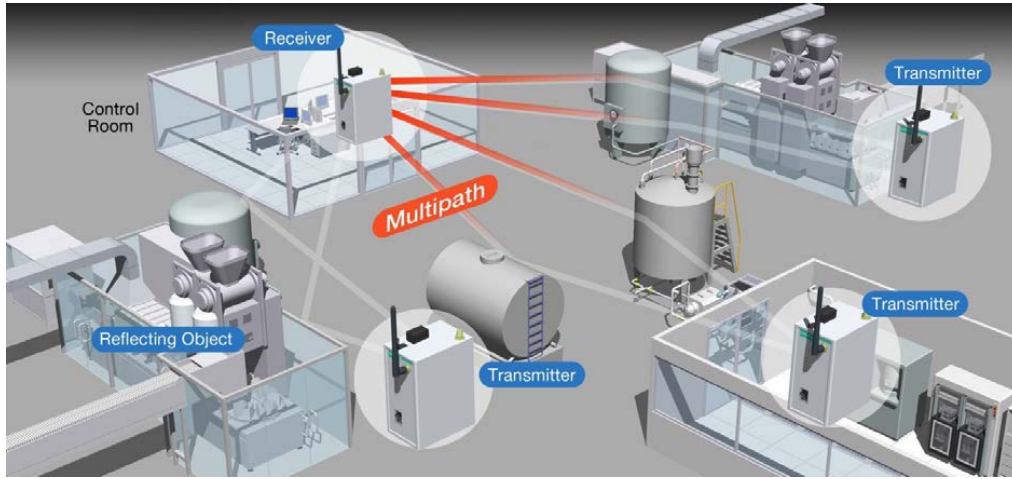


Figure 2.1: Wireless communication channel [33].

Given that the deployment locations differ, wireless channel models presented by standard organisations (such as the IEEE and 3GPP) provide channel characteristics based on the operating frequency (sub 6 GHz or millimetre wave), location (indoor or outdoor) and topography (LoS or NLoS). For example, a pictorial overview of the IEEE 802.15.4a parameterized ultra wideband (UWB) channel model can be viewed in Figure 2.2.

COTS devices based on widely known communication standards (such as IWAN, WiMAX, WirelessHART) can be used to create wireless networks in industrial environments. The radio interfaces of the access points (AP) and client modules used in these scenarios employ techniques such as multiple-input multiple-output (MIMO), orthogonal frequency division multiplexing (OFDM) and mesh networks to maintain reliable communications on the factory shop floor. Nonetheless, while the uptake of wireless/mobile communication is growing, a handful of challenges exist with respect to the wireless channel, spectrum scarcity, mobility management and energy efficiency.

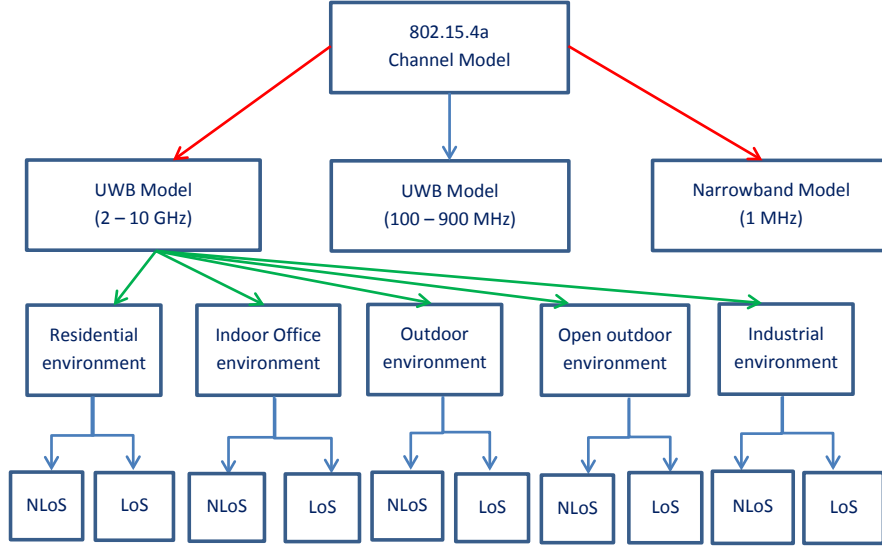


Figure 2.2: Illustration of the 802.15.4a UWB channel model for 2 - 10 GHz.

## 2.2 Characterizing the Wireless Channel

In this thesis, the fading definitions adopted are guided by [31, 34]. According to Rapaport, *fading* is of two types. *Large-scale fading* accounts for the average received signal power and losses caused by EM wave propagation mechanisms for a specified transmitter  $\rightarrow$  receiver ( $T_x \rightarrow R_x$ ) separation distance. On the other hand, *small-scale fading* (which is also known as *fading* [34]) predicts the rapid variation of the received signal power over a few wavelengths. In other words, small-scale fading can be viewed as the destructive or constructive effect of MPCs arriving at a simple receiver. A simple receiver refers to one without equalization. The MPCs arriving at the receiver will have different phases and time delay due to the  $T_x \rightarrow R_x$  separation distance, path travelled, location and orientation of the scatterers and the position of the receiver. At a simple receiver, these components are vectorially combined, which leads to the following [34]:

1. Changes in the amplitude of the received signal. This amplitude variation has been observed to follow a *Rayleigh distribution* when a LoS is absent and a *Rician distribution* when the LoS path is present.
2. Random frequency modulations due to changing Doppler shifts on multipath signals (Doppler spread).

### 3. Time dispersion caused by multipath propagation delay

In Figure 2.3, the effect of the summing in-phase and out-of-phase MPCs is illustrated. In general, as the separation distance between a transmitter and a receiver increases, the receiver experiences both large-scale and small-scale fading as depicted in Figure 2.4, where  $P_r$  is the received power (dBm),  $P_t$  is the transmit power (dBm) and  $d$  is the  $T_x \rightarrow R_x$  separation distance (m).

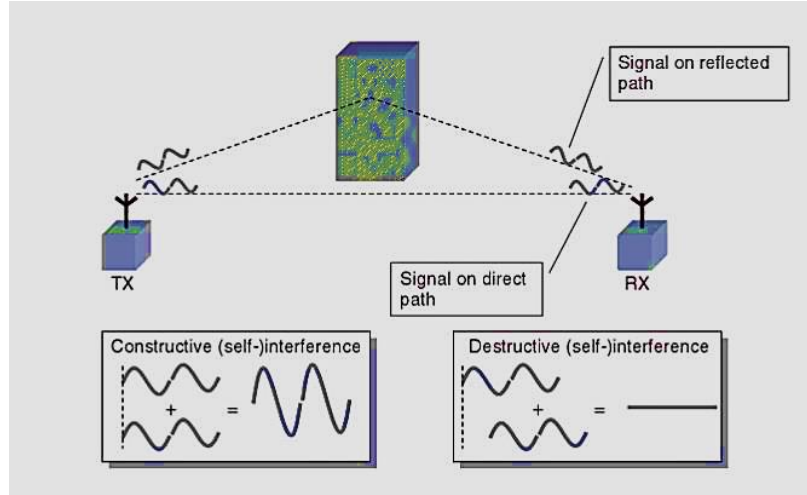


Figure 2.3: Illustration of constructive and destructive interference [35].

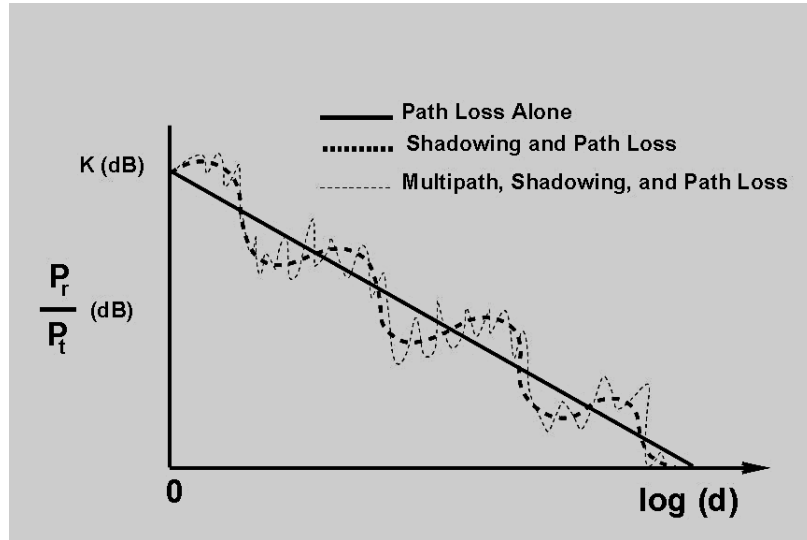


Figure 2.4: Illustration of large-scale and small-scale fading effects versus distance. Path loss and shadowing account for large-scale effects, while multipath accounts for small-scale effects [31].

The physical (PHY) and media access control (MAC) layers of a wireless communication system are essential in determining performance metrics such as data rate, throughput. As a result, a critical understanding of the effects of the wireless channel and radio front ends on the transmitted signal is essential to the overall system design. The propagation properties of the wireless channel can be grouped into two categories [36]:

1. Narrowband signal characteristics
2. Wideband signal characteristics

The narrowband features provide an overview of the signal strength at the receiver, which is usually a vectorial combination of the complex amplitudes of the paths detected. This feature can be associated to *large-scale fading*. On the other hand, wideband characteristics provide details regarding multipath propagation in the channel (*small-scale fading*) as well as the channel frequency selectivity [36]. As a result, both wideband and narrowband features are required to obtain a complete description of the channel. Assuming the wireless channel is time invariant, the narrowband features presents the channel behaviour (impulse response) at a spot frequency, and the wideband features represent the overall impulse response [36].

## 2.3 Multipath Fading in Wireless Communication

Small-scale fading can result into time dispersion (delay spread) or frequency dispersion (Doppler spread). With respect to the time dispersion, the wireless channel can either be described as flat fading or frequency-selective fading. On the other hand, depending on how rapidly the transmitted signal changes with respect to the rate of change in the channel, frequency dispersions can either create a slow or fast fading wireless channel. The coherent bandwidth ( $B_c$ ) of a wireless channel is the range of frequencies over which two frequency components have a strong potential for amplitude correlation. Doppler spread is a measure of the spectral broadening caused by the velocity changes in the wireless channel, transmitter or receiver while delay spread gives a measure of the frequency selectivity or the time dispersion in the wireless channel.

### **2.3.1 Flat Fading**

If a mobile radio channel possesses a constant gain and linear phase response over a specified bandwidth that is greater than the signal bandwidth, then the transmitted signal will undergo “flat fading”. In a flat fading channel, the spectral characteristics of the transmitted signal are preserved at the receiver. However, amplitude fluctuations may occur. In other words, in a flat fading channel, the signal bandwidth is much smaller than the channel coherent bandwidth. In the time domain, the symbol period is much greater than the delay spread. A classical example is the Rayleigh flat fading channel, which assumes that the channel induces a time varying amplitude according to the Rayleigh distribution

### **2.3.2 Frequency Selective Fading**

If the wireless channel possess a constant gain and linear phase over a bandwidth that is smaller than the bandwidth of the transmitted signal, then the wireless channel is described as “frequency selective”. In this scenario, which is realistic; multiple copies of the transmitted waveform arrives at the receiver. These multiple copies are usually attenuated by different amounts and overlap in time at the receiver.

### **2.3.3 Fast Fading**

In a fast fading channel, the channel impulse response (CIR) changes rapidly within the transmitted signal’s symbol duration. This means that the coherence time of the channel is smaller than the symbol period or the signal bandwidth is smaller than the Doppler spread.

### **2.3.4 Slow Fading**

In a slow fading channel, the CIR changes at a much slower rate than then transmitted signal. In this case, the wireless channel can be assumed to be static over the specified bandwidth. For a slow fading channel, the symbol period is less than the coherence time or the signal bandwidth is greater than the Doppler spread.



## 2.4 Narrowband Channel Characteristics

### 2.4.1 Theoretical Methods (Narrowband)

Narrowband channel features can be obtained via simple theoretical means such as the free space path loss (log-distance) model and the two-way ground model.

#### Free space model (Log-distance)

This model assumes a clear LoS between the transmitter and the receiver and it is given by the *Friis transmission equation* in eqn. (2.1). It is used to determine the signal strength for a given  $T_x \rightarrow R_x$  separation distance  $d$ , where  $P_t$  is the transmitted power,  $P_r(d)$  is the received power at  $(d)$ ,  $G_t$  is the transmit antenna gain,  $G_r$  is the receive antenna gain,  $\lambda$  is the transmitting wavelength,  $n$  is the path loss exponent which is equal to 2 and  $L$  is cable loss. In real life scenarios, a reference distance  $d_o$  with known received power or path loss is used. The received power  $P_r(d_o)$  or path loss  $PL_{d_o}$  at  $d_o$  can be derived from an average spot measurements with radius  $d_o$ . The free space path loss (dB) can then be derived from Friis equation, and is presented in eqn. (2.2). This is also referred to as the *log-distance path loss model*, as received signal power decreases logarithmically with increasing distance.

$$P_r(d) = \frac{P_t G_t G_r}{L} \left( \frac{\lambda}{4\pi d} \right)^n \quad (2.1)$$

$$PL_d = PL_{d_o} + 10n \log(d/d_o) \quad (2.2)$$

#### Log normal shadowing

This model accounts for signal attenuation caused by clutter in the channel. For a specified  $T_x \rightarrow R_x$  separation distance, the *free space propagation model* gives the same result, even when the receiver is shadowed by an object. However, in reality, the average received signal predicted by eqn. (2.2) will vary due to shadowing. This model adds a zero-mean Gaussian distributed random variable  $X_\theta$  to the path loss model in eqn. (2.2) [34]. The path loss using this model can be computed using eqn. (2.3) and the values of the random variable can be derived either from measurements and statistical

techniques such as linear regression.

$$PL_d = PL_{d_o} + 10n \log(d/d_o) + X_\theta \quad (2.3)$$

### Two-ray ground reflection

In typical wireless communication channels, the transmit signal seldom uses the LoS path. The two-ray model adds a ground reflection to the LoS path adopted in the *free space propagation model*. However, this model gives unstable results for short range distances. Therefore a cross-over distance  $d_c$  is defined (as shown in eqn (2.4)) to determine when to adopt the model. For a given  $T_x \rightarrow R_x$  separation distance  $d < d_c$ , the *free space propagation model* is used. The received power using this model can be computed using eqn. (2.5), where  $h_t$  is the transmitter height and  $h_r$  is the receiver height.

$$d_c = 4\pi h_t h_r / \lambda \quad (2.4)$$

$$P_r(d) = \frac{P_t G_t G_r h_t^2 h_r^2}{d^4 L} \quad (2.5)$$

### 2.4.2 Measurement-based Stochastic Models (Narrowband)

Radio propagation measurements have been carried out in indoor locations (such as offices and factories) as well as outdoor scenes [37–50]. While both scenes require the same measurement instruments, they present different propagation topographies with respect to scatterers, material composition of the environment and mobility. In this subsection, widely known measurement-based stochastic models for outdoor and indoor locations are discussed. It should be noted that the measurement data presented in this subsection are generalizations from the respective measurement campaigns. It is expected that site-specific details would vary for each location.

## A. Outdoor Models

Evaluating radio coverage outdoors requires estimating the effects of the terrain and scatterers such as building rooftops, trees, and other physical structures larger than the signal wavelength. These scatterers introduce attenuation of the radio signal through the EM propagation mechanisms.

### Okumura-Hata

The Okumura-Hata model [51] is based on measurement data gathered by Okumura in Tokyo, Japan and has been widely adopted in predicting outdoor wireless coverage. The path loss (between 150 MHz and 1500 MHz) using this model can be computed using eqn. (2.6), where  $A$ ,  $B$  and  $C$  are dependent on the operating frequency and transmitter/receiver heights. The correction factors  $A$ ,  $B$ ,  $C$  depend on the environment, while  $h_b$ ,  $h_m$ ,  $f_c$ ,  $a(h_m)$  represent the transmitter and receiver antenna heights, operating frequency and mobile antenna correction factor.

$$PL = A + B \log(d) + C \quad (2.6)$$

$$A = 69.55 + 26.16 \log(f_c) - 13.82 \log(h_b) - a(h_m) \quad (2.7)$$

$$B = 44.9 - 6.55 \log(h_b) \quad (2.8)$$

For a medium sized city,  $a(h_m)$  is given by eqn (2.9) and for a large city, it is computed using eqn. (2.10) and eqn. (2.11)

$$a(h_m) = (1.1 \log(f_c) - 0.7)h_m - (1.56 \log(f_c - 0.8)) \quad (2.9)$$

$$a(h_m) = 8.29(\log(1.54h_m)^2 - 1.1) \quad \text{for } f_c \leq 300\text{MHz} \quad (2.10)$$

$$a(h_m) = 3.2(\log(11.75h_m)^2 - 4.97) \quad \text{for } f_c \geq 300\text{MHz} \quad (2.11)$$

### COST-231

The European Co-operative for Scientific and Technical Research (COST) extended *Okumura-Hata* model to compute path loss and coverage at frequencies going up to 2 GHz. This was required in order to estimate large-scale radio propagation effects for global system for mobile (GSM) communications in Europe [52]. The modified equations are given in eqn. (2.12), where  $C$  is 0 dB for medium sized and suburban areas and 3 dB for metropolitan centres. In order to obtain reliable results, the model requires that

the transmitter and receiver heights should be between 30 m to 200 m and 1 m to 10 m, and the  $T_x \rightarrow R_x$  separating distance be between 1 km and 20 km.

$$PL = 46.3 + 33.9 \log(f_c) - 13.82 \log(h_b) - a(h_m) + (44.9 - 6.55 \log h_b) \log(d) + C \quad (2.12)$$

## B. Indoor Models

Radio propagation indoors experiences the same EM mechanisms as outdoor propagation. In closed spaces such as office buildings, EM waves have to travel through walls and across floors.

### Wall-partitioned path loss models (same floor)

Generally, indoor partitions could be *hard* or *soft* [34]. Hard partitions are created with the building structure and soft partitions are moveable. An example of a soft partition is plasterboard used in office partitioning. In order to obtain the loss introduced by these partitions on the same floor, signal power measurements are required. In [34], a summary table of signal loss measurements is presented for various material types. On the same floor, the site-specific path loss can be computed using eqn. (2.13), where  $L_w$  is the measured signal loss associated with the obstruction for a LoS path.

$$PL_d = PL_{d_o} + 10n \log(d/d_o) + \sum_{i=0} L_w + X_\vartheta \quad (2.13)$$

### Wall-partitioned path loss models (between floors)

Obtaining the loss across floors introduces another term to eqn. (2.13). The signal attenuation across floors can be obtained via measurement as shown in [53]. The predicted path loss using this model can then be calculated using eqn. (2.14), where  $FAF$  is the floor attenuation factor in dB.

$$PL_d = PL_{d_o} + 10n \log(d/d_o) + \sum_{i=0} L_w + X_\vartheta + FAF \quad (2.14)$$

## 2.5 Wideband Channel Characteristics

Wideband propagation models provide a means of evaluating how other RF front end features (such as modulation techniques and equalization) perform with respect to a

specified multipath channel. In this section, widely known wideband stochastic and measurement based statistical models for outdoor and indoor locations will be presented. In order to obtain tractable solutions for modelling the wireless channel, it is assumed that the channel is slowly time-varying or quasi static. However, in a scenario where interacting objects, transmitter and receiver are fixed, a linear time-invariant system can be assumed. In a slowly time-varying wireless channel, the scattering function of the channel can be split into two functions: the delay spectrum and the Doppler spectrum as shown in eqn. (2.15) [36].

$$S(\tau, \lambda) = Q(\tau)D(\lambda). \quad (2.15)$$

$$Q(\tau) = |\overline{h(\tau)}|^2 = \sum_{i=0}^N \overline{|\beta_i^2|} \delta(\tau - \tau_i) \quad (2.16)$$

The power delay spectrum (which is also known as the delay profile) is the average of the channel impulse response as shown in eqn. (2.16), while the Doppler spectrum ( $D(\lambda)$ ) refers to the broadening of the frequency detected at the receiver due to the Doppler shift of the respective MPCs.

## 2.5.1 Stochastic Wideband Models

### N-tap Rayleigh & Rician-fading Models

In both models, the following are assumed:

1. The radio channel is *slowly time-varying*
2. The amplitude of the MPCs varies according to the *Rayleigh distribution* for a NLoS topographies and a *Rician* distribution when a LoS is present.
3. The phase of the MPCs is uniformly distributed over  $[0, 2\pi]$

In Figure 2.5, the Rayleigh fading behaviour is illustrated by simulation at 900 MHz for a mobile device travelling at 120 km/hr [34]<sup>1</sup>. From Figure 2.5, it can be seen that deep fades occur when the signal drops below a threshold (that specifies receiver sensitivity). The statistics of the level-crossing rate (LCR) and fade duration dictate the performance of the receiver RF front end.

---

<sup>1</sup>This speed corresponds to a maximum Doppler shift of 100 Hz.

## 2.5.2 Measurement-based Stochastic Models (Wideband)

### A. Outdoor Wideband

**COST 207 Model.** This model is based on measurements using the GSM channel bandwidth (200 kHz) for rural, urban, bad urban and hilly areas [54]. The model provides scattering function parameters for the areas characterized by using four Doppler spectrum realizations and four power delay profiles (one for each of the locations surveyed). The Doppler spectrum available in the COST 207 model for the tapped-delay line are Rayleigh, Rician and Gaussian. From the measurement results provided, the power delay spectrum could be estimated using one-sided single exponential functions.

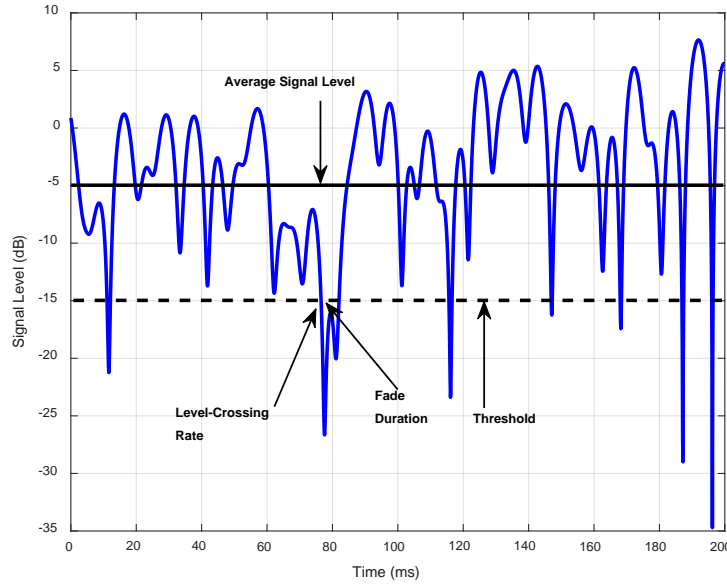


Figure 2.5: A Rayleigh signal envelope at 900 MHz.

### B. Indoor Wideband

#### Saleh-Valenzuela Model.

The Saleh-Valenzuela (S-V) model is based on the clustering of MPCs and the exponential decay the MPCs experience as they arrive at the receiver. Using the S-V model, the channel impulse response can be mathematically expressed as  $h(\tau)$  (shown in equation (2.17)) and illustrated in Figure 2.6, where  $L$  is the number of clusters,  $K$  is the number of MPCs in a cluster  $L$ ,  $\beta_{kl}$  and  $\theta_{kl}$  are the amplitude and phase of the  $k$ th MPC in the  $l$ th cluster,  $\tau_{kl}$  is the arrival time delay of the  $k$ th ray/MPC in the  $l$ th cluster and  $T_l$  is the

cluster arrival time. The ray amplitude  $\beta_{kl}$  is calculated by eqn. (2.18), where  $\Gamma$  and  $\gamma$  are the exponential decay constants for the clusters and rays within a cluster. The average power of the first component in the first cluster is  $\overline{\beta^2(0,0)}$ .

$$h(\tau) = \sum_{l=0}^{L-1} \sum_{k=0}^{K-1} \beta_{kl} e^{j\theta_{kl}} \delta(\tau - T_l - \tau_{kl}) \quad (2.17)$$

$$\overline{\beta_{kl}^2} = \overline{\beta^2(0,0)} e^{-T_l/\Gamma} e^{-\tau_{kl}/\gamma} \quad (2.18)$$

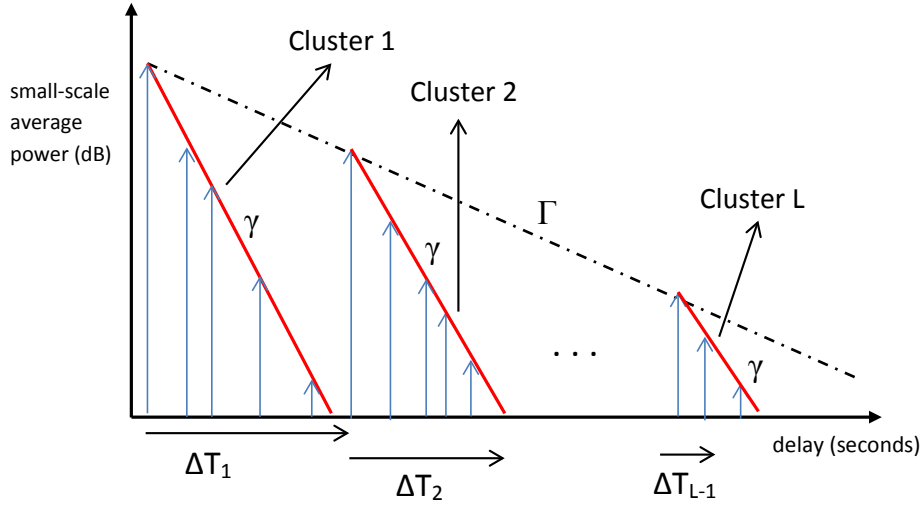


Figure 2.6: Saleh-Valenzuela channel impulse response model. The visually identified clusters are represented with red solid lines with corresponding decay rate ( $\gamma$ ), and the envelope decay constant ( $\Gamma$ ) is represented by the dashed solid line.

## 2.6 Ray Tracing for Wireless Channel Characteristics

Accurate large and small-scale effects for a given location can be obtained via deterministic methods. Deterministic models require a detailed 3-D computer-aided design (CAD) model of the physical location with respect to objects between and around the transmitter/receiver. The operating principle of deterministic models is to solve Maxwell's equations by either using ray optics or finite-difference equations [36]. In ray tracing, this involves two tasks: tracing propagation paths from the transmitter to the receiver and computing the associated electric field. With respect to radio propagation, a “ray” can be visualized as: an EM wave that travels in a straight line in a homogeneous medium, obeys the laws of reflection, refraction and diffraction.

## 2.6.1 Basic Ray Tracing Algorithms

### Shooting and Bouncing Ray (SBR)

The SBR technique introduced by [55] is widely adopted in commercial ray tracing softwares. This process starts by launching rays from a transmitter (known as a source point) to a receiver (known as a field point). An illustration of the SBR algorithm is presented in Figure 2.7. In order to trace rays using this technique, these three steps are required: ray launching, ray tracing and ray reception [56].

Ray launching requires that the rays from a source are uniformly distributed and are launched at discrete angles. This requirement ensures that the rays carry equal power as an isotropic source. After the rays are launched, they can be traced to the field point directly (LoS) or traced from diffracting and reflecting edges or surfaces. In scenarios where the rays hit the floor of a building or ground in urban spaces, the method of image technique is used to determine ground reflection points.

In Wireless Insite<sup>®</sup>, diffracting edges are identified when adjacent rays from a transmitter travel via different paths in the geometry. After the rays have been launched and traced, the specific geometrical paths are constructed. Ray reception is carried out such that a collection sphere is created around a field point, and EM rays passing through that sphere are used in the EM field computation.

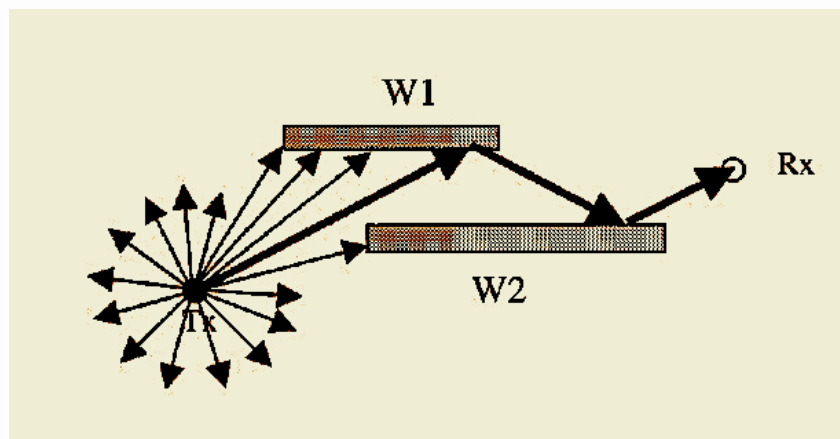


Figure 2.7: The shooting and bouncing ray (SBR) launching schematic. W1 and W2 are arbitrary reflecting surfaces. [57].



### Image Method

This technique is illustrated in Figure 2.8 and it is used to determine the path of a reflected ray. Using Figure 2.8, the path tracing can be explained as follows:

1. Locate the image of  $R_x$  ( $R_i$ ) with respect to the planar reflection surface AB.
2. Connect the image  $R_i$  to  $T_x$  in order to obtain a line segment that intersects the surface at reflection point  $Q$ .
3. Create reflected path using points  $T_x$ ,  $Q$  and  $R_x$

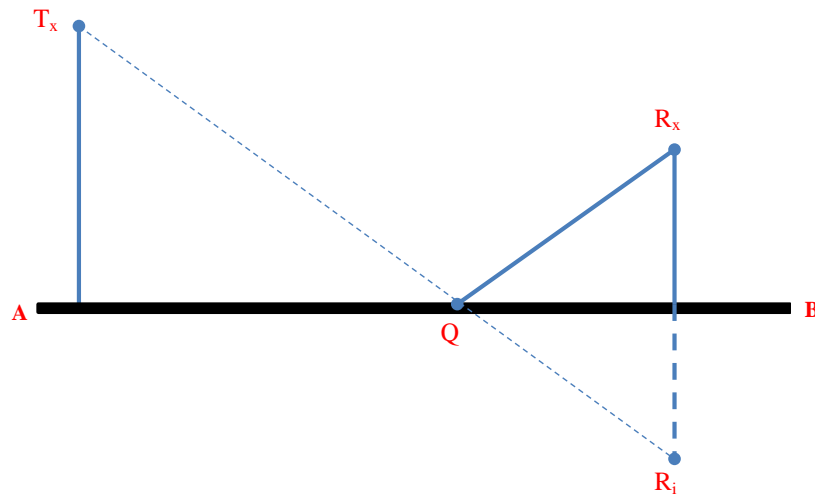


Figure 2.8: Image ray tracing method.

### Hybrid Method

A hybrid algorithm that combines SBR and image method was initially proposed by Tan et. al. in [58]. This method uses SBR to determine the geometric paths, thereafter the Image method is used to adjust the trajectory with respect to the reflection points. The hybrid method possesses added advantages in form of the computational efficiency from the SBR technique and the reflection point accuracy from the image method [57].

## 2.6.2 Evaluating Wireless Channel Characteristics

In the commercial ray tracing suite (Wireless Insite<sup>®</sup>) used in this thesis, the hybrid method is adopted in obtaining geometric paths and the electric field is computed in accordance with the *Uniform Theory of Diffraction* (UTD). At the specified field points, the

rays passing through the collection sphere are combined to determine small and large-scale fading effects such as path loss, delay spread or channel impulse response. Wireless Insite is able to compute large scale power distance relationships by implementing the Hata model, COST 231 model or the free space model. In the literature, ray tracing techniques have been used to effectively estimate wireless channel characteristics such as path loss, delay spread and Rician K-factor [59–64]. With respect to ray tracing, the delay spread of a ray tracing wireless channel ( $\tau_{rms}$ ) can be calculated using eqns. (2.19) to (2.23), where  $\eta_o$  is the free space impedance ( $377 \Omega$ ),  $\lambda$  is the wavelength,  $E_{\theta,i}$  and  $E_{\phi,i}$  are the theta and phi components of the electric field of the  $i^{th}$  path at the receiver,  $\theta_i$  and  $\phi_i$  are the directions of arrival,  $\beta$  defines the overlap of the transmitted and received waveform in the frequency domain,  $L_i$  is the geometric path length,  $c$  is the speed of light. In a measurement regime,  $\tau_{rms-RT}$  becomes  $\tau_{rms}$ ,  $P_i$  becomes the channel power as a function of excess delay  $P(\tau)$ , which is obtained from the complex channel impulse response and  $\bar{t}$  becomes the mean excess delay( $\tau$ ).

$$P_i = \frac{\lambda^2 \beta}{8\pi \eta_o} |E_{\theta,i} g_{\theta}(\theta_i, \phi_i) + E_{\phi,i} g_{\phi}(\theta_i, \phi_i)|^2 \quad (2.19)$$

$$P_R = \sum_{i=0}^{N_p} P_i \quad (2.20)$$

$$t_i = \frac{L_i}{c} \quad (2.21)$$

$$\bar{t} = \frac{1}{P_R} \sum_{i=0}^{N_p} P_i t_i \quad (2.22)$$

$$\tau_{rms-RT} = \sqrt{\frac{1}{P_R} \sum_{i=0}^{N_p} P_i t_i^2 - \bar{t}^2} \quad (2.23)$$

## 2.7 Summary

This chapter has discussed the wireless channel and how it can be characterised. For a quasi-static wireless channel, the Doppler spread, delay spread and the power distance relationship can be used to obtain wideband and narrowband features of a channel. An understanding of radio propagation is required in modelling indoor locations, especially when details of the inventory are unknown. Assuming a quasi-static or slowly time

varying channel, a multipath rich environment like a factory or machine workshop will cause time dispersion arising from multiple reflecting conducting surfaces. The measure of the time dispersion (delay spread) will be used in Chapters 4 and 5 for comparing the wideband characteristic of a site specific floor plan. In the next chapter, ambient energy measurement results from a feasibility study at an engine plant is presented.

## Chapter 3

# Ambient Energy Characterisation

In this chapter, the results of a measurement campaign carried out at Ford Dagenham engine Plant (DEP) is presented and discussed. Irradiance measurement data is presented in Section 3.2, followed by ambient temperature differences and input RF power density in Section 3.4. Input RF power density across the plant varied between  $-127 \text{ dBm/cm}^2$  to  $-113 \text{ dBm/cm}^2$ . The maximum temperature difference measured within 30 cm away from machine parts on the production lines surveyed was  $10 \text{ }^\circ\text{C}$ . Indoor lighting was dominant at the plant via fluorescent tubes, with average irradiance of  $1 \text{ W/m}^2$  ( $-10 \text{ dBm/cm}^2$ ). The results obtained from this measurement campaign showed that indoor lighting and temperature difference were suitable ambient sources for energy harvesting at the DEP.

### 3.1 Introduction

Prior to deploying an energy harvester in any given location, it is essential to evaluate its suitability. Consequently, measurements were taken at the DEP in order to obtain a distribution and availability of ambient energy at the plant. For each of the three domains investigated, different parameters were measured: input RF power density ( $\text{dBm}/\text{cm}^2$ ) for characterizing ambient RF energy; temperature measurements ( $^{\circ}\text{C}$ ) for thermal energy; and irradiance ( $\text{W}/\text{m}^2$ ) for ambient light energy. While ambient light, temperature and RF have been characterised for indoor and outdoor locations in the literature, most of indoor studies investigated office locations. Factory environments are often classified as indoor environments, however they differ in inventory, size, building height and building materials when compared with office or home locations.

In the literature, ambient light has been characterised using radiometric and photometric measurement techniques [5, 65–68]. Radiometric characterisation of light gives an insight into the amount of energy contained in light photons, rather than a perception of how much light is perceivable (as in photometric characterisation) [65]. However, in order to accurately characterise ambient light energy for energy harvesting, it is essential that a radiometric measurement approach is adopted. In the literature, light energy is measured as the radiant flux energy per unit area (also known as irradiance). The long term stationary data presented in [65, 69] was gathered over sixteen months in office buildings in New York, USA using a light-to-frequency converter and a LabJack data acquisition device (DAQ). These results were used to predict energy profiles and develop energy harvesting aware algorithms. At Location A (a students' office on the 6th floor in [65]), the irradiance data was down sampled to 7 hours (9 am - 4 pm) for the first day of the month and averaged over a year. With the measurement setup placed on a windowsill and window shading in place, the average indoor irradiance was computed as  $0.3788 \text{ W}/\text{m}^2$ . In [5], illuminance (*lux*) was measured at residential apartments in Southampton, UK, San Sebastian, Spain and Warsaw, Poland using light meters (ISO-TECH 1337 and DT-8809A). The light levels measured varied from 100 lx ( $0.027 \text{ W}/\text{m}^2$ ) to 3700 lx ( $1.27 \text{ W}/\text{m}^2$ ) over a 24 hour time scale. This was due to the variation in building types and use, weather, time of the day, type of artificial light used, influence of

sunlight as well as the government lighting regulations at the measurement sites. The *lux* results were converted to irradiance by using a linear fit to the illumination levels vs power density for a COTS amorphous-Silicon (a-Si) PV cell. A photodiode sensor on the TelosB mote in [66] was used to gather indoor and outdoor illuminance (*lux*). These traces were used for determining how PV cells could be used for powering and extending communication range in emerging computational RFIDs. Two office locations as well as indoor residential buildings were characterized and the average illuminance for 2.5 hours varied from 49 lx to 241 lx. These photometric results can be converted to radiometric using the linear fit in [5]. For a 9 cm<sup>2</sup> a-Si PV cell, the corresponding irradiance varied from 0.0135 W/m<sup>2</sup> to 0.07 W/m<sup>2</sup>. However peaks of 700 lx (0.22 W/m<sup>2</sup>) and 1091 lx (0.35 W/m<sup>2</sup>) were recorded, which are less than those presented in [5].

In [70], an irradiance characterisation device was conceptualized. The prototype presented was capable of measuring irradiance as well as computing the anticipated DC power output for a-Si and crystalline silicon cells. The setup adopted used two sensors (ADJD-S371 red, green, blue (RGB) digital colour sensor, a light-to-digital converter) and a microSD card for data logging. Indoor irradiance varied from 0.23 W/m<sup>2</sup> (over a two hours period) to 0.17 W/m<sup>2</sup> (over 4091 seconds). Outdoor irradiance values measured were two orders of magnitude greater than indoor traces. A dye sensitized solar cell (DSSC), resistor and a sensor node were used in [68] to obtain irradiance values over 10 days. Indoor irradiance varied from 0.2 W/m<sup>2</sup> to 0.5 W/m<sup>2</sup>, while outdoor irradiance was an order of magnitude greater.

Thermal energy characterization was carried out by attaching a commercially available thermoelectric module to a Dell Alienware laptop personal computer (PC) in [71]. Using a thermal camera, heat dissipation paths for the PC electronics were identified. From the results presented, the maximum temperature difference recorded (8.6 °C), produced 119  $\mu$ W of harvestable power, with corresponding power density of 1.25 mW/cm<sup>3</sup>. Less power was recorded in [72], where a commercial TEG was attached to a human wrist. The harvestable power reported was 20  $\mu$ W at 22 °C room temperature. The authors also highlighted that human motion and wind could alter the temperature difference recorded [72]. A contactless infrared thermometer (Calex PYROPEN-E) and digital thermometers (TENMA 72-2065A, TME KS01-3 surface probe) were used for temper-

ature measurements in [5]. At the measurement sites, the temperature difference for the equipment characterised (radiators, cooker, boiler and water pipes) varied between 11 °C to 59.5 °C. This corresponds to 1 mW to 9 mW when a commercial TEG datasheet was used to estimate harvestable power [73].

Input RF power density levels (indoors and outdoors) has been quantified in the literature by using two measurement setups. The former consists of a spectrum analyser, antenna and a PC for post processing. It is usually used to obtain details of the spectrum of interest [5, 15, 74–79]. The latter consists of a probe as a sensor and a display meter for visualisation [80–83]. In most cases, this setup is used to obtain an overview of the frequency spectrum surveyed.

Narrowband or frequency selective measurements in [15] characterized ambient Wi-Fi signals in an office location, where the received power on the measuring device peaked at -23 dBm<sup>1</sup>. The rectenna designed using the measurement results was able to harvest ambient Wi-Fi and could operate at incident RF power as low as -40 dBm. This was possible because the RF power incident on the antenna array was high enough to turn on the rectifying diodes. In [77], Wi-Fi power density was measured at distances between 7.05 m and 12.30 m away from a wireless access point. The floor on which the measurements were taken had electrical laboratories, classrooms and offices. The recorded RF power density were in the range of -50 dBm/cm<sup>2</sup> to -30 dBm/cm<sup>2</sup>. While it was concluded that the power densities were too low for energy harvesting, the rectenna designed in [15] could be adopted. The European EM field exposure report in [79] for 2G base station (GSM 900 and GSM 1800) showed that the RF power density varied widely from participating countries due to different regulations. Most of the measurement data was carried out in Austria, where the average indoor RF power density near the window and further away was -47.17 dBm/cm<sup>2</sup> and -44.56 dBm/cm<sup>2</sup>. For outdoor locations (which include ground, terrace, balcony and roof top measurement), the average outdoor values were of the same order as the recorded values indoors. However, the maximum power density (-28.73 dBm/cm<sup>2</sup>) recorded during the entire measurement was obtained outdoors.

Wideband measurements carried out by [74] in densely populated areas in London showed

---

<sup>1</sup>The received power on the spectrum analyser can be converted to power density, however the antenna gain of the monopole used was not discussed

that ambient RF can be harvested when there is sufficient incident RF power. The highest incident RF measured for 2G was  $-25 \text{ dBm/cm}^2$  at Hampstead station and  $-36 \text{ dBm/cm}^2$  for 3G at St James Park. These power densities were obtainable due to the fact that the measurements were taken outdoors in areas with very good wireless network coverage from UK mobile network operators. A similar measurement campaign was also carried out by [75] for the purpose of assessing public exposure to macro cells (base stations). Within a separation distance of 0 - 150 m from the 2G base stations characterised, the outdoor RF power density measured was between  $-60 \text{ dBm/cm}^2$  and  $-40 \text{ dBm/cm}^2$ , with indoor values spread over a wider range of  $-80 \text{ dBm/cm}^2$  to  $-40 \text{ dBm/cm}^2$ .

The measurement campaign started off by [75] was extended to microcells and picocells using a similar measurement setup in [78]. Using microcell specifications based on the antenna height and the total radiated power, the measurements were taken 1 - 100 m away from 20 microcell base stations. The total outdoor RF power density of ambient EM waves within the wideband measurement bandwidth (80 -2500 MHz) was in the range of  $-70 \text{ dBm/cm}^2$  and  $-20 \text{ dBm/cm}^2$ , which was largely influenced by 2G base station downlinks. In addition, narrowband measurements were also carried out for 2G micro cell base station downlinks by time averaging the broadcast control channel (BCCH) of the respective microcell base stations. Analysing the power density results from [75] and [78] showed that the power density measured near microcells were generally higher than those measured near macrocell base stations. Apolinio et al. in [76] also characterised RF power density across a wide bandwidth for the purpose of human exposure evaluation by subdividing the spectrum into contiguous bands. The authors integrated the electric field over the measurement bandwidth, consequently making it impossible to estimate power density for RATs present within the measurement bandwidth.

In general, it can be inferred from the literature presented that the RF power density indoors is usually lower when compared to outdoor measurements. This is due to additional propagations effects the EM wave experiences. Some of these effects include building penetration loss, in building reflections or attenuation caused by humans. While it is impossible to make a fair comparison, due to the different propagation environments in the works cited, the results affirm the intuition that the received power (density) of a base station channel is usually higher when measured outdoors than indoors.



## 3.2 Ambient Light Measurements

### 3.2.1 Methodology and Instrumentation (Ambient Light)

Radiometric characterisation of indoor lighting was adopted in the measurement campaign carried out at the DEP. Irradiance was measured using a Kipp & Zonen SP Lite pyranometer [84] (see Figure 3.1) connected via a cable to a data logger (Squirrel SQ2020-2F16) [85] and placed in a fibreglass case. The data logger (shown in Figure 3.2 ), read voltage at a sample interval of 1 minute (in  $\mu\text{V}$ ) from the pyranometer. The measured voltage input was converted to irradiance ( $\text{W}/\text{m}^2$ ) using the sensitivity of the pyranometer in ( $\mu\text{V}/\text{W}/\text{m}^2$ ) and its spectral range ( $\text{W}/\text{m}^2$ ). Due to health and safety requirements, measurements were taken between 10:30 am and 15:30 pm at the DEP. In addition, irradiance measurements were taken at the 5GRC and HSSMI office in London. At the DEP, the pyranometer was placed on a raised flat surface approximately 1.5 m high<sup>2</sup> and desk level at other office locations.

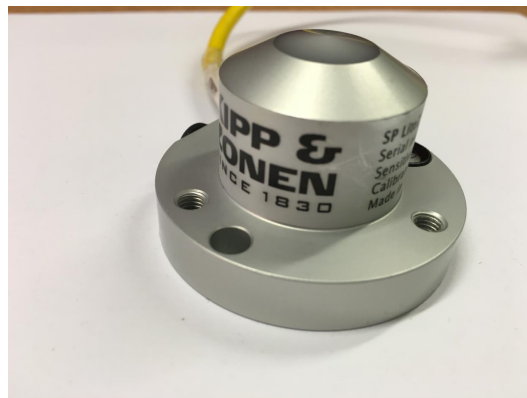


Figure 3.1: SP Lite pyranometer [84]. This device was used to obtain irradiance values at the DEP.

---

<sup>2</sup>As an additional safety requirement, the device was placed on a platform that can be visible to anyone on the factory floor



Figure 3.2: Squirrel SQ2020-2F16 data logger [85]. This device was used to log data from the pyranometer.

### 3.2.2 Measurement Campaign Results (Ambient Light)

The irradiance values presented in Figure 3.3 were taken at the center of the DEP, while the result in Figure 3.4 was measured on a production line further away from the center of the plant. The measurements were taken one day apart, with the second measurement taken on the 13<sup>th</sup> of May, 2015. Observing the raw measurement data, it was evident that the measurement was interrupted and the affected time span was removed from the post processed data. The average irradiance and standard deviation measured at both locations was  $1.20 \pm 0.12 \text{ W/m}^2$  and  $0.98 \pm 0.11 \text{ W/m}^2$ . The weather around the factory during measurement was sunny, as readings outside varied between  $400 \text{ W/m}^2$  and  $600 \text{ W/m}^2$ . Using the average irradiance ( $E$ ) at the plant, an assumed efficiency ( $\eta_{PV}$ ) of 14.1% for a DSSC from GCell [86], PV cell area ( $A$ ) of  $25 \text{ cm}^2$ ,  $350 \mu\text{W}$  can be realized using eqn. (3.1).

$$P_{DC} = \eta_{PV} E A \quad (3.1)$$

Additional indoor irradiance values from HSSMI and the 5GRC were obtained using the same measurement setup and procedure. The average irradiance obtained from both office spaces were  $1.53 \text{ W/m}^2$  and  $1.96 \text{ W/m}^2$ . The irradiance values from HSSMI and 5GRC are presented in Appendix A.

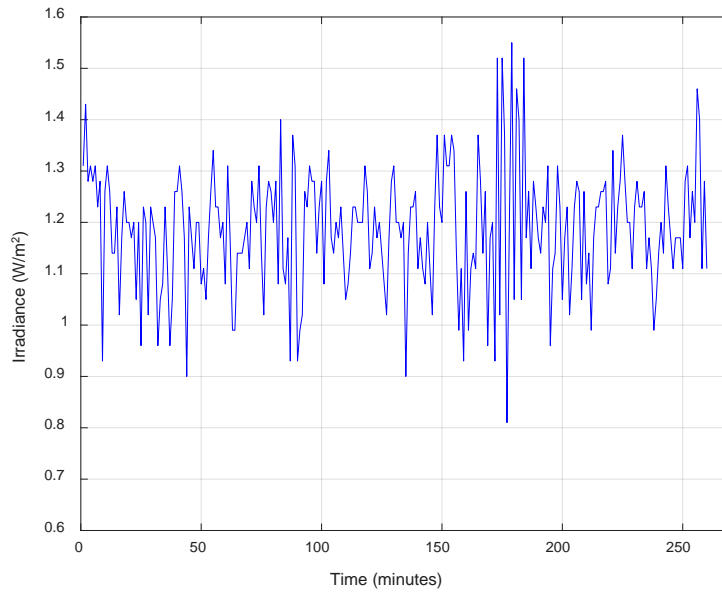


Figure 3.3: Irradiance measurement at a center location at the automobile plant. This measurement was taken between 10:45 AM and 3:30 PM. The Figure shows irradiance values with interruptions excluded.

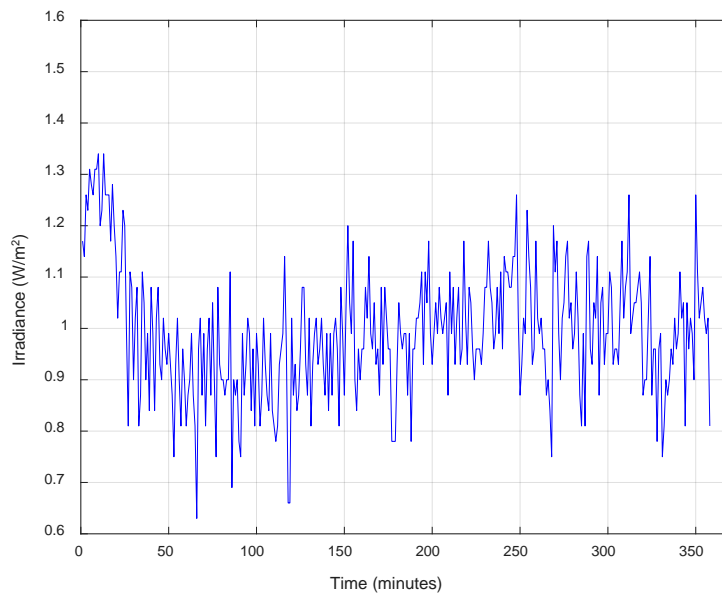


Figure 3.4: Second Irradiance measurement at the automobile plant. This measurement was taken between 11:00 AM and 5:00 PM. The Figure shows irradiance values with interruptions excluded.

### 3.3 Ambient Temperature Measurements

#### 3.3.1 Ambient Temperature Measurement Procedure

Temperature measurements at the DEP were taken using a contactless infrared thermometer (Calex PYROPEN-E shown in Figure 3.5) at six locations. These locations were at the start and end of three production lines. Complying with the health & safety standards at the DEP, the thermometer was held at 30 cm away from the machine parts on the production lines. The average ambient temperature around the production lines characterized was 24.50 °C.

#### 3.3.2 Measurement Campaign Results (Ambient Temperature)

In Table 3.1, the temperature readings obtained at the DEP are presented. The maximum and average temperature difference recorded was 10 °C and  $3.45 \pm 2.96$  °C. Depending on the COTS thermal harvester adopted, the respective performance data can be used to estimate the obtainable DC power. For example, the TGP-751 (from Micropelt energy harvesting [73]) will generate 1000  $\mu$ W at 10 °C temperature difference and 80  $\mu$ W at the average temperature difference recorded. Prior to the measurement campaign at the DEP, the operating temperature of a vertical cutting mill at the Ford training institute generated a temperature difference of 4 °C<sup>3</sup>.



Figure 3.5: Calex PYROPEN-E infrared thermometer [87].

---

<sup>3</sup>The Ford training institute is located in the same building as HSSMI on the ground floor

Table 3.1: Summary of temperature measurements at the DEP

Production line	Temperature at the start of the production line (°C)	Temperature at the end of the production line (°C)
Engine assembly	26.00	35.00
Engine crankshaft	21.50	22.10
Engine block	25.90	22.60

## 3.4 Ambient Radio Frequency Measurements

### 3.4.1 Radio Frequency Measurement Procedure

Estimating the electromagnetic field at any given point requires E-field measurements in more than one polarisation. This is due to the possibility that the orientation of the transmitted wave might have changed due to propagation characteristics (e.g. reflection, shielding and refraction). In the literature, horizontal and vertical polarization components of the electric field are measured and vectorial combination is used to sum the respective components [75, 76, 78, 79, 88]. As a result, dual-polarization measurements with vector combination were used in the measurement campaign to estimate input RF power density at five locations on the factory floor. The E-field displayed on the spectrum analyser was converted to RF power density by using eqns. (3.2) to (3.4), where  $E_{dB\mu V/m}$  is the E-field displayed on the spectrum analyser,  $AF$  is the antenna factor <sup>4</sup>,  $L_{cable}$  is the cable loss,  $E_{Volts/m}$  is the electric field in volts/m,  $P_d$  is the input RF power density in dBm/cm<sup>2</sup>. It is noteworthy that some authors use both survey techniques (spectrum analyser or probe/display) [81, 83], depending on the measurement purpose or for result comparison. While most of these measurement campaigns use “max-hold” trace technique on the spectrum analyzer, other measurement procedures adopt an averaging method [76, 78]. The “max-hold” trace records the highest occurring value of the electric field per frequency during a sweep. This gives rise to a scenario whereby the

<sup>4</sup>The antenna factor is used to estimate the electric field strength that generates 1 Volt at the antenna terminals.

power density is being over estimated. The “average-mode” trace technique shows an instantaneous value of the signal at the end of the frequency sweep by taking the average of a trace point and its prior reading.

$$E_{dB\mu V/m} = E_{dB\mu V} + AF - L_{cable} \quad (3.2)$$

$$E_{Volts/m} = 10^{((E_{dB\mu V/m} - 120)/20)} \quad (3.3)$$

$$P_d(mW/cm^2) = \frac{(E_{Volts/m})^2}{3770} \quad (3.4)$$

The setup adopted in this measurement campaign is made up of a log-periodic antenna (EM-6947 from Electro-metrics; 6dBi gain), Rhode & Schwarz (R&S) ESPI-7 spectrum analyser and a PC: see Figure 3.6. On the spectrum analyser, both “max-hold” and “average-mode” sweeps were activated while the antenna was rotated manually in a similar way to [75] for horizontal and vertical polarization. In order to ensure that sufficient detail was extracted during the frequency sweep, a resolution bandwidth (RBW) of 100 kHz was used. The RBW selected across the band covered is less than the carrier spacing in GSM 900, GSM 1800, UMTS, DTV, and Wi-Fi. In addition to the RBW, the sweep time was set to 37 seconds and the number of frequency points on the spectrum analyser was 2801. These settings align with the recommendation in [79], which ensures that the spectrum analyser is able to evaluate each of the RAT carriers independently. The measurement locations selected for this campaign were chosen based on access to mains power and health and safety requirements at the DEP. In Figure 3.7 the measurement locations are shown with respect to a rectangular floor plan that depicts the factory floor (527 m by 305 m). The selected measurement locations are a subset of possible locations where wireless sensors can be placed. Measurements were taken during the day while production lines were in operation. On the factory floor, different production lines for engine crank, engine block, engine heads and engine assembly were active during the measurement. These production lines have fixed and moving machines, which are made of metals and alloys such as steel. These materials affect RF propagation characteristics by introducing time dispersion in the wireless channel. All RF measurements presented in this sub section were taken either close to a production line or a pedestrian path.

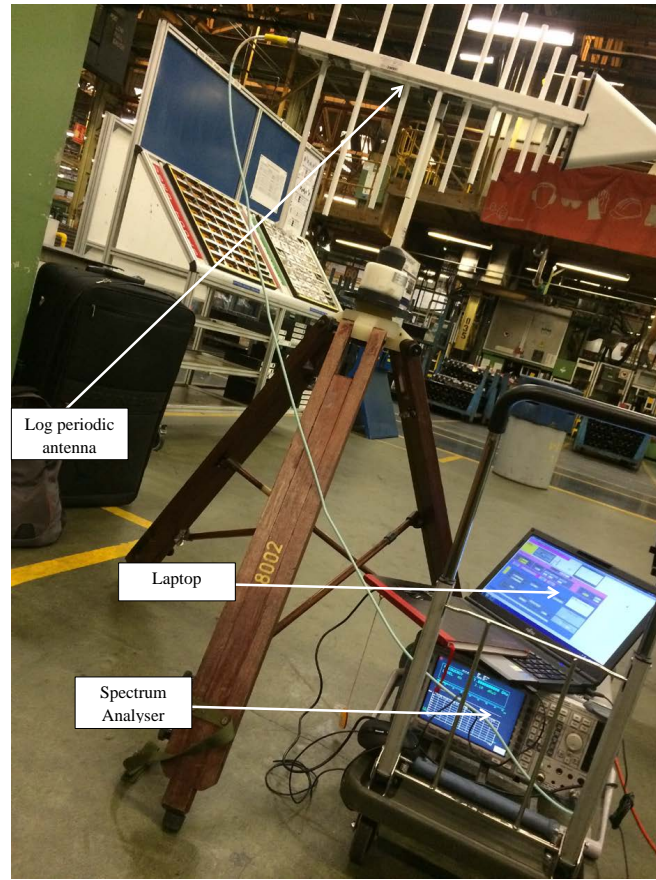


Figure 3.6: Input RF power density measurement setup at the DEP.

### 3.4.2 Radio Frequency Measurement Campaign Results

Comparing the measurement data with widely known RF power density measurement campaigns in the UK as shown in Table 3.2, it can be seen that the input RF power density levels for GSM and 3G inside the plant are three to four orders less than the results presented in [74] and [5]. However, the indoor measurement results in [5] (taken at Southampton, UK ) were obtained near a window. Apart from GSM 1800, where the measurement at the DEP exceeds those presented in [5], the ambient RF power density at the DEP is low in comparison to [5, 74]. This large difference in the measurement results is primarily due to the location of the DEP, as the mobile network coverage in this area is poor. Moreover, the results in [74] were obtained outside underground stations in London where mobile coverage is good due to the dense macrocell installations.

Table 3.2: Comparison of maximum indoor RF power density levels at the DEP

RATs	Frequency (MHz)	This work (dBm/cm <sup>2</sup> ) max-hold	[74] (dBm/cm <sup>2</sup> ) max-hold	[5] (dBm/cm <sup>2</sup> ) max-hold	This work (dBm/cm <sup>2</sup> ) average mode
Digital TV	470-610	-80	-80	-	-100
GSM 900	880-960	-90	-37	-50	-111
GSM 1800	1710-1880	-70	-40	-79	-95
3G	1320-2170	-88	-50	-62	-97
Wi-Fi	2400-2500	-70	-70	-86	-101

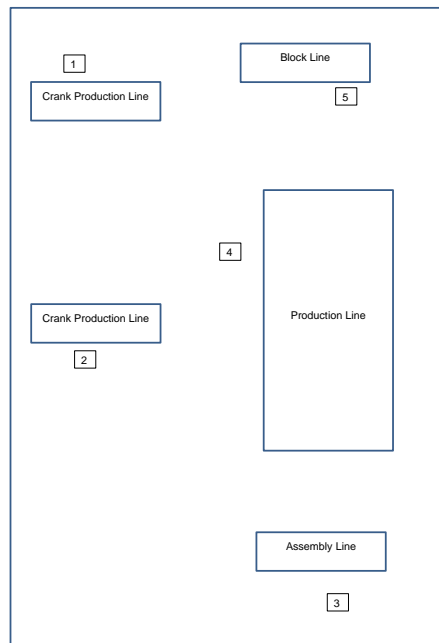


Figure 3.7: Sketch of RF power density measurement points at the automobile factory.

In Figures 3.8 to 3.12, the vector combination of the input RF power density at the measurement locations are presented<sup>5</sup>. From the measurement results, it can be observed that the recorded power density using the “max-hold” trace technique varied over a wider range for horizontal and vertical polarization. For example, at Location 1 the Wi-Fi and GSM 1800 signals measured in both polarizations vary up to 20 dB/cm<sup>2</sup>. Using the “average-mode”, the variation in horizontal and vertical polarization measurements drops to less than 5 dB/cm<sup>2</sup>. At other locations where measurements were taken, the

<sup>5</sup>The RF power density measured at each location for both polarizations using average and max-hold is presented in Appendix B



strength of the Wi-Fi signal received fluctuated due to the locations of the Wi-Fi AP. The dominant frequency across the plant was GSM-1800 and 3G, which agrees with the results presented in [89]. The results of the “average-mode” trace have been used for design considerations within this thesis, since it provides a more realistic estimate of the input RF power density at the plant. However, max-hold measurements were recorded at each of the measurement locations. With respect to the base station and mobile transmit channels, the measurements at the plant also showed that the mobile transmit band had higher peak ambient powers than the base station downlink channel (as seen at Locations 1, 2 and 3 ). This is due to the number of active mobile phones around the measurement location and the distance to the 3G base station. Upon inspecting the power density values presented, it is evident that ambient RF energy harvesting is not feasible at the plant. This is essentially due to the distance from nearby base stations. In addition, the building materials and the presence of metallic objects also contribute to the EM wave attenuating effect experienced at the plant. Using the field trials carried out at Imperial College, London, as a benchmark [74], the least input power required to cold start an ultra-low power management module (PMM) was -25 dBm. Based on the measurement results, a realistic power density (of -87 dBm/cm<sup>2</sup> from the “average-mode” results) and a RF-DC conversion efficiency of 50%, a 62 dBi gain antenna will be required to generate 5  $\mu$ W at the output terminal of a radio frequency energy harvester (RFEH). Moreover, the rectenna will have to be in the optical line-of-sight of the transmitter due to the pencil shaped beam. This makes ambient RF energy harvesting unrealistic based on the available power density available at the DEP. The antenna gain, effective aperture, power density, output power and operating wavelengths are related using eqns. (3.5) to (3.7), where  $A_e$  is the effective aperture,  $\lambda$  is the wavelength,  $G_{fm}$  is the antenna gain at the mid-band frequency,  $P_{RF}$  is the input RF power of the RFEH,  $S$  is the input RF power density,  $P_{DC}$  is the out DC power of the RFEH,  $\eta_{RF-DC}$  is the RF-DC conversion efficiency.

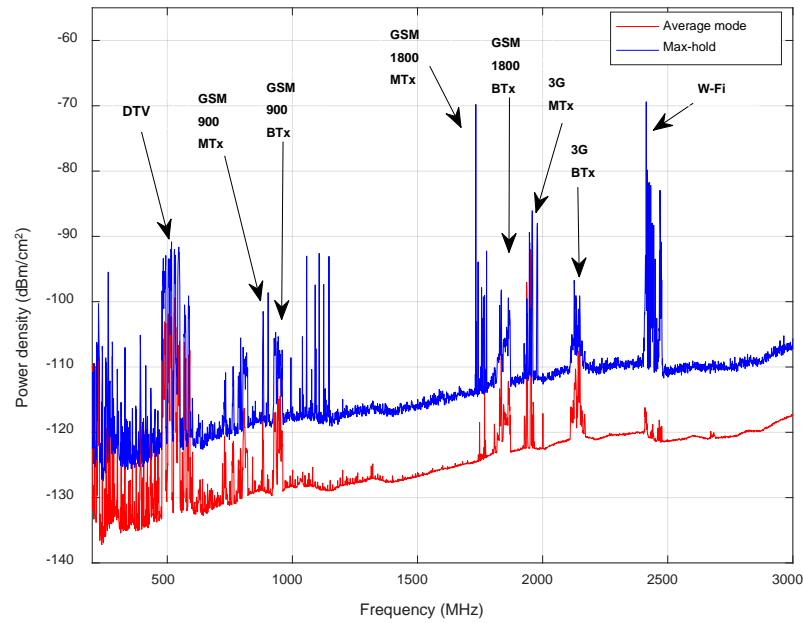


Figure 3.8: Input RF Power density at Location 1 at the DEP. This result shows the vector combination of horizontal and vertical polarization for average and max-hold modes.

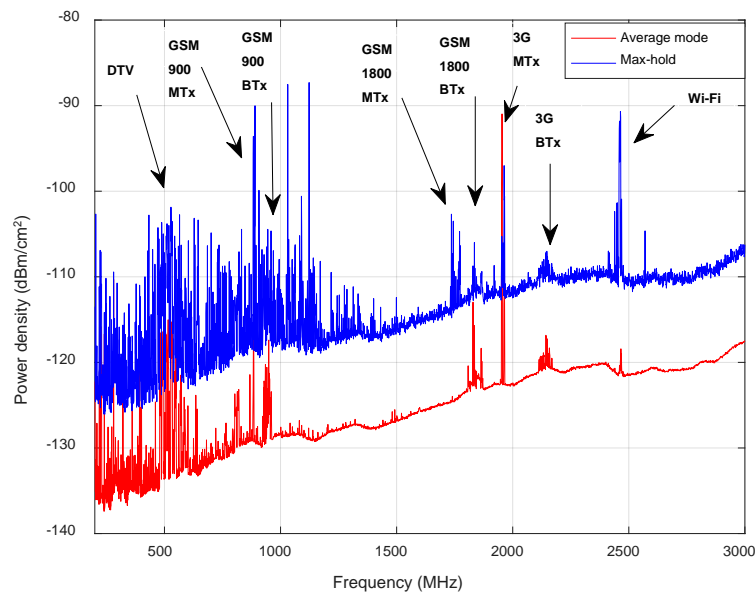


Figure 3.9: Input RF Power density at Location 2 at the DEP. This result shows the vector combination of horizontal and vertical polarization for average and max-hold modes.

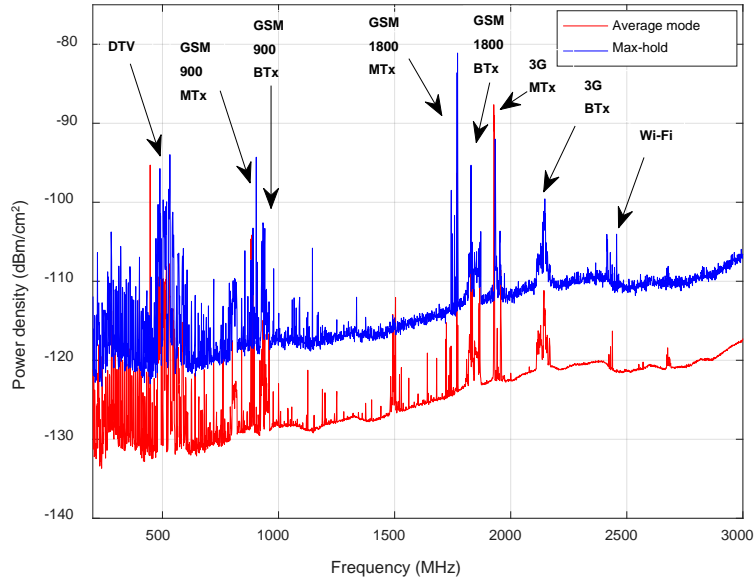


Figure 3.10: Input RF Power density at Location 3 at the DEP. This result shows the vector combination of horizontal and vertical polarization for average and max-hold modes.

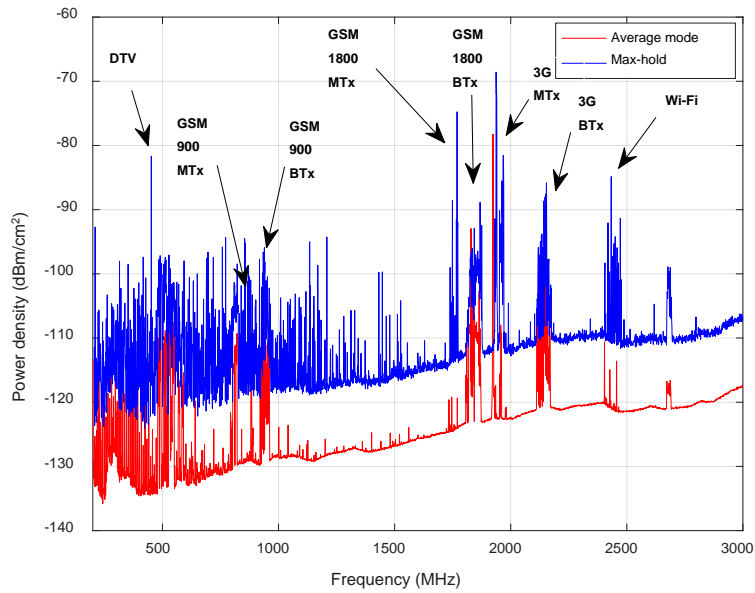


Figure 3.11: Input RF Power density at Location 4 at the DEP. This result shows the vector combination of horizontal and vertical polarization for average and max-hold modes.

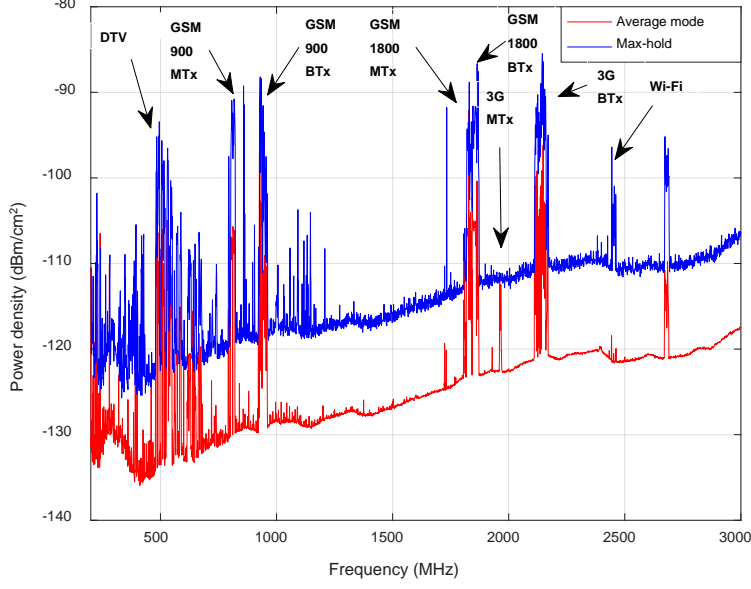


Figure 3.12: Input RF Power density at Location 5 at the DEP. This result shows the vector combination of horizontal and vertical polarization for average and max-hold modes.

$$A_e = \frac{\lambda^2 G_{fm}}{4\pi} \quad (3.5)$$

$$P_{RF} = S A_e \quad (3.6)$$

$$P_{DC} = \eta_{RF-DC} P_{RF} \quad (3.7)$$

However theoretically, an increased amount of power can be harvested by designing the antenna to resonate across an entire band or multiple bands as seen in multi-band rectennas [90–93]. Wideband antennas are able to capture RF waves across a wide bandwidth, compared to the narrowband antennas assumed in the calculation above. Adopting a wideband antenna and matching circuit, provides the opportunity to increase the RF power available at the input terminals of the rectifying circuit. Using the recommendation in [74], the RF channel power density across the respective RATs present at the DEP has been calculated in MATLAB and presented in Table 3.3 to 3.7 for the locations investigated. Given the banded power density, estimates can be made for the received power available to the rectifier circuit. From the banded power density results presented in Tables 3.3 to 3.7, it is evident that this solution increases the available ambient RF

power available to the rectenna, however it still proves ineffective. This is because COTS PMMs require incident RF power several orders more than the values presented.

Table 3.3: Banded Input RF Power density at Location 1

RATs	Frequency (MHz)	Average-mode (dBm/cm <sup>2</sup> )	Max-hold (dBm/cm <sup>2</sup> )
Digital TV	470-610	-78.00	-67.89
GSM-900 (MTx)	880-915	-99.96	-84.21
GSM-900 (BTx)	925-960	-93.35	-83.26
GSM-1800 (MTx)	1710-1785	-94.19	-59.78
GSM-1800 (BTx)	1805-1880	-88.27	-77.22
3G (MTx)	1920-1980	-76.57	-68.34
3G (BTx)	2110-2170	-85.98	-76.50
Wi-Fi	2400-2500	-90.29	-57.77

Table 3.4: Banded Input RF Power density at Location 2

RATs	Frequency (MHz)	Average-mode (dBm/cm <sup>2</sup> )	Max-hold (dBm/cm <sup>2</sup> )
Digital TV	470-610	-91.81	-78.81
GSM-900 (MTx)	880-915	-100.37	-76.45
GSM-900 (BTx)	925-960	-98.55	-85.71
GSM-1800 (MTx)	1710-1785	-95.60	-82.76
GSM-1800 (BTx)	1805-1880	-92.78	-82.62
3G (MTx)	1920-1980	-78.62	-80.71
3G (BTx)	2110-2170	-91.68	-81.30
Wi-Fi	2400-2500	-90.91	-72.80

Table 3.5: Banded Input RF Power density at Location 3

RATs	Frequency (MHz)	Average-mode (dBm/cm <sup>2</sup> )	Max-hold (dBm/cm <sup>2</sup> )
Digital TV	470-610	-85.28	-74.50
GSM-900 (MTx)	880-915	-87.42	-82.44
GSM-900 (BTx)	925-960	-96.04	-84.29
GSM-1800 (MTx)	1710-1785	-85.71	-68.92
GSM-1800 (BTx)	1805-1880	-88.87	-78.86
3G (MTx)	1920-1980	-73.13	-76.91
3G (BTx)	2110-2170	-89.08	-78.16
Wi-Fi	2400-2500	-90.94	-79.56

Table 3.6: Banded Input RF Power density at Location 4

RATs	Frequency (MHz)	Average-mode (dBm/cm <sup>2</sup> )	Max-hold (dBm/cm <sup>2</sup> )
Digital TV	470-610	-84.71	-72.83
GSM-900 (MTx)	880-915	-99.12	-84.59
GSM-900 (BTx)	925-960	-86.57	-77.32
GSM-1800 (MTx)	1710-1785	-95.17	-64.35
GSM-1800 (BTx)	1805-1880	-79.58	-70.76
3G (MTx)	1920-1980	-63.09	-54.62
3G (BTx)	2110-2170	-76.23	-66.84
Wi-Fi	2400-2500	-90.25	-72.50

Table 3.7: Banded Input RF Power density at Location 5

RATs	Frequency (MHz)	Average-mode (dBm/cm <sup>2</sup> )	Max-hold (dBm/cm <sup>2</sup> )
Digital TV	470-610	-83.60	-72.91
GSM-900 (MTx)	880-915	-103.60	-90.61
GSM-900 (BTx)	925-960	-79.22	-69.23
GSM-1800 (MTx)	1710-1785	-95.34	-79.99
GSM-1800 (BTx)	1805-1880	-77.34	-66.55
3G (MTx)	1920-1980	-92.68	-84.00
3G (BTx)	2110-2170	-75.69	-64.72
Wi-Fi	2400-2500	-91.06	-69.60

### 3.5 Summary

This chapter has presented measurement data from an automobile plant in the UK. The measurement outcome showed that indoor lighting and temperature differences between machine parts on the production lines could be harvested. Indoor light from fluorescent tubes was dominant during the measurement as the irradiance values obtained outside the factory during the day were two orders greater than the indoor values, which aligns with the literature. Moreover, this shows that the long term irradiance values can be predicted, since indoor lighting at the plant is kept ON throughout the day. While the temperature differences measured are sufficient for COTS TEGs, ambient temperature will fluctuate at different times of the year. Consequently, affecting the estimated harvestable power

profile that can be obtained using thermal energy harvesters. As a result of the location of the automobile plant and the mobile network coverage in the vicinity, the ambient RF power levels recorded are not sufficient for energy harvesting.

Due to the insufficient ambient RF power recorded during the measurement campaign, RF power transport can be adopted by using intentional radiators (IRs). IRs can be placed within factory spaces for the sole purpose of augmenting the available ambient RF power. In order to model the radio coverage area of IRs, site-specific deterministic modeling techniques are required. In Chapter 4, details of a measurement campaign at a University machine workshop is discussed. This workshop contains inventory that can be found in factories.

# Chapter 4

## Wideband Channel Measurement

In this chapter, wideband channel measurement results from a machine workshop are presented. The machine workshop is located at the Wolfson school of Mechanical, Electrical and Manufacturing Engineering, Loughborough University. The frequency selectivity of the channel over 2.3 - 2.5 GHz (ISM band) was obtained by using a frequency domain channel sounding method discussed in Section 4.2. The measurement settings discussed in Section 4.3 were selected so as to prevent distortion of the received signal. In Section 4.5, details of the accompanying ray tracing model of the machine workshop are discussed. Section 4.6 presents the measurement and ray tracing results as well as the delay spread distance relationship. The measurement campaign discussed in this chapter was used to evaluate the performance and suitability of the commercial propagation software used.



## 4.1 Introduction

Wireless channel measurements can be carried out in different ways depending on the wireless application, some of which are [36]:

1. *Spatial measurements* whereby the transmitter or receiver is moved to different locations separated by several wavelengths (greater than  $10\lambda$ ).
2. *Local measurements* whereby the transmitter or receiver is moved around a specific location over wavelengths much less than  $10\lambda$ .
3. *Traffic-effect or temporal measurements* whereby the transmitter and receiver are fixed and measurements are carried out with movements occurring between the transmitter and receiver.
4. *Partitioned measurements* whereby the effects of hard and soft partitions are investigated.
5. *Frequency-dependent measurements* whereby the channel characteristics are measured at different frequencies.
6. *Angle-of-arrival measurements* whereby the angle of arriving MPCs are characterized.
7. *Time-of-arrival measurements* whereby the arrival time of the MPCs are measured.

With respect to site specific deterministic modelling, ray tracing results have been compared with channel measurements in the literature [60, 94–100]. Ray tracing techniques provide a measurement alternative for determining large and small-scale radio propagation effects. In [60, 94, 98–100], ray tracing was used to obtain parameters such as path gain; path loss; Rician K-factor; received power and rms delay spread, which account for both propagation effects. Ray tracing for modelling large-scale fading was investigated in [95, 96] while small-scale effects were considered in [97]. The environments considered in the literature presented were indoor locations such as offices, electronic laboratories or a merchant ship in [99]. In contrast to the environments surveyed, the ray tracing model in this chapter investigates a multipath rich environment. With respect

to the materials adopted in the ray tracing models, concrete was used for floor and ceiling; plasterboard for open office plan separation; plywood for table tops and glass for doors. These material definitions have been adopted in the ray tracing model presented in Section 4.6. Objects in ray tracing models are usually an approximate representation of the floor plan and inventory. As a result, the ray tracing model is usually tweaked by adjusting material definitions, specifying number of reflections and diffractions or by evaluating diffuse scattering [60, 94]. Regarding diffuse scattering, the authors in [97] noted that at millimetre wave frequencies, the effect of diffuse scattering in the ray tracing model is negligible, since the objects become larger than the wavelength. However, in [94], second order diffuse scattering improved the accuracy of the simulation of rms delay spread and received power. It is noteworthy that it had no effect on the maximum excess delay reported. In Figure 4.1, a pictorial illustration of propagating paths in a ray tracing model is shown.

The rms delay spread is defined as the second moment of the PDP and can be obtained from eqns. (4.1) to (4.3), where  $N$  is the number of MPCs in the profile,  $P_n$  and  $\tau_n$  are the power and time delay of the  $n^{th}$  MPC. Consequently, it becomes a critical design factor for wireless transceivers [34]. From the delay spread expression, it can be seen that  $\tau_{rms}$  depends on the power ratios and difference in time delays and not the transmit power [60].

$$\tau_{rms} = \sqrt{\overline{\tau^2} - \bar{\tau}^2} \quad (4.1)$$

$$\bar{\tau} = \frac{\sum_{n=1}^N P_n \tau_n}{\sum_{n=1}^N P_n} \quad (4.2)$$

$$\overline{\tau^2} = \frac{\sum_{n=1}^N P_n \tau_n^2}{\sum_{n=1}^N P_n} \quad (4.3)$$

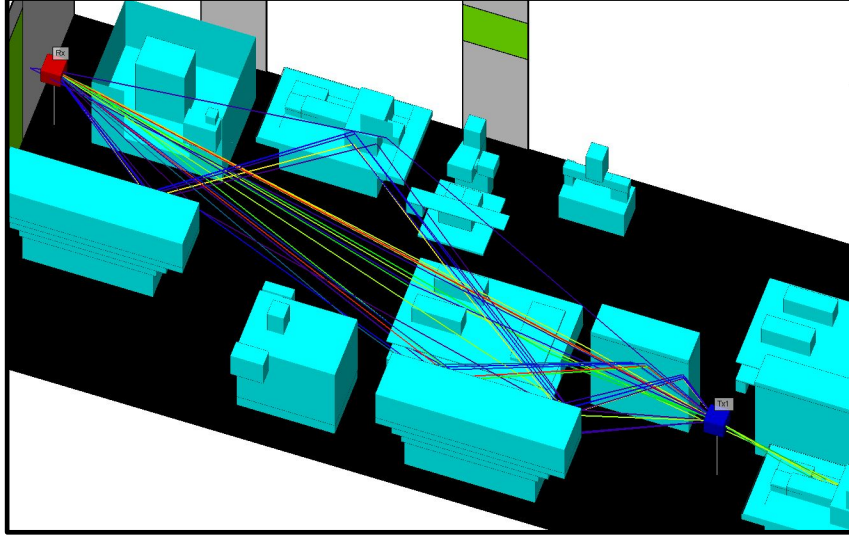


Figure 4.1: Three-dimensional visualisation of direct, reflected and diffracted rays in a LoS setup from  $T_x$  (blue) to  $R_x$  (red).

In order to compare the performance of the deterministic models, the mean absolute percentage error (MAPE) of the channel sounding and ray tracing modelling results are summarized in Section 4.5, where the results from the measurement campaign will be put in context with the literature. In general, channel characteristics can be obtained either in the time domain or frequency domain. In the time domain, the impulse response ( $h(\tau)$ ) is obtained by probing the channel with a narrow pulse, while in the frequency domain, the channel transfer function (CTF) is post processed using a window function and the inverse Fourier transform. In this chapter, only vertical polarization measurement and simulations were investigated. This is due to the radiation pattern of the omnidirectional antennas used in both the measurement campaign and the ray tracing model. In horizontal polarization measurements or simulations, the power radiated by the antenna is directed towards the floor and the ceiling.

## 4.2 Channel Sounding Techniques

Time domain channel measurements can be carried out either by transmitting a spread-spectrum signal and correlating the signal received with the transmitted sequence or by

transmitting a short pulse across the wireless channel. In both time domain cases, phase information of the MPC is not available due to the envelope detection at the receiver [34, 36].

#### 4.2.1 Direct RF Pulse (Time Domain) Channel Sounding

The direct pulse measurement setup shown in Figure 4.2 is made up of a probing pulse generator with pulse width  $T_{bb}$  and repetition  $T_{rep}$ , RF sweep oscillator and power amplifier at the transmitter. At the receiver, the pulse is detected using an envelop detector and stored in a digital storage oscilloscope (DSO). While the envelop detector ignores phase information of the MPCs, a coherent detector can be used in order to retain phase of the MPCs. One of the disadvantages associated with this time domain technique is its high peak to average power operation of the amplifiers used in the transmit RF chain. In addition, it is susceptible to noise and interference due to the pass band filter at the receiver RF front end. The pulse repetition period  $T_{rep}$  is the maximum detectable delay and the delay resolution is equal to the probing pulse width  $T_{bb}$ . In the literature, this technique has been used by various authors for obtaining channel characteristics [39, 101, 102].

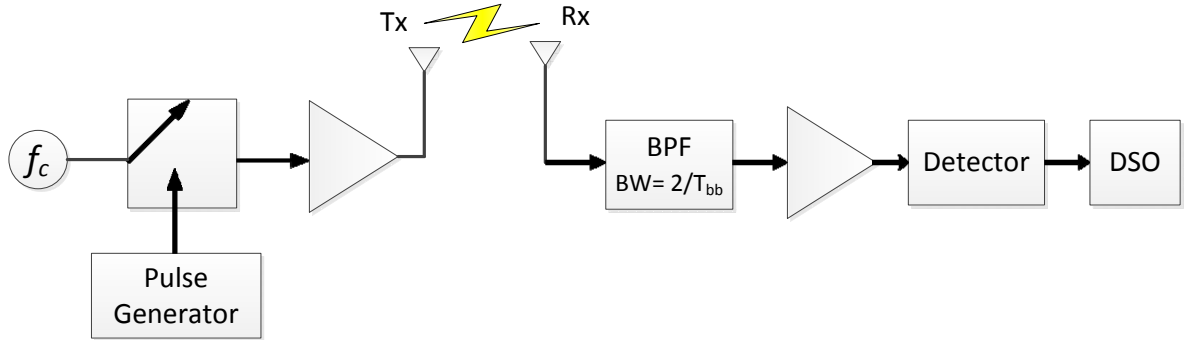


Figure 4.2: Direct RF pulse time domain channel sounding measurement system.

#### 4.2.2 Spread spectrum Channel Sounding

##### Sliding Correlator

The block diagram of a sliding correlator channel sounder is shown in Figure 4.3. In this channel sounding technique, the carrier signal is spread over a large bandwidth by

mixing (*spreading*) the signal with a pseudo-noise (PN) sequence (also known as chips) of chip rate  $V(\text{Hz})$ , which is the inverse of the chip duration [34]. These PN sequences in actuality are binary sequences with amplitude  $\pm 1$ . At the receiver, the signal is filtered and the spreading process is inverted by using a slightly slower PN sequence similar to that used at the transmitter ( $U(\text{Hz})$ ). Autocorrelating the despread signal with a slower PN sequence at the receiver creates a sliding correlator. Given that the incoming MPCs will arrive with different delays, this causes the autocorrelation to peak at different times. Consequently, the channel impulse response convolved with the pulse shape can be displayed on an oscilloscope. The delay resolution using this technique is given by eqn. (4.4), where  $R_c$  is the chip rate of the transmit PN sequence.

$$\Delta\tau = \frac{2}{R_c} \quad (4.4)$$

The advantages of using this method in comparison to the direct RF pulse method is that it can achieve a wider coverage area due to the efficient operation of the power amplifiers, improved dynamic range as well as lower transmit power [34,36]. On the other hand, the time required to slide the PN sequences can introduce errors in estimating the channel, particularly when there are rapid variations in the channel (*fast fading*). Additionally, the use of coherent detector at the receiver does not resolve the problem with retaining phase information of the MPCs. In the literature, this channel sounding technique was used in [103–108].

### 4.2.3 Frequency Domain Channel Sounding

In Figure 4.4, the operating principle of a frequency domain channel measurement system using a vector network analyser (VNA) and frequency/time transformation is presented. The VNA works as a frequency sweeper and obtains  $N$  complex samples of the channel frequency ( $H(k)$ ,  $0 \leq k \leq N$ ) at discrete frequencies  $f_k = f_o + k\Delta f$ ,  $0 \leq k \leq N$ , with equal frequency spacing of  $\Delta f$ . The channel's complex frequency response is also known as the transfer function (i.e. transmissivity  $S_{21}(f)$ ) is evaluated by comparing the transmitted signal on port 1 and the received signal on port 2 of the VNA [34,36]. The response is then converted to time by using the inverse discrete Fourier transform, as the band-limited CTF is sampled at the measurement bandwidth. This method is suitable for

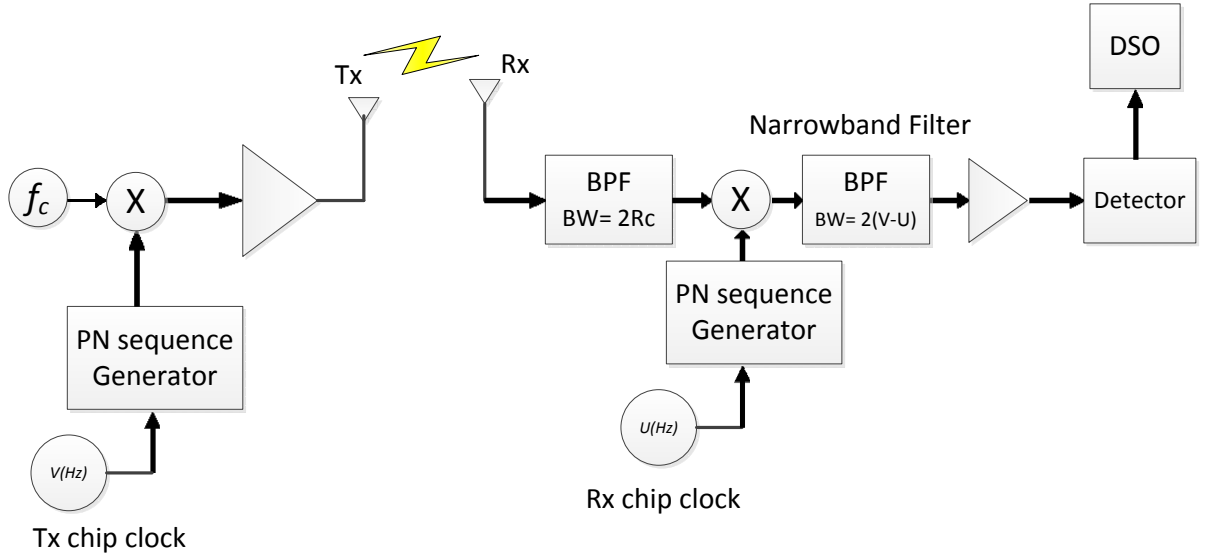


Figure 4.3: Sliding correlator channel sounding measurement system.

locations where the channel frequency response does not change rapidly (slow fading), as the fluctuations can lead to errors in estimating the channel impulse response. The inherent advantage of this method is that amplitude and phase information of the MPCs is recorded. The delay resolution using frequency domain channel sounding is the inverse of the measurement bandwidth and the maximum detectable delay by the system can be calculated using eqn. (4.5), where  $N_p$  is the number of frequency points on the VNA and  $BW$  is the measurement bandwidth.

$$\tau_{max} = \frac{N_p - 1}{BW} \quad (4.5)$$

In the literature, this technique has been widely adopted for indoor wireless channel modelling [109–118].

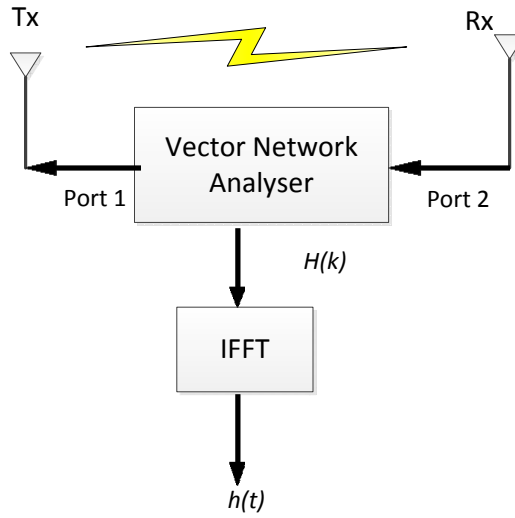


Figure 4.4: Frequency domain channel sounding measurement system.

### 4.3 Wireless Channel Measurement System

The frequency domain channel sounding measurement system was adopted during the measurement campaign. This is because the system is easy to set up and the short  $T_x \rightarrow R_x$  separation distances to be investigated. During the measurement window, the wireless channel in the workshop was quasi static by taking the measurements out of hours.

The measurement system used in this campaign is shown in Figure 4.5, with the physical implementation for a LoS measurement shown in Figure 4.6. The measurement system is made up of a VNA (Agilent E8050A), two wideband vertically polarised omni directional antennas (Electrometrics 6116), a 13 m long cable connecting the receiver antenna to port 2 on the VNA and a 3 m cable connecting the transmitting antenna to port 1 on the VNA. In Appendix C, the antenna gain, and frequency loss graph for the cables are presented. In the transfer function mode, the VNA compares the transmitted signal from port 1 to the received signal on port 2 in order to evaluate the CTF. The frequency band used during the measurement was 2.3 - 2.5 GHz, which falls within the ISM band for wireless local area network (LAN). The maximum equivalent isotropically radiated power (EIRP) of the system was 6.21 dBm, which is below the RF exposure limit. Since the VNA was used for transmitting and receiving simultaneously, the received signal

experiences a frequency shift due to the propagation delay. The frequency shift ( $\Delta F$ ), can be calculated using eqn. (4.6), where  $t_s$  is the sweep time. Taking into consideration  $\Delta F$  and the front end filter on the VNA, the intermediate frequency (IF) bandwidth of the VNA was set to 3 kHz. This setting allows the VNA to detect the shifted received signal without distortion. In Table 4.1, the settings and parameters used for the measurements are presented. With the measurement settings shown in Table 4.1, ( $\tau_{max}$ ) for the system was  $8 \mu s$ , which corresponds to a path resolution of 2400 m. The CTF obtained from the measurements includes the antenna responses of both the transmitting and receiving antennas. Given that the machine workshop inventory creates a rich multipath environment, it can be assumed that the CTF obtained is independent of the MPC directions [119].

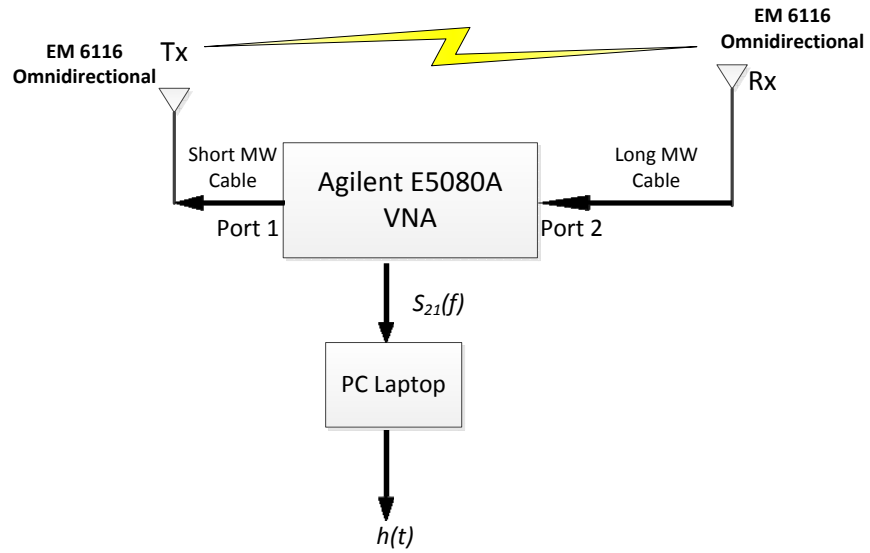


Figure 4.5: Channel measurement system block diagram.



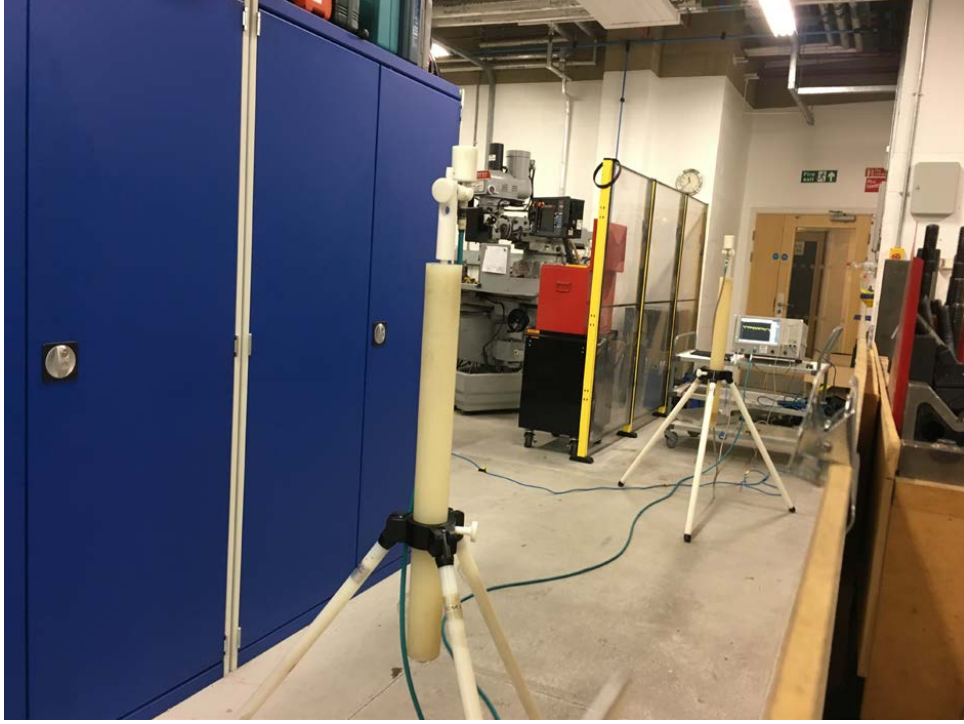


Figure 4.6: Pictorial illustration of the channel measurement setup for a LoS point.

Table 4.1: Measurement setup parameters

Parameter	Value
Frequency points	1601
Sweep time	800 ms
Transmit power	5 dBm
IF bandwidth	3 kHz

$$\Delta F = \left( \frac{\tau_{max}}{t_s} \right) BW \quad (4.6)$$

The link budget for the frequency domain channel sounder at 2.3, 2.4 and 2.5 GHz i.e., the lower, mid-point and upper band of the frequency band for the maximum separation distance of 12 m is presented in Table 4.2. The path loss was calculated using a path loss exponent of 2.81 [37], which represents the worst case scenario for an indoor factory location. From the link budget, the system margin shows that the measurement system was operated above the noise floor. Thus, amplifiers on either the transmit or receive chain were not required.

Table 4.2: Link budget for the frequency domain channel sounder. A 13 m MW cable is connected to the receiver and a 3 m MW cable is connected to the transmitter

Parameter	Values		
	2.3 GHz	2.4 GHz	2.5 GHz
Transmitter power	5.0 dBm	5.0 dBm	5.0 dBm
Transmit cable loss	1.2 dB	1.2 dB	1.2 dB
Transmit antenna gain	1.2 dBi	1.2 dBi	1.2 dBi
Path loss at 12 m	88.8 dB	89.3 dB	89.8 dB
Receive antenna gain	1.2 dBi	1.2 dBi	1.2 dBi
Receive cable loss	4.5 dB	4.5 dB	4.5 dB
Received power	-87.1 dBm	-87.6 dBm	-88.1 dBm
Receiver sensitivity	-136 dBm	-136 dBm	-136 dBm
System margin	48.9 dB	48.4 dB	47.9 dB

## 4.4 Measurement Environment and Procedure

The dimensions of the machine workshop are 17 m by 11 m by 4.5 m. The workshop room is located on the ground floor with concrete ceiling lined with heating, ventilating and air-conditioning (HVAC) pipes. The walls are made of brick and there are metallic enclosures carrying cables from the floor to the roof. The windows are made of glass with metal bars. The workshop room is packed with metallic equipment like lathes, drills, workbenches, and other machine tools as listed in Appendix D. Within the machine workshop, the receiver locations were classified into two topographies, which are: LoS measurements and NLoS measurements. In LoS measurements, there was a visible direct path between the transmitter and receiver, while NLoS topographies were as a result of obstructions introduced by machine parts, metallic cupboards or pillars. Using a practical inter sensor node distance from [99, 120], the  $T_x \rightarrow R_x$  separation distance for both LoS and NLoS receiver locations were between 2 and 12 m. Prior to the measurements, the VNA was calibrated using a full 2-port calibration method. The calibration process removes the measurement errors generated by the connectors and MW cables. During the measurement campaign, the transmitter was fixed while twelve receiver locations (as shown in Figure 4.7) were used to obtain LoS and NLoS delay spread.

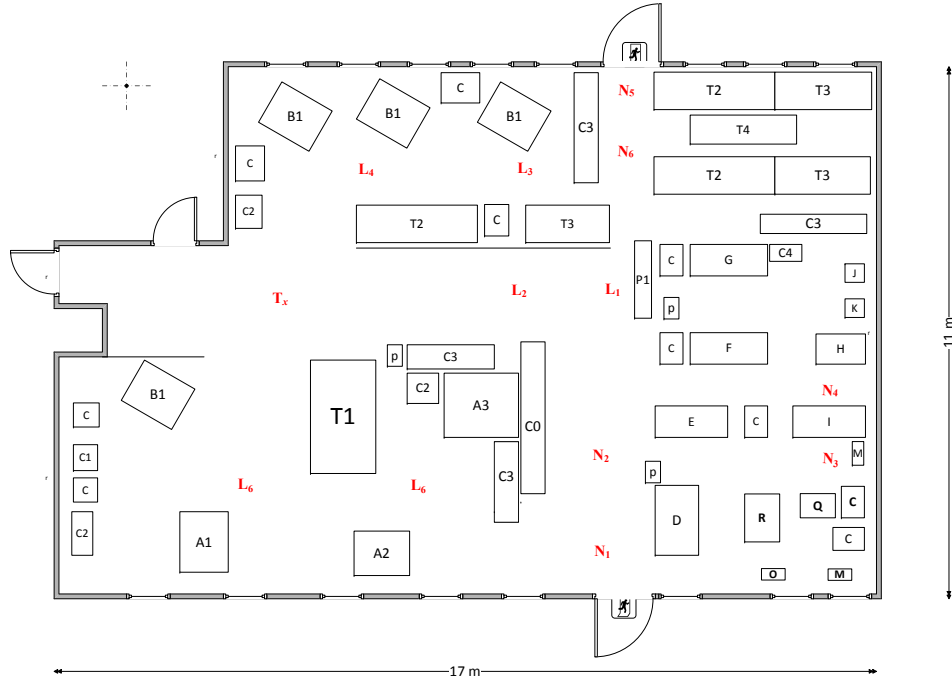


Figure 4.7: Loughborough University Machine Workshop Layout. The floor plan shows the transmitter and receiver locations. The six LoS and NLoS receiver locations are represented as  $L_i$  and  $N_i$ .

## 4.5 Machine Workshop Ray Tracing Model

The ray tracing model of the machine workshop was implemented in a commercial ray tracing software (Wireless Insite [121]). In the ray tracing model shown in Figure 4.8, the following material definitions were used: concrete for the floors and ceiling, brick for the walls, glass for the windows and the entrance door. The model also includes two metal doors represented with exit signs. In Figure 4.8, metal boxes are used for overhead HVAC pipes and pillars. The HVAC pipe layout and ceiling is set to invisible in order to aid visual inspection of the inventory. The workshop inventory is representative of factory environments and includes large and small metal objects (such as mills, lathes, workbenches, carts, drawers, shelves) that are found in factories. The simulation settings and parameters for the ray tracing model are summarized in Table 4.3.

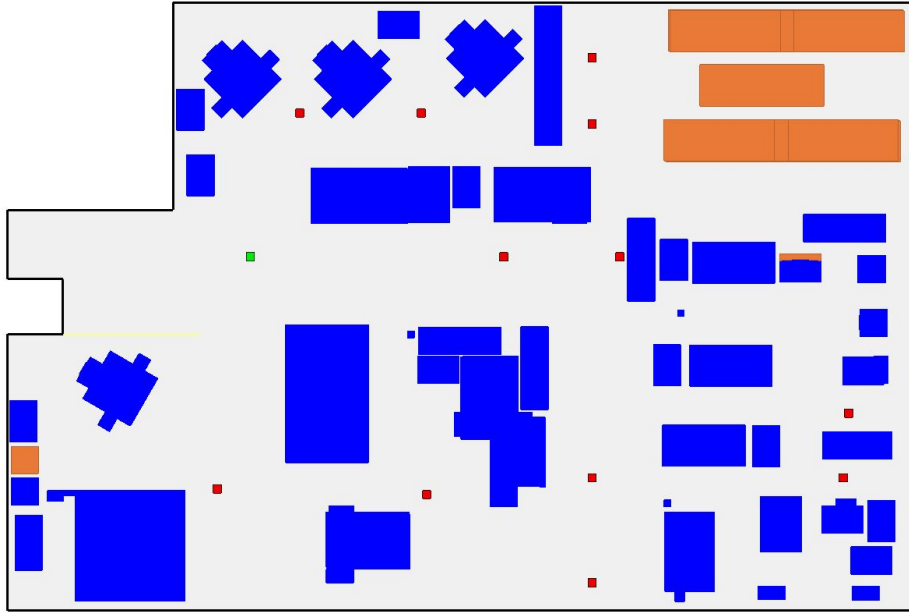


Figure 4.8: Top view of Loughborough University machine workshop ray tracing model. In the figure, blue objects are defined as PEC, brown objects are defined as wood and the yellow line represents a glass partition.

Table 4.3: Ray tracing model parameters

Parameter	Value
Frequency band	2.3 - 2.5 GHz
Antenna type	$\lambda/2$ dipoles
Transmitter Antenna gain	2 dBi
Receiver Antenna gain	2 dBi
Transmitter power	0 dBm
Number of reflections	6
Number of diffractions	2
Number of transmissions	2
Ray tracing method	SBR
Ray spacing	0.25 degrees
Signal waveform	Sinusoidal
Antenna polarisation	Vertical

## 4.6 Measurement Results and Ray Tracing Comparison

The delay vs power relationship of the CTF was obtained by using the time domain mathematical option on the VNA. This option implements the IFFT process to obtain time dispersion of the channel. So as to suppress the effect of the band limited IFFT, a Kaiser window with  $\beta = 7$  (as recommended in [119]) was applied to the CTF. Moreover, this window option allows MPCs to be identified by reducing energy dispersion into subsequent delay bins. A 30 dB threshold was applied to the profiles obtained from the measurement system and the ray tracing software. This threshold excludes MPCs that are 30 dB below the strongest MPC. To make a fair comparison between the delay spread results obtained from the VNA and the predictions made by Wireless Insite, a common maximum excess delay ( $t_\eta$ ) was applied <sup>1</sup>. The excess delay was selected from the ray tracing profile for each receiver location. Thus, the  $\tau_{rms}$  obtained from both the VNA and Wireless Insite were from 0 to  $t_\eta$ .

The  $\tau_{rms}$  obtained from the VNA measurements and Wireless Insite are presented in Table 4.4 and Table 4.5 compares the error measures obtained with the literature <sup>2</sup>. The error measures were calculated using eqn. (4.7), where  $A_i$  is the measured value,  $B_i$  is the ray tracing value,  $n$  is the number of measurement points. In general, ray tracing simulations are regarded as accurate and representative of the measurement when the path loss and delay spread predictions at the receiver locations are within 5 dB and 20 ns [100, 124].

$$MAPE = \frac{100}{n} \sum_{i=0}^n \left| \frac{A_i - B_i}{A_i} \right| \quad (4.7)$$

---

<sup>1</sup>The ray tracing and measurement power profiles from which the  $\tau_{rms}$  was calculated from are presented in Appendix E

<sup>2</sup>In the literature [122, 123], this error measure has been used to evaluate the performance of prediction and interpolation tools. In addition, it has been used extensively in weather and stock market forecasting

Table 4.4: Comparison of rms delay spread obtained from VNA and ray tracing model

Path	VNA (ns)	Wireless Insite (ns)
T → L <sub>1</sub>	18.51	15.43
T → L <sub>2</sub>	15.92	15.90
T → L <sub>3</sub>	15.22	11.80
T → L <sub>4</sub>	12.56	12.99
T → L <sub>5</sub>	17.76	13.29
T → L <sub>6</sub>	15.57	11.46
T → N <sub>1</sub>	19.07	13.39
T → N <sub>2</sub>	21.94	15.10
T → N <sub>3</sub>	21.97	19.92
T → N <sub>4</sub>	26.76	14.68
T → N <sub>5</sub>	26.44	19.52
T → N <sub>6</sub>	13.22	9.49

Table 4.5: Error measure comparison for measurement and ray tracing prediction

Author	Frequency (GHz)	Parameter	MAPE
This work	2.4	Delay spread	22.13
[100]	1.3	Delay spread	48.81
[98]	2.4	Delay spread	28.39
[95]	2.4	Received power	57.56
[60]	3.5	Delay spread	14.77
[97]	60.0	Delay spread	20.43

In Figure 4.9, the delay spread as a function of distance is presented. The figure shows that the delay spread is larger for NLoS and it increases with distance for both topographies. This phenomenon has been observed in the literature [50, 99, 110, 119].

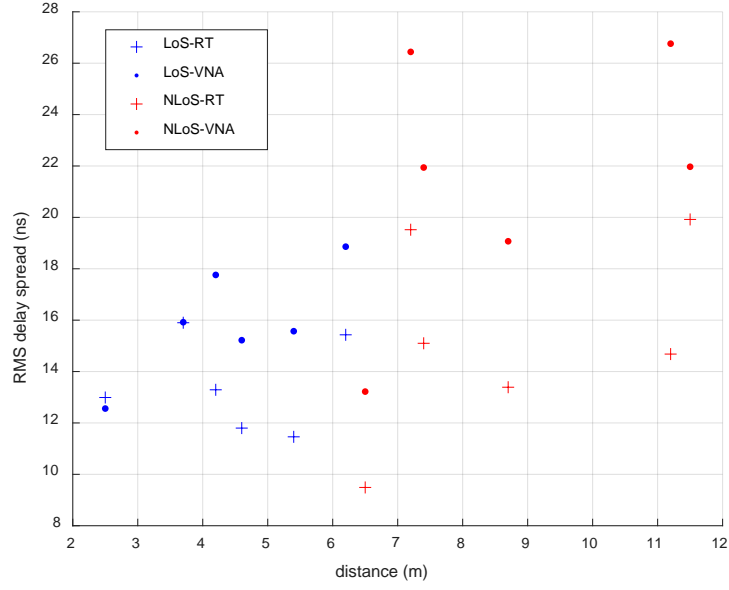


Figure 4.9: RMS delay spread as a function of distance for all VNA measurement and ray tracing simulations.

## 4.7 Summary

The delay spread prediction at each receiver location was within 20 ns. Thus, the ray tracing results in this work can be regarded as accurate and the data obtained from the commercial ray tracing software can be used to estimate the delay spread in indoor locations. The environment investigated in this chapter contrasts with the literature. As a result, the new measurement data can be used to model RF receivers situated in multi-path rich environments like machine workshops. By using ray tracing modelling, it is possible to obtain and analyse wireless channel characteristics without access to the measurement site. The ray tracing commercial software used in this chapter will be adopted in Chapter 5 to deterministically model machine workshop spaces without knowledge of the inventory.

## **Chapter 5**

# **Fractal Based Radio Propagation**

## **Modelling**

In this chapter, a novel fractal laying technique is presented for populating multipath rich environments like machine workshops. The concept of fractals is introduced in Section 5.2 and the fractal laying algorithm is discussed in detail in Section 5.3. In Section 5.4, the Saleh-Valenzuela statistical wideband model is presented. The delay spread for LoS and NLoS topographies using the fractal overlaying technique is presented in form of cumulative density functions (CDF) in Section 5.5 and the statistical features obtained from the model are presented in Section 5.6.



## 5.1 Introduction

Fractals are typically non ending patterns which can occur in nature or can be created mathematically. A “fractal object is self-similar in that subsections of the object are similar in some sense to the whole object” [125]. In general, fractals can be natural or artificial. Naturally occurring fractals could be of the *branching form* or *spiral form*. Some examples of the natural occurring branching fractals are: blood vessels or neurons, lighting bolt, oak trees and natural occurring spiral fractals include: hurricanes, spiral galaxy and the agave cactus plant [126]. Artificial fractals are mathematically generated and some widely known examples include Sierpinski triangle, Cantor set, Sierpinski square and Koch curve. In artificial fractals, subsequent fractal levels or iterations are obtained by recursively evaluating the fractal mathematical algorithm. In the literature, fractals have been applied in medical research [127–132] and antenna designs [133–138].

With respect to modelling factory like spaces without knowledge of the exact inventory, the author in [27] used a physical-statistical approach to model a factory floor space by generating random cluster centres and scatterer locations. The scattering objects in the wireless channel were modelled as finite lossy dielectric cylinders and geometric relations were used to calculate the arrival time of the MPCs. In this regard, this work shows how fractals can be used to rapidly generate inventory in order to populate machine workshops. The mundane task of accurately specifying objects in the ray tracing software has been studied and an algorithm for machine workshops of similar dimensions has been presented. In this thesis, a fractal overlaying rule for placing objects on a machine workshop floor is discussed.

Two University machine workshops were investigated in this thesis. These are: the Mechanical, Electrical and Manufacturing Engineering workshop at Loughborough University and the workshop floor plan at Clemson University presented in [139]. The CDF delay spread obtained from the exact inventory at both sites was compared to the fractal overlaying algorithm on both floor plans. With the help of the fractal overlay algorithm presented, similar spaces can be rapidly modelled using fractal objects. Consequently, increasing the generality and applicability of ray tracing modelling techniques.

## 5.2 2-Dimensional Fractals

The Sierpinski square (also known as Sierpinski carpet) is created by dividing a square into nine congruent squares. The central square is then removed, leaving eight squares as shown in Figure 5.1). Subsequent iterations are created by applying this algorithm to the remainder squares from the previous iteration. For example, in the Sierpinski square, after  $n = 0, 1, 2, 3, 4$  iterations, the number of black squares is equal to 1, 8, 64, 512. The area of the black squares after the  $n^{\text{th}}$  iteration can be calculated using eqn. (5.1) [125, 140].

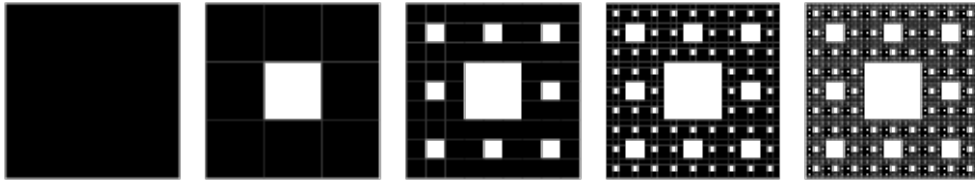


Figure 5.1: A Sierpinski carpet after four iterations [140].

$$\begin{aligned}
 N_n &= 8^n \\
 L_n &= \frac{1}{3^n} \\
 A_n &= L_n^2 N_n \\
 &= \left(\frac{8}{9}\right)^n
 \end{aligned} \tag{5.1}$$

The Sierpinski triangle (also known as Sierpinski sieve) is geometrically created by removing the inverted half-scale copy of the original triangle (as shown in Figure 5.2). By applying this process recursively, the layout for subsequent iterations can be obtained. The fractional area of the black section of the fractal is given by eqn. (5.2), after the  $n^{\text{th}}$  iteration. For the first iteration in the Sierpinski triangle, one-quarter of the area is removed [125, 140]. In eqns. (5.1) and (5.2),  $N_n$  is the number of black squares or triangles and  $L_n$  is the length of a white triangle or square.

$$\begin{aligned}
 N_n &= 3^n \\
 L_n &= \frac{1}{2^n} \\
 A_n &= L_n^2 N_n \\
 &= \left(\frac{3}{4}\right)^n
 \end{aligned} \tag{5.2}$$

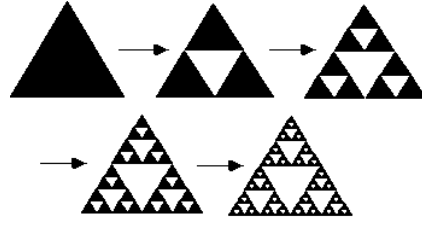


Figure 5.2: A Sierpinski triangle after four iterations [141].

The recursive technique of removing a part of an object is also present in the Cantor set fractal. In order to create a Cantor set, the middle third of the interval is removed. This process is repeated with the remaining two pieces in the second iteration. As described above, subsequent iterations can be created by repeating the removal process. The length of each segment created after the  $n^{\text{th}}$  iteration is given by eqn. (5.3). In Figure 5.3, a Cantor set fractal of five subdivisions is shown. The fractals presented have been modified to suit the application in this thesis and are explained in subsequent subsections.

$$L_n = \left(\frac{1}{3}\right)^n \quad (5.3)$$

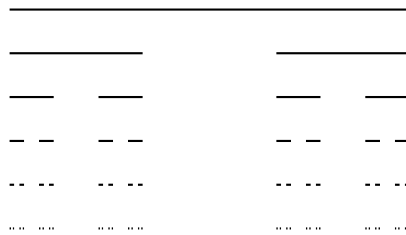


Figure 5.3: A Cantor set after five iterations [142].

### 5.3 Fractal Based Modelling

Two machine workshops (Loughborough University and [139]) were modeled in a commercial ray tracing software (Wireless Insite<sup>®</sup>). The machine workshop shown in Figure 5.4 shows the redrawn machine workshop layout from [139]. The dimensions of the Clemson University workshop are 16 m by 10.5 m and the inventory was similar to the

Loughborough University workshop, however the layouts were distinctly unique. With respect to the material definitions, similar materials were used in both workshop models. The fractal object placement algorithm can be summarized as follows:

1. Define a square cell using the shorter dimension ( $L_{sc1}$ ) of the machine shop. A cell in this work is defined as a square boundary that imposes space constraints for placing the fractal objects.
2. Using the defined square cell, place fractal objects from the first and second fractal iteration/level. These objects can be referred to as “Level 1” and “Level 2” objects.
3. Define a second square cell. This cell is smaller than the cell defined in 1). The length of the second square cell in meters can be expressed as:  $L_{sc2} = L_{sc1} - 1$ .
4. Repeat 2) using the cell size defined in 3).
5. Define the smallest square cell with length  $L_{sc3}$ ;  $L_{sc3} = L_{sc2} - 1$ .
6. Repeat 2) using the cell size defined in 5).

Using the step-by-step method described, a machine floor space of similar dimensions can be populated with fractal objects of two levels from three different cell sizes. The ray tracing implementations of the fractal overlay on the workshop floor plans are shown in Figures 5.5, 5.6 and 5.7. In the fractal overlay algorithm, the fractal objects of the Sierpinski square are modified to fit the cell size. Consequently, the object locations have been approximated in line with the grid size.

A numeric label was attached to each of the level 2 objects for each cell, by numbering left to right and top to bottom. This provides an opportunity to mix the material definition of the level objects. For example, a percentage of the level 2 objects can be defined as PEC or wood. From the Sierpinski square layout, the level 1 objects were selected as 1 m by 1 m. As a result of the Sierpinski square rule, the level 2 objects are dimensioned one-third of the level 1 objects. Based on the height distribution of objects at the workshops, the height of level 1 objects was set to 3 m and level 2 objects were set to 2 m.

With the square cells defined, the fractals were used to populate the respective machine shop floors. For both machine shop models,  $\lambda/2$  dipoles were used and the signal band-

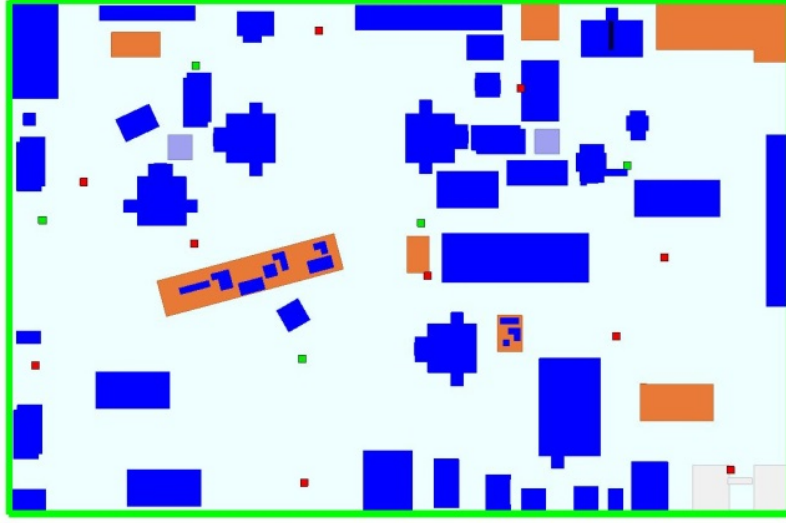
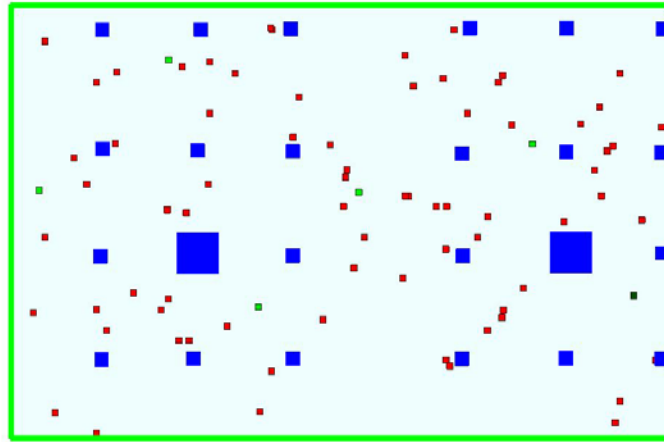


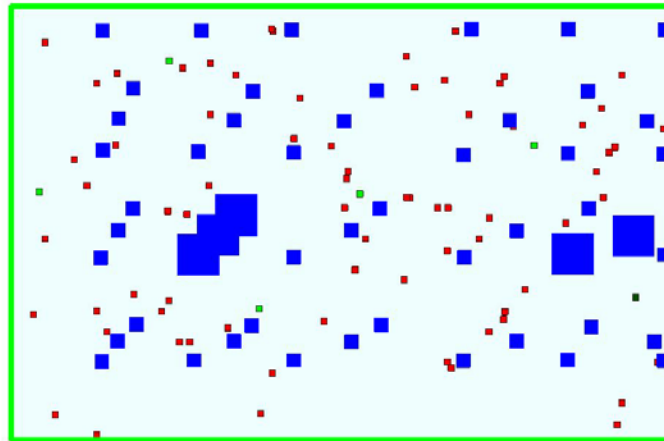
Figure 5.4: Clemson University Machine Workshop adapted from [139]. Blue objects represent PEC and wooden objects are coloured in brown.

width was set at 200 MHz (2.3 GHz - 2.5 GHz) in order to cover the license free spectrum. At millimetre wave (60 GHz), the simulation bandwidth was also set to 200 MHz. In both machine shop models, five pseudo randomly located active transmitters ( $T_x$ ) with fifty receivers ( $R_x$ ) were used for obtaining the overall delay spread distribution on the workshop floor plans. This combination creates 250 different  $T_x \rightarrow R_x$  receiver locations. With respect to average power delay profiles (APDPs), the machine workshop at Loughborough University was used with one active transmitter and ten receiver locations <sup>1</sup>. The transmitter and receiver locations used for the fractal statistical analysis are shown in Figure 5.8. With the selected fractal overlay in place, the topographies of the receiver locations with respect the transmitter created seven NLoS points and three LoS points (R5, R7 and R10). Given that the floor plans of both workshops are of similar dimensions, the fractal overlay of both workshops gives rise to approximately 46 objects. All the transmitters and receivers locations used were placed at a height of 1.5 m.

<sup>1</sup>Due to the large amount of channel profiles obtainable using the virtual array method, one out of the five transmit antennas and ten out of the receiver locations were selected for the PDP analysis

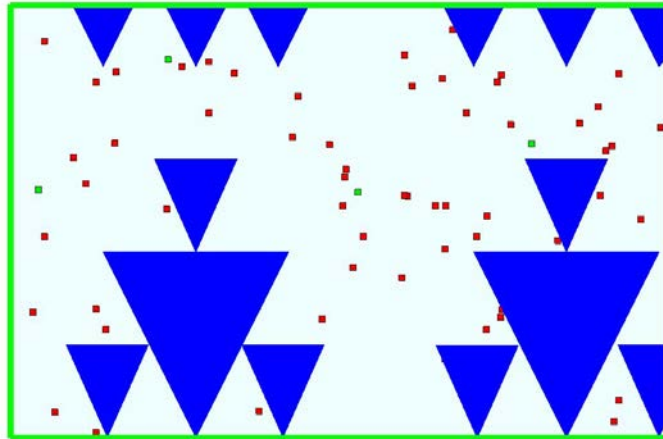


a)

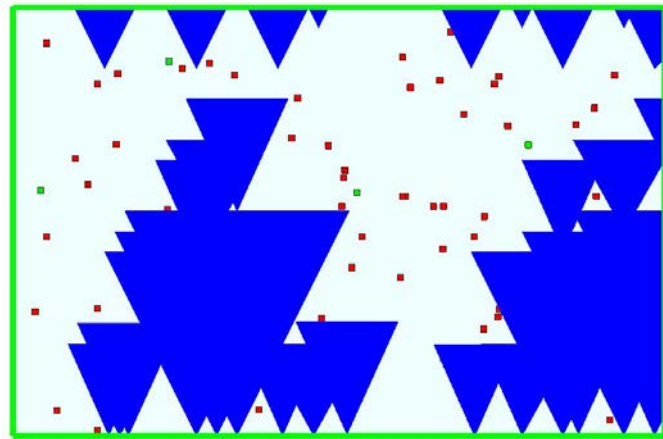


b)

Figure 5.5: a) Clemson University Sierpinski square fractal layout for 9m cell, b) Clemson University Sierpinski square fractal overlay for 9m, 10m and 11m cells. The red dots are receivers and green dots are transmitters.



a)



b)

Figure 5.6: a) Clemson University Sierpinski triangle fractal layout for 9 m cell, b) Clemson University Sierpinski triangle fractal overlay for 9 m, 10 m and 11 m cells.

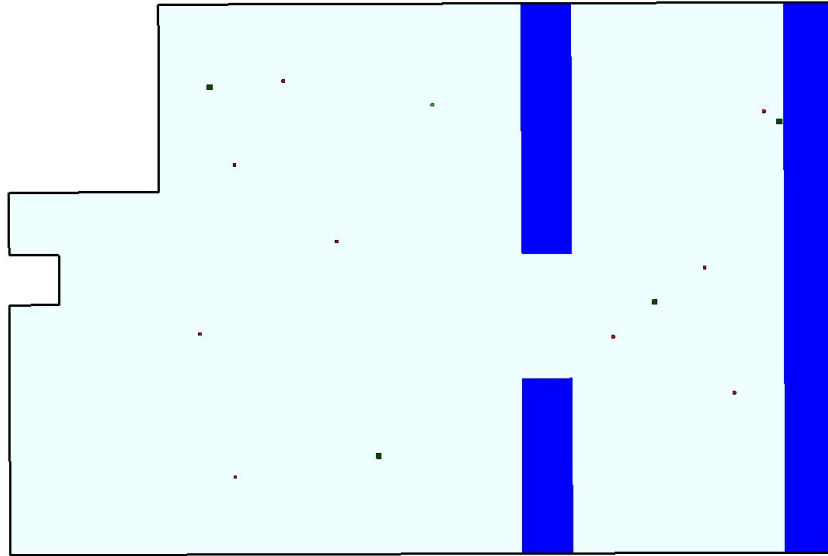


Figure 5.7: Loughborough University Cantor set fractal overlay layout. Due to the pattern of the Cantor set, objects for different cell sizes overlap.

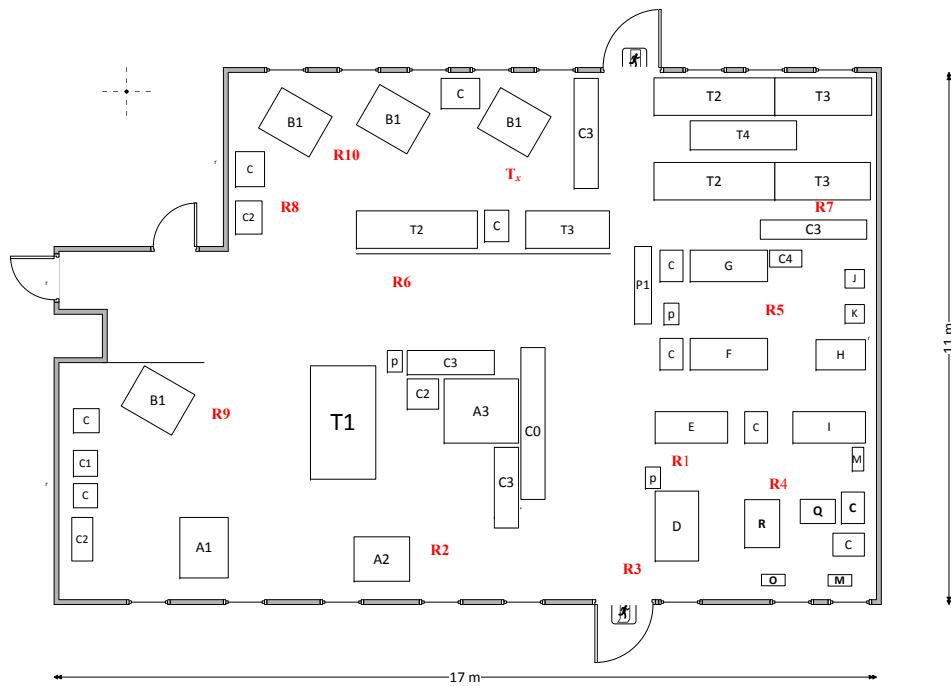


Figure 5.8: Transmitter and receiver locations used for fractal APDP analysis on the Loughborough University workshop floor plan.



## 5.4 Fractal Overlay Statistical Features

As described in Chapter 2, large-scale fading effects within an area (of  $10\lambda - 40\lambda$ ) on the machine workshop floor is relatively constant [143]. Thus, small-scale fading effects can be studied using *virtual arrays* [111]. The virtual array adopted is made up of a uniform linear array (ULA) of 4  $\lambda/2$  dipoles at the transmitter and a uniform rectangular array (URA) of twelve  $\lambda/2$  dipoles at the receiver end. The separation between each element in the corresponding array is  $\lambda/2$ . The virtual array set up (of 48 elements) is depicted in Figure 5.9 and it aligns with the IEEE 802.15.4a requirement presented in [144]. The fractal features data pool contains 960 profiles ( $48 \times 10$ ) for 2.4 GHz and ( $48 \times 10$ ) for 60.0 GHz. The PDP between the  $a^{th}$  element of the ULA and the  $b^{th}$  element of the URA  $P(\tau, a, b)$  shows the power/time distribution between  $a$  and  $b$ . The APDP between  $a$  and  $b$  was obtained by spatially averaging the PDPs such that the first MPC of each profile arrives in the same delay bin for all  $P(\tau, a, b)$ .

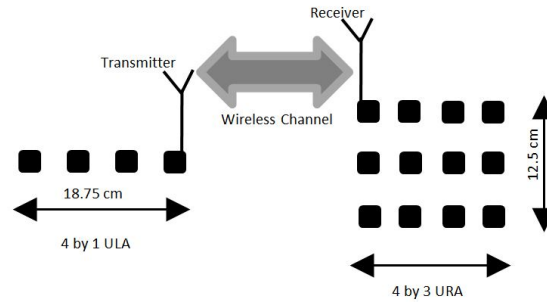


Figure 5.9: Virtual antenna array setup.

### Saleh-Valenzuela Model Parameters

The cluster arrival rate ( $\Lambda$ [1/nsec]), ray arrival rate ( $\kappa$ [1/nsec]), cluster decay factor ( $\Gamma$ ) and ray decay factor ( $\gamma$ ) make up the Saleh-Valenzuela (S-V) model parameters. In this thesis, “visual inspection” has been used to identify clusters. This manual cluster identification technique has been widely adopted in the literature [110, 145, 146], as well as the IEEE 802.11 TGn Channel model [147].

1. *Cluster Arrival Rate*: The inter cluster arrival rate ( $\Lambda$ ) was calculated using the inter cluster arrival time ( $\Delta T_l = T_l - T_{l-1}$ ). The  $\Delta T_l$  was then averaged for the respective APDP, thus  $\Lambda = 1/\overline{\Delta T_l}$ .

2. *Ray Arrival Rate*: The ray arrival rate ( $\kappa$ ) was obtained based on the recommendations in [110, 111, 149] and the delay bin was selected as 5 ns.
3. *Cluster Power Decay*: The cluster decay ( $\Gamma$ ) for LoS or NLoS was obtained by graphing the peak cluster power and arrival time for similar topographies. The cluster power decay was then obtained by performing linear regression with the normalized power in dBm and the delay (ns). The slope of the regression line was then converted to the decay constant using eqn. (5.4).

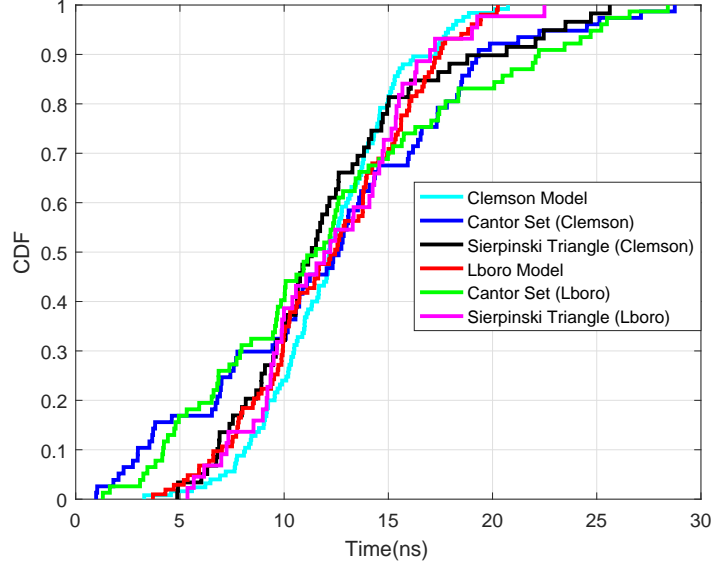
$$\Gamma = \frac{-10}{\ln 10 k_{reg,l}} \quad (5.4)$$

where  $k_{reg,l}$  is the slope of the regression line on dB scale for cluster  $l$ .

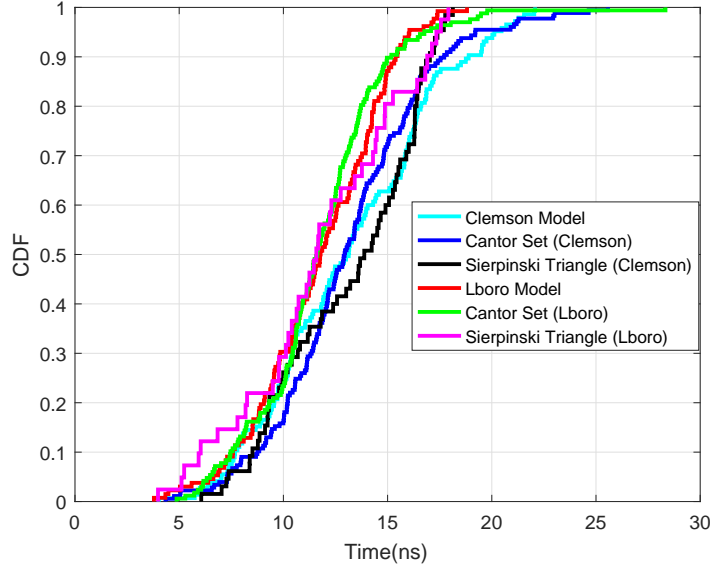
4. *Ray Power Decay*: The ray decay constant ( $\gamma$ ) was calculated in a similar way as the cluster decay constant. For a specified cluster  $l$ , the ray decay was obtained from a linear regression of the logarithmic powers and the delay for MPCs within a cluster  $l$ , with the log power as the dependent variable and delay as the independent variable.

## 5.5 Time Dispersion Prediction Using Fractal Overlays

Using the machine workshop models with their corresponding inventories, the  $\tau_{rms}$  was calculated at 250 receiver locations in Wireless Insite. In the simulation, the propagation paths were used to determine the topographies of the receiver locations (NLoS or LoS). In Figure 5.10, the NLoS and LoS CDFs of the delay spread computed for both machine workshops was compared to the values obtained using the Cantor set and Sierpinski triangle fractal overlays. Due to the characteristics of the Cantor set and Sierpinski triangle fractals (which can be seen in Section 5.2), both fractals have sparse level 2 objects. As a result, they offer little flexibility regarding overlaying objects for the first and second iterations. Moreover, the Cantor set creates LoS topographies for approximately 70 % of the receiver points since it has only two visible objects (as shown in Figure 5.7) and the Sierpinski triangle absorbs 55 - 65% of the receiver points in its fractal objects<sup>2</sup>. As a result, only the Sierpinski square layout will be discussed further in this chapter.



(a)

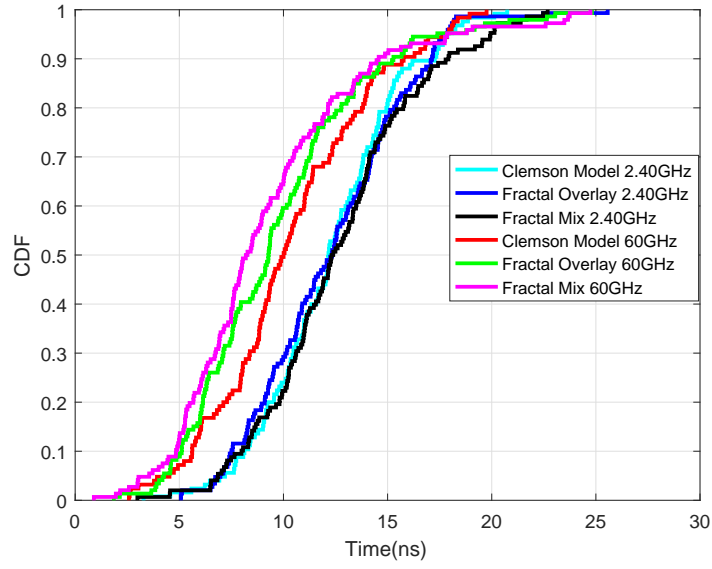


(b)

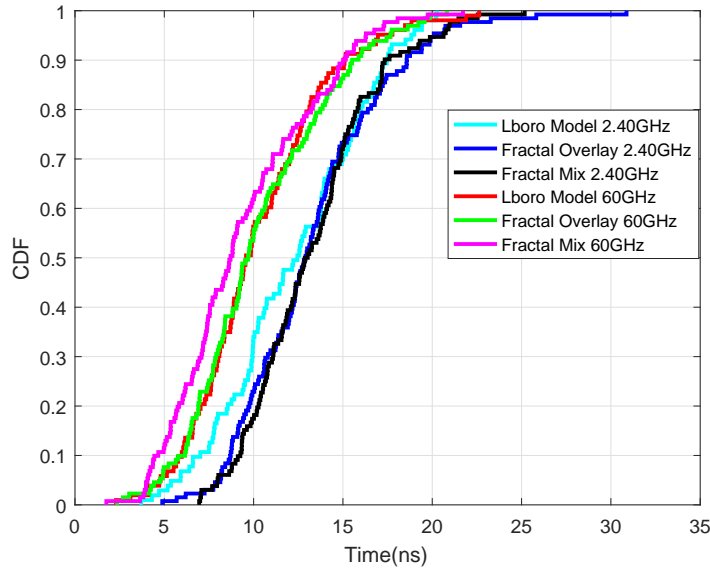
Figure 5.10: Simulation of delay spread CDF at 2.4 GHz using Cantor set and Sierpinski triangle fractal overlays a) NLoS b) LoS. All objects in the simulation were PEC.

In Figures 5.11 and 5.12, the CDF of the simulated delay spread at 2.4 GHz and 60 GHz is presented. Both Figures (5.11 and 5.12) also show the delay spread obtained when the material definition of a percentage of the level 2 objects is changed to *wood*. The primary purpose of mixing the level 2 objects is to observe the effect of the material definitions on the EM wave propagation. As the amount of wooden content increases, the delay spread

<sup>2</sup>The delay spread CDFs presented in this chapter have been normalised



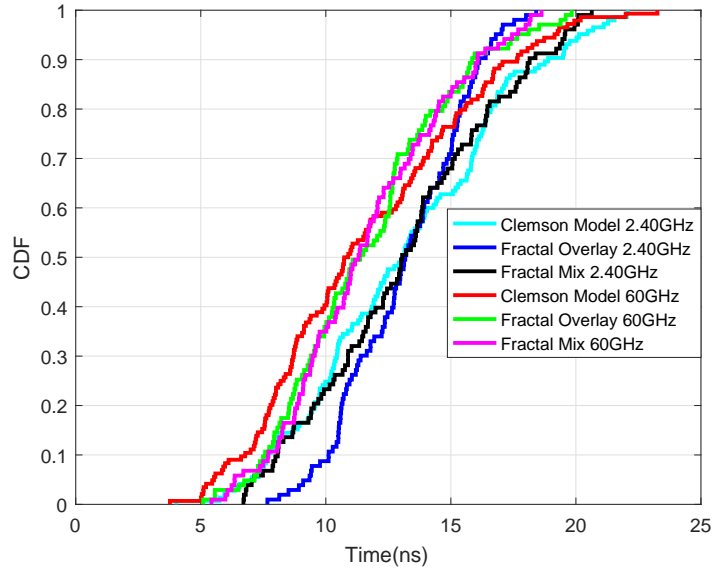
(a)



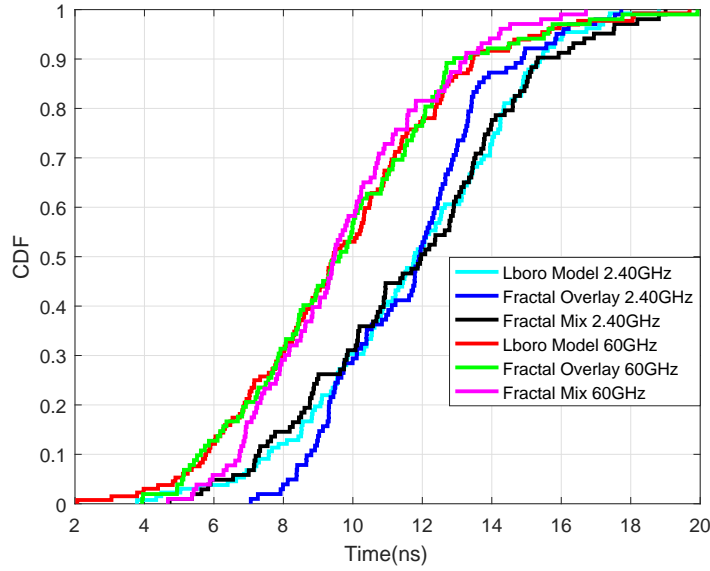
(b)

Figure 5.11: Simulation of NLoS delay spread CDF using Sierpinski square fractal overlay and overlay mixture. a) Clemson University workshop and b) Loughborough University workshop.

for NLoS and LoS reduced. This is the expected behaviour, as the environment becomes more absorbent than reflective. Thus, a non reflecting environment can be created by defining the fractal objects as wood or paper, and a highly reflecting environment can be created by adding metal objects in smaller fractal cells for the overlay algorithm described.



(a)



(b)

Figure 5.12: Simulation of LoS delay spread CDF using Sierpinski square fractal overlay and overlay mixture. a) Clemson University workshop and b) Loughborough University workshop.

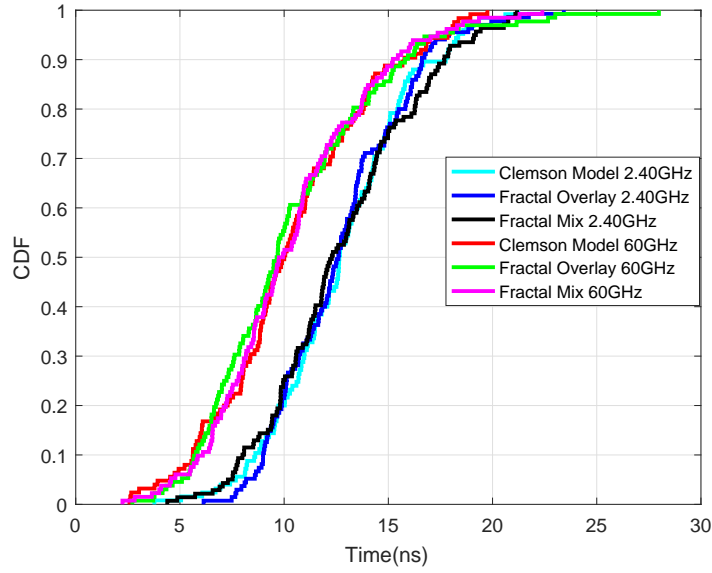
Thirty percent absorbent material mixture was chosen as a compromise between the number of level 2 objects and the reducing effect on the delay spread. Using the Sierpinski square overlay, 90% of the arriving paths were within 15.04 ns (NLoS) and 10 ns (LoS) within both workshop models at 2.4 GHz. While the Sierpinski square overlay mixture had most of its MPCs arriving within 17.78 ns (NLoS) and 15 ns (LoS), which

is closer to the delay spread results from the exact models at 2.4 GHz. At 60 GHz, 90% of the arriving NLoS paths are within 15.52 ns for the Sierpinski square fractal overlay, and 15.01 ns for the fractal overlay mixture. The corresponding LoS values are 12.44 ns and 11.70 ns.

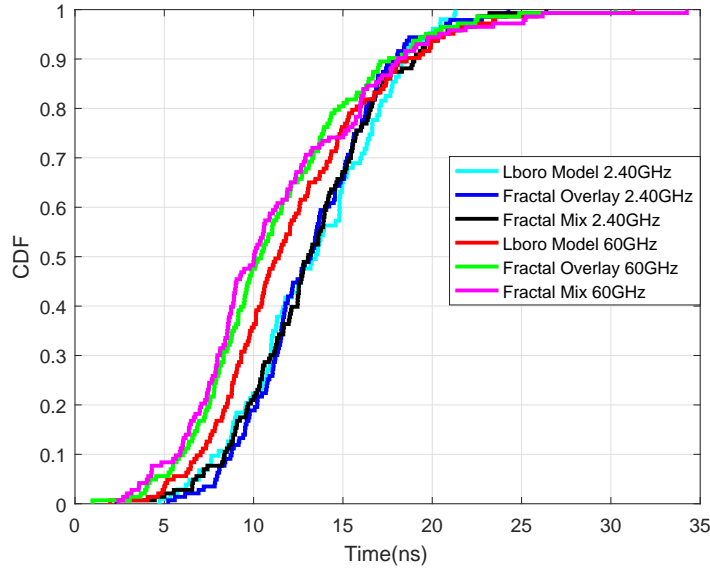
Further exploring the Sierpinski square layout, the number of edges per  $\text{m}^2$  was reduced by using triangular solids. The triangular solids inherit all the design parameters of the Sierpinski square overlay fractal layout, with the edges of each object reduced by two. In Figures 5.13 and 5.14, the CDFs for using the triangular objects fractal layout is shown for the same NLoS and LoS topographies. From the results, it can be observed that when the number of edges are reduced, the mean delay spread prediction error is reduced at both 2.4 GHz and 60 GHz. This shows an inverse relationship between the number of edges per  $\text{m}^2$  and the mean delay spread. Thus, the number of edges per  $\text{m}^2$  and the introduction of wooden objects both have dominant effects on the fractal overlay results. With the triangular objects fractal overlay, 90% of the arriving paths were within 17.98 ns (NLoS) and 15.78 ns (LoS) in both workshop models at 2.4 GHz. The triangular objects fractal overlay mixture had most of its paths arriving within 18.82 ns (NLoS) and 16.60 ns (LoS). At 60 GHz, 90% of the arriving NLoS paths were within 17.38 ns for the triangular objects fractal overlay and the overlay mixture. The corresponding LoS values were 14.39 ns and 12.62 ns.

In Table 5.1, the mean, standard deviation, and maximum values of the delay spread obtained from all the scenarios considered is presented. From Table 5.1, it is evident that the triangular objects fractal overlay reduces the effect of mixing the level 2 objects. As a result, this can be used when the amount of absorbent material is uncertain. With respect to the fractal objects, level 2 objects have a greater effect on the mean and standard deviation of the delay spread when compared to level 1 objects.

Upon investigating the summary of the statistics presented in Table 5.1, it can be observed that the LoS delay spread for the Clemson University workshop model was greater than the NLoS component. This is most likely due to the workshop layout, which can introduce additional reflection and diffraction surfaces. Thus, generating more propagation paths at the scatterers. In the literature, a similar phenomenon has been observed in [103], where the LoS component was higher than its NLoS component. In general,



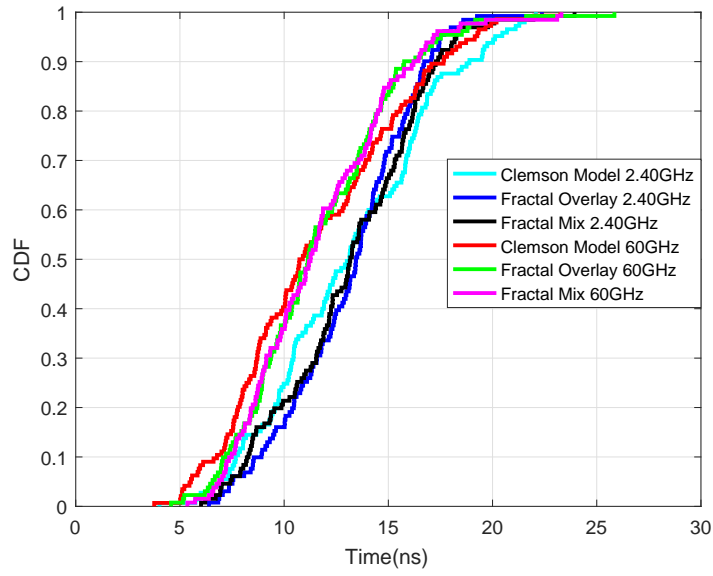
(a)



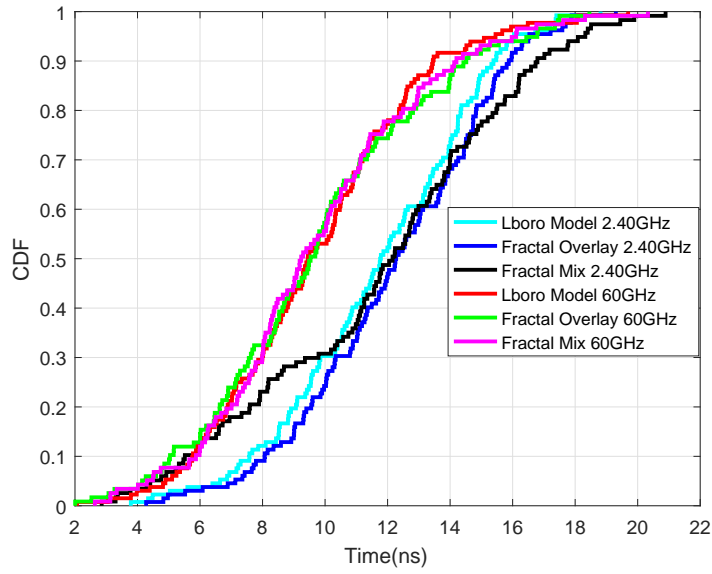
(b)

Figure 5.13: Simulation of NLoS delay spread CDF using Triangular objects fractal overlay and overlay mixture. a) Clemson University workshop and b) Loughborough University workshop.

lower delay spread was observed at 60 GHz which aligns with the literature [94, 148]. The ability of the fractal overlay to preserve the topographies of the receiver locations was investigated, and the results are presented in Table 5.2. Regardless of the topography of the receiver point in the workshop models, the fractal overlay technique has shown its ability to predict the delay spread for NLoS and LoS topographies.



(a)



(b)

Figure 5.14: Simulation of LoS delay spread CDF using Triangular objects fractal overlay and overlay mixture. a) Clemson University workshop and b) Loughborough University workshop.



Table 5.1: Summary of mean RMS delay spread, standard deviation and maximum at 2.4 GHz and 60 GHz for the fractal overlay combinations used at Clemson University model and Loughborough University workshops. Triangular objects in the Sierpinski square layout are represented as TO

Workshop/Topography	Fractal/Model	2.4 GHz			60 GHz		
		$\mu$ (ns)	Std.	Max (ns)	$\mu$ (ns)	Std.	Max (ns)
Clemson/NLoS	Model	12.27	3.28	20.74	10.34	3.82	19.75
	Sierpinski Square (SS)	9.18	3.59	22.48	9.72	4.21	24.81
	Triangular objects (TO)	11.97	3.15	22.64	9.93	4.22	27.58
	Mixed (SS)	12.69	3.82	22.69	9.22	4.51	24.74
	Mixed (TO)	12.75	3.62	21.18	9.13	3.77	21.19
	Cantor set	12.26	6.39	28.73			
	Sierpinski Triangle	8.43	4.88	21.79			
Clemson/LoS	Model	13.16	4.10	22.08	11.61	4.20	23.26
	Sierpinski Square (SS)	6.83	2.44	12.08	8.20	3.35	16.43
	Triangular objects (TO)	10.12	3.08	19.33	9.15	3.60	23.39
	Mixed (SS)	9.94	3.72	17.42	7.23	3.21	14.25
	Mixed (TO)	9.63	3.51	20.40	7.87	3.47	19.56
	Cantor set	10.42	3.72	22.84			
	Sierpinski Triangle	10.33	3.35	15.30			
Lboro/NLoS	Model	12.28	4.00	20.25	10.24	3.83	22.62
	Sierpinski Square (SS)	9.75	4.08	27.35	10.27	3.90	20.82
	Triangular objects (TO)	13.31	3.69	24.26	11.23	4.78	30.26
	Mixed (SS)	13.28	3.54	25.17	9.41	3.96	21.73
	Mixed (TO)	13.14	4.17	26.21	10.52	5.37	33.54
	Cantor set	11.75	6.64	27.87			
	Sierpinski Triangle	6.97	3.94	17.17			
Lboro/LoS	Model	11.71	3.06	18.18	9.70	3.21	19.70
	Sierpinski Square (SS)	6.35	2.35	12.37	7.69	3.11	17.92
	Triangular objects (TO)	11.22	3.81	19.10	9.57	3.57	18.33
	Mixed (SS)	9.98	3.23	17.27	6.12	2.55	13.13
	Mixed (TO)	11.52	4.18	20.69	8.19	3.41	18.82
	Cantor set	10.41	3.20	27.04			
	Sierpinski Triangle	9.48	3.77	15.69			

Table 5.2: Summary of receiver point classification using Loughborough and Clemson University models

Site	Sierpinski Square (%)	Triangular solids(%)	Cantor Set(%)	Sierpinski Triangle(%)
Lboro	47.3	50.6	48.5	23.3
Clemson	50.0	55.6	62.2	27.6

## 5.6 Validation of Fractal Overlay Model

The fractal model (triangular objects fractal overlay) was validated using the S-V model parameters at 2.4 GHz. In Table 5.3, a summary of the model parameters which are obtained from the visually identified clusters is presented. In the Loughborough University workshop model, the ray decay ( $\gamma$ ) was between 0.72 and 20 for NLoS and LoS sites. It also generally increased with the cluster arrival time which aligns with the result in [110]. In total, 38 clusters were investigated with average cluster number of 3 for LoS and 4 for NLoS at 2.4 GHz and 4 for LoS/NLoS at 60 GHz. The statistical simulation of the delay spread was obtained by applying a 200 MHz filter to the UWB S-V model implementation in [149]. A comparison of the delay spread prediction using the bandwidth limited S-V model and the fractal overlay is presented in Table 5.4<sup>3</sup>. With respect to the manual cluster identification technique, it should be noted that clusters generally overlap. However the rays within a cluster decay much faster than the power of the first ray in the following cluster [39]. Thus, the clusters have been identified assuming the inter cluster time is sufficiently large, such that the clusters can be identified with the naked eye [39]. Upon inspecting the APDPs generated from the fractal overlay model, the following features (which are in agreement with [110]) were observed:

1. Clusters have different decay constants, and the ray decay constant within a cluster increases with delay.
2. Some of the clusters show more than one decay.

<sup>3</sup>Based on the recommendations in [110, 111, 149], the the delay bin was selected as 5 ns. Consequently, the rays arrive at regular intervals of 5 ns

3. For all the LoS receiver locations, the first MPC is the strongest and arrives first. After which attenuated MPCs follow. This also occurs with some of the NLoS locations.

In Appendix F, the APDPs used to obtain the S-V parameters at 2.4 GHz and 60 GHz are presented.

Table 5.3: S-V Channel parameters from Loughborough University machine workshop at 2.4 and 60 GHz

S-V parameter	LoS 2.4 GHz	NLoS 2.4 GHz	LoS 60 GHz	NLoS 60 GHz
$\Gamma$	10.90	12.83	12.08	11.39
$\gamma$	7.70	9.70	6.70	6.90
$\Lambda$	0.04	0.06	0.04	0.045
$\kappa$	0.20	0.20	0.20	0.20

Table 5.4: Fractal overlay (Triangular solids) and S-V model delay spread comparison for Loughborough University machine workshop

Scenario	Fractal overlay (ns)	S-V model (ns)
LoS (2.4 GHz)	11.22	11.00
NLoS (2.4 GHz)	13.31	14.00

## 5.7 Summary

This chapter has presented in-depth details of a novel technique that can be used to rapidly model delay spread in workshop environments. The fractal overlay formed from three “cells” has been used to populate the machine workshop plan using the fractal algorithm presented. The delay spread obtained from the Saleh-Valenzuela model showed a maximum of 5% MAPE. The results presented in this chapter show that this technique can be used to model performance of a communication technology in an indoor location without information of the inventory. In Chapter 6, spatial interpolation techniques are used to predict the received power at unsampled points. These unsampled points represent areas where measurement results have not been taken but are suitable locations for sensor nodes or energy harvesting devices.

## **Chapter 6**

# **Predicting Received Power and Energy Profiles Using 2-D Interpolation**

While the sparse spot RF power density measurements presented in Chapter 3 of this thesis are insufficient to provide a detailed overview of the ambient power distribution at the DEP, it is also practically impossible to take measurements at every feasible location where an energy harvesting device can be placed. This chapter discusses how spatial interpolation techniques can be used as a compromise between both extremes. In Section 6.2, the interpolation techniques used are discussed. Section 6.3 investigates how the interpolation techniques perform using measurement data from Chapters 3 and 4. An overlaying grid of the interpolated values is generated and used in Section 6.4, where the energy available to an energy harvesting devices is integrated across a specified path over time.

## 6.1 Introduction

In reality, it is practically impossible to obtain measurement results for a large number of  $x, y$  coordinates at a plant due to constraints such as accessibility to mains power and risk assessment requirements. These constraints also apply to smaller floor spaces like machine workshops, as these locations usually have restrictions with respect to working hours and health & safety. With the aid of a power density grid for both sites, it is possible to extend the measured results to other feasible coordinates where energy harvesting devices might be placed. Moreover, it is possible that these devices are placed in hard to reach areas which might not be suitable for measurements. In general, interpolation techniques are premised on the fact that events occurring within a predefined cluster are closely correlated. In geographic information systems (GIS), spatial interpolation has been used for: contouring display data, mathematically determining surface properties at specified points and spatial decision making [122, 150–153]. Moreover, other 2-D interpolation techniques such as bilinear interpolation, cubic convolution and nearest neighbour have been used in the literature for image processing [154–161].

With respect to the interpolation techniques adopted, two different approaches were used to determine the most suitable interpolation technique for both locations. For the Loughborough University workshop model, fifty percent of the points from the interpolated grid were compared to the exact values from the deterministic model. In the ray tracing software, a XY grid of receiver points was created. The number of receiver points in the XY grid of the ray tracing model was 160 at 1 m spacing. In the DEP model, the locations at which measurements were taken were predicted using the interpolation techniques. Consequently creating a scenario where four measurement points were used to predict the value at the fifth point. In this chapter, the three interpolation techniques adopted for estimating power levels at the DEP and Loughborough University machine workshop will be discussed and compared using the MAPE.

## 6.2 2-D Grid Interpolation Techniques

Spatial interpolation techniques (or methods) can be viewed as a weighted combination of observed data [123]. This weighted sum can be generalized using the prediction formula shown in eqn. (6.1), where  $z(x_o, y_o)$  is the predicted value of a primary variable at an unsampled point,  $z(x_i, y_i)$  are the observed values of the primary variable,  $\lambda_i$  is the weight allocated to the respective observations and  $n$  represents the number of sample points used in the interpolation method [162].

$$z(x_o, y_o) = \sum_{i=1}^n \lambda_i z(x_i, y_i) \quad (6.1)$$

Scattered data interpolation methods can be grouped into three categories, namely: Non-geostatistical interpolation methods, geostatistical interpolation methods and combined methods. Non-geostatistical interpolation methods include nearest neighbour, inverse distance weighting, radial basis functions and natural neighbours, while kriging and its variants are geostatistical methods [123, 163, 164]. The difference between geostatistical and non-geostatistical interpolation techniques is that geostatistical methods estimates the variability of the predicted values at the unsampled location. Combined interpolation methods such as gradient plus inverse distance squared and clustering assisted regression method combine non-geostatistical and geostatistical methods. Irrespective of the interpolation method classification, spatial interpolation techniques can be characterized by the following features [165]:

### Global versus Local

Spatial interpolation techniques that use all the sampled data points in predicting the weighted average are regarded as global methods. On the other hand, local methods use a subset of the sampled points. The sampled points used in the prediction are determined by a constraint set a priori.

### Exactness

This measures the accuracy of the interpolation technique. A spatial interpolation technique that predicts the same value of a primary variable at a sampled point is referred to as an exact method, otherwise it is referred to as inexact.

### Deterministic or stochastic

Deterministic interpolation methods only provide estimations of the primary variable at an unsampled point, while stochastic methods compute the estimated values as well as uncertainties associated with the prediction.

### Univariate versus multivariate

Interpolation techniques that use only the primary variable (such as power density or received power) to predict values at unsampled points are referred to as univariate. Multivariate interpolation methods use a primary and at least one dependent variable in predicting unsampled data.

### Convex versus non-convex

Interpolation techniques that predict values that are bounded by the maximum and minimum observations are referred to as convex interpolation methods. While predictions from non-convex methods could yield values outside the range of the observed data.

The features of the interpolation techniques used to predict the RF power (and RF power density) at locations other than the measurement or observation points are summarized in Table 6.1.

Table 6.1: Features of interpolation techniques adopted [164]

Interpolation method	Global/local	Exactness	Deterministic/Stochastic	Convex/non-convex
IDW	Global	Inexact	Deterministic	Convex
Kriging	Local	Exact	Stochastic	can be non-convex
RBF (Gaussian)	Global	Exact/inexact	Deterministic	can be non-convex

## 6.2.1 Inverse Distance Weighting

Inverse distance weighting (IDW) is a global interpolation technique that uses all the sampled data points to estimate the value at an unsampled point [123, 163]. This technique is based on the assumption that points further away from the unsampled point have less influence. This is evident through its weighted average which assigns smaller weights to points further away from the unsampled point. For a given  $(x, y)$  coordinate, the interpolated value of the received power or power density ( $P_d$ ) can be computed using Shepard's algorithm [166] in eqns. (6.2) to (6.4), where  $h_i$  is the Euclidean distance be-

tween the measurement points and the interpolated location,  $p$  is referred to as the power parameter,  $w_i$  is the interpolation weight. When the power parameter is set to 2, the IDW method becomes analogous to the inverse square law. The interpolated power density in eqn. (6.4) is thus obtained as a weighted average of the sampled power density at the scattered locations  $(x_i, y_i)$ . In Section 6.3, eqns. (6.2) to (6.4) are used to estimate the received power and received power density. Since the interpolated values are based on a weighted average, the interpolated values are bounded by the maximum and minimum values of the sampled data points.

$$w_i = \frac{h_i^{-p}}{\sum_{j=0}^n h_j^{-p}} \quad (6.2)$$

$$h_i = \sqrt{(x - x_i)^2 + (y - y_i)^2} \quad (6.3)$$

$$P_d(x, y) = \sum_{j=0}^n w_j P_d(x_j, y_j) \quad (6.4)$$

## 6.2.2 Radial Basis Function

Radial basis functions (RBF) are another form of deterministic and global spatial interpolation method that have been adopted in fields such as artificial neural networks. In RBF, data is approximated by a sum of translated RBFs of the form of eqn. (6.5), where  $\varphi_r$  is the radial basis function. The expansion coefficients ( $w_i$ ) are selected based on the interpolation condition of the observed data points. In most applications, the Euclidean distance is adopted for the norm. The RBF can be implemented using Gaussian, inverse quadratic and thin plate spline functions [167–169]. The Gaussian RBF is described using eqn. (6.6), where  $\zeta$  is a choice parameter. These equations are used in Section 6.3 to estimate the received power and received power density.

$$y(x) = \sum_{i=0}^n w_i \varphi(||x - x_k||) \quad (6.5)$$

$$\varphi_r = e^{-(\zeta r)^2} \quad (6.6)$$



### 6.2.3 Kriging

Geostatistical interpolation using kriging can be summarized into a two staged process:

1. Creating a variogram and covariance functions to estimate the spatial correlation between the sampled points
2. Predicting the primary variable at the unsampled points

A variogram is a plot of the semivariance which provides a description of the data set's spatial continuity. The semivariance  $\gamma(h)$  can be mathematically defined as shown in eqn. (6.7), where  $h$  is the distance between point  $x_i$  and  $x_o$ . This point-to-point pairing of the sampled data is depicted in Figure 6.1, where the red point is paired with the remaining points and the semivariance is estimated. This process is repeated for each of the sampled points. In other words, pairs with larger separation distance will have a high semivariance, which infers less correlation between the data points. Thereafter, the points are fitted with a known semivariogram model such as the Gaussian variogram. After completing this spatial correlation process, interpolation is then computed using an estimator of choice [163, 164].

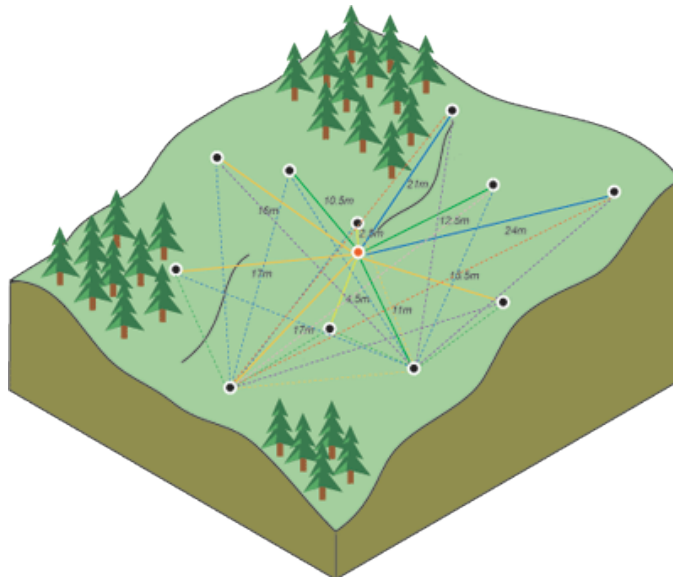


Figure 6.1: Illustration of semivariance pairing using coloured points [170].

$$\gamma(x_i, x_o) = \gamma(h) = \frac{1}{2n} \sum_{i=0}^n (z(x_i) - z(x_i + h)) \quad (6.7)$$

### Kriging Estimator

The generic kriging estimator is shown in eqn. (6.8), whereby the weights are selected such that variance between the prediction and actual value is minimized [163, 164].

$$\hat{z}(x_o) - \mu = \sum_{i=0}^n \lambda_i [z(x_i) + \mu(x_o)] \quad (6.8)$$

In eqn. 6.8,  $\hat{z}(x_o)$  is the estimated value at unsampled point  $x_o$ ,  $z(x_i)$  are sampled values of the primary variable,  $\mu$  is a known stationary mean that is assumed to be constant and  $\lambda_i$  are the kriging weights. The kriging estimator has variants which are modified versions of eqn. (6.8), some of which include: simple kriging, ordinary kriging, kriging with a trend and block kriging. In this regard, ordinary kriging was adopted as it is mostly used and does not require a data mean a priori. In ordinary kriging, the sum of the weights is equal to 1 and  $\mu$  in eqn. (6.8) is replaced by the local mean  $\mu(x_o)$ . The weights  $\lambda_i$  are computed from the semivariance. Thus, they are the solution to a system of linear equations that reduce the mean square error between the estimates and the measured values [171]. In comparison with IDW and RBF, kriging factors in a covariance process that accounts for the statistical relationship amidst the sampled points [172]. The estimated power density was computed in a similar manner, with the weighting function interdependent on the separation distance and the spatial orientation of the measured quantity [173]. Using eqn. (6.9), the power density can be geostatistically estimated.

$$P_d(x, y) = \sum_{j=0}^n \lambda_j P_d(x_j, y_j) \quad (6.9)$$

## **6.3 Evaluating Interpolation Techniques in Multipath Rich Environments**

In order to compare the prediction ability of the interpolation techniques used in this section, the MAPE has been adopted. The interpolation algorithms were implemented in MATLAB, with Kriging and RBF evaluated using [174, 175].

### **6.3.1 Evaluating Interpolation Techniques at Dagenham Engine Plant**

With respect to the DEP, the MAPE was calculated at the five measurement locations. This was carried out by interpolating the measured power density at the respective locations. In Figures 6.2 to 6.6, the interpolated power density is presented for each location at the DEP. The MAPE at the DEP is summarized in Table 6.2, which shows that the interpolation methods generally perform better in the mobile transmit channel than the base station downlink. This is also evident in the low MAPE for Wi-Fi, which has its APs and user equipment located within the DEP. From the results presented in [30], increasing the  $p$  parameter increases the prediction error of the IDW method and the choice of the  $p$  parameter aligns with [171] and the inverse square law. In addition, Kriging Gaussian [176] and RBF showed non-convex behaviour at Locations 1, 2, 3 and 5.

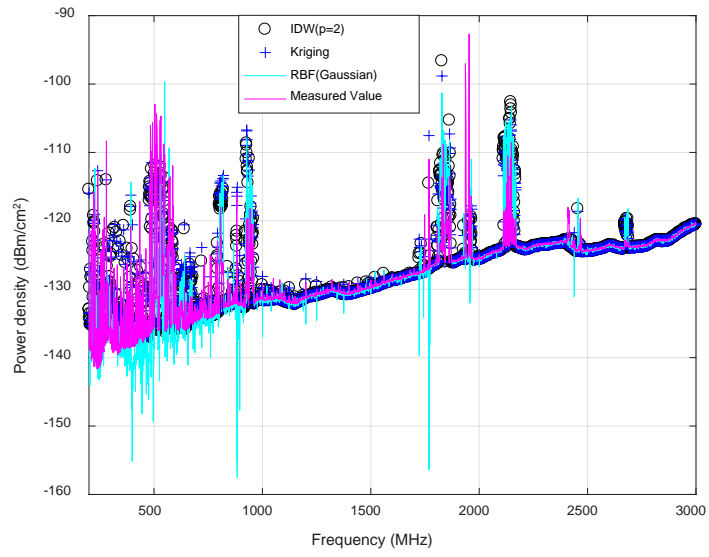


Figure 6.2: Comparison of IDW, Kriging, RBF with the measured value at DEP (Location 1).

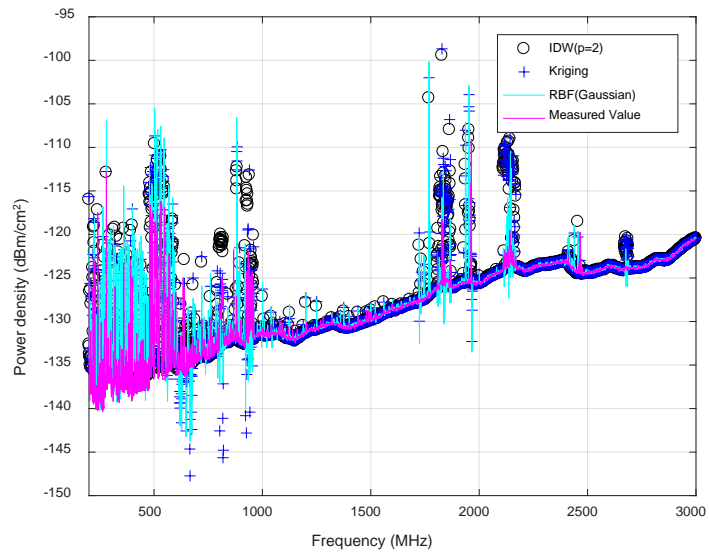


Figure 6.3: Comparison of IDW, Kriging, RBF with the measured value at DEP (Location 2).

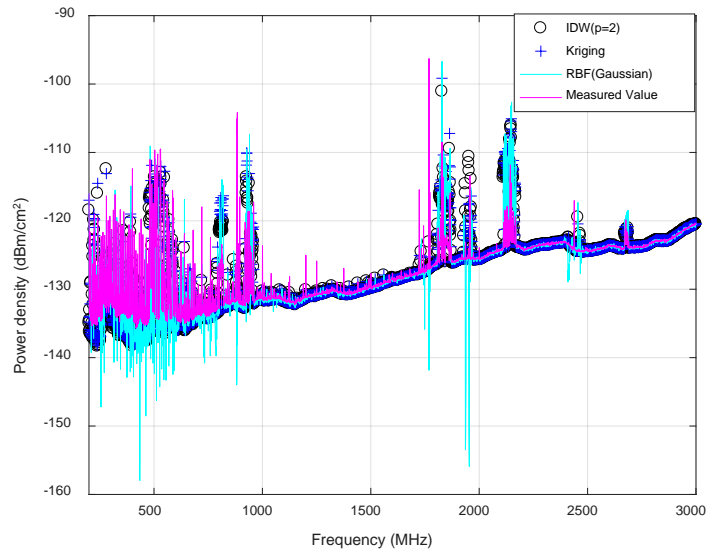


Figure 6.4: Comparison of IDW, Kriging, RBF with the measured value at DEP (Location 3).

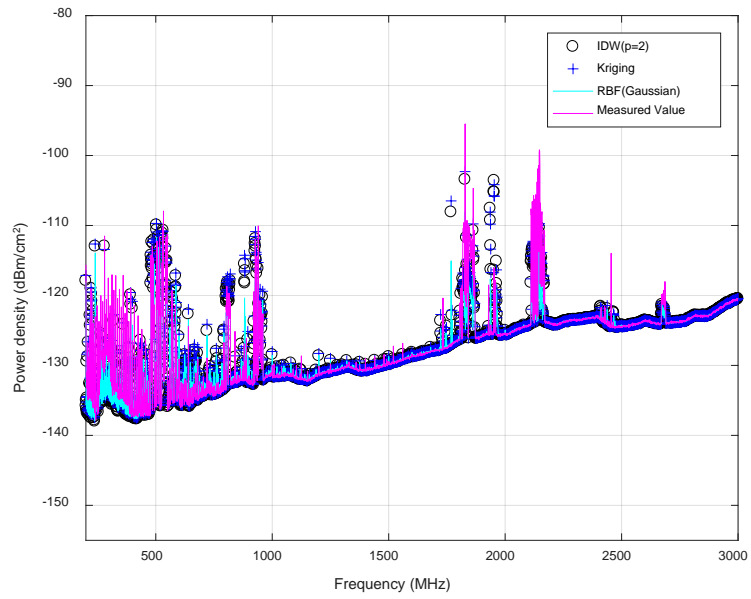


Figure 6.5: Comparison of IDW, Kriging, RBF with the measured value at DEP (Location 4).

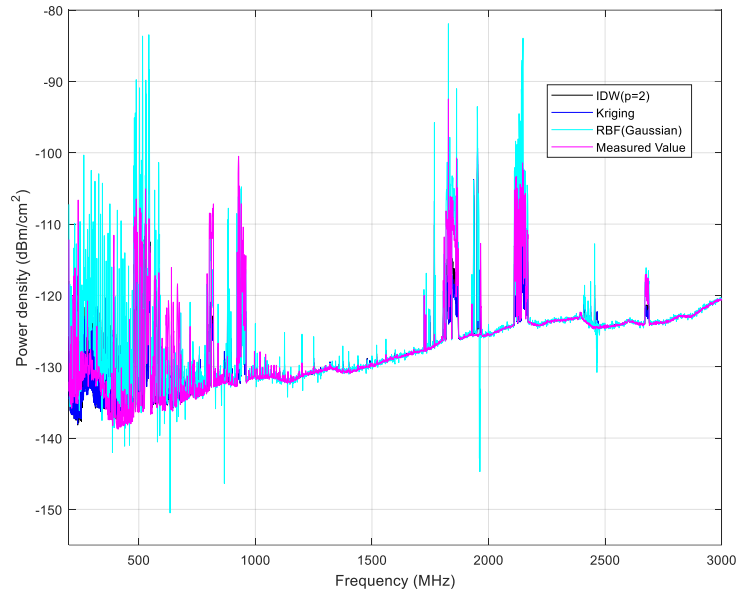


Figure 6.6: Comparison of IDW, Kriging, RBF with the measured value at DEP (Location 5).

Table 6.2: MAPE comparison of interpolated values for RATs at the DEP

RATs	Frequency (MHz)	IDW (p = 2)	Kriging Gaussian	RBF Gaussian
Digital TV	470-610	142	151	100
GSM-900 (MTx)	880-915	20	25	151
GSM-900 (BTx)	925-960	57	69	41
GSM-1800 (MTx)	1710-1785	12	14	10
GSM-1800 (BTx)	1805-1880	49	46	53
3G (MTx)	1920-1980	50	45	28
3G (BTx)	2110-2170	69	67	73
Wi-Fi	2400-2500	11	11	10

### 6.3.2 Evaluating Interpolation Techniques at Loughborough University workshop

In order to extend the usability and adaptability of the interpolation techniques used at the DEP, their ability to predict received power at the Loughborough University workshop was investigated. In this subsection, interpolation prediction was carried out at center frequency of 2.4 GHz. The technique adopted to evaluate the performance of the interpolation methods at the Loughborough University workshop involved predicting the

received power at randomly selected receiver locations. Using the ten receiver locations in Figure 5.4 as control points, the MAPE was calculated for 12% , 23%, 35% and 50% of the receiver points obtained from the XY receiver grid in the deterministic model. The downward trend of the MAPE shown in Table 6.3 is intuitive. This is because the average prediction error reduces with sample size. The percentage threshold of 80 receiver points was selected as a compromise between the number of receiver locations on the XY grid, and the error between the subsequent iterations of the MAPE.

Table 6.3: MAPE performance comparison of the spatial interpolation methods used in predicting XY grid receiver power in the LU workshop model (2.4 GHz)

No. of points	IDW (p = 2)	Kriging Gaussian	RBF Gaussian
19	78	93	73
37	68	81	68
56	71	79	79
80	66	78	71

## 6.4 Estimating Ambient Energy Profiles Using Interpolated Grids

Using any of the interpolation techniques described, a power density grid map can be created that estimates the RF power density at several locations within the DEP or the workshop. In this regard, two case scenarios have been studied and are discussed. The description in Scenario 1 is applicable to the DEP and Scenario 2 applies to the workshop floor plan.

### Scenario 1

A pallet travelling through an arbitrary production line at the DEP. It is essential to note that the paths traced do not show the exact production lines at the plant, however, these paths are conceptualized in order to obtain power budget estimates for wireless sensor nodes to be deployed on pallets at the plant.

## Scenario 2

A wearable sensor device attached to a workshop technician who walks a predefined path along the workshop aisles to a machine equipment.

In both use case scenarios, the path length and travel time determine the ambient RF energy that can be accumulated. It is noteworthy that additional losses will arise from the RFEH conversion and power management circuitry. In order to obtain a theoretical estimate of how much power can be possibly harvested over the entire period, the following assumptions and specifications have been adopted:

1. Pallet speed = 0.1m/s. The pallet speed was obtained by observing pallets at the DEP during the measurement campaign.
2. Time require to travel between each grid point = 10 seconds.
3. Distance between grid points = 1 m. The grid spacing has been chosen as a compromise between computation time of the deterministic model and indexing with respect to estimating the interpolated grid.
4. Total grid points in  $x$ -direction (DEP) = 305. This represents the length of the DEP grid in  $x$  direction. An appropriate scale has been adopted to obtain the interpolated grid.
5. Total grid points in  $y$ -direction (DEP) = 527. This represents the length of the DEP grid in  $y$  direction.
6. Total grid points in  $x$ -direction (LU Workshop) = 16. This represents the length of the LU workshop grid in  $x$  direction.
7. Total grid points in  $y$ -direction (LU Workshop) = 10. This represents the length of the LU workshop grid in  $y$  direction.
8. Walking speed = 1.4 m/s.
9. A realistic RF-DC conversion efficiency of 40%.
10. Negligible battery charging and power management circuit loss.



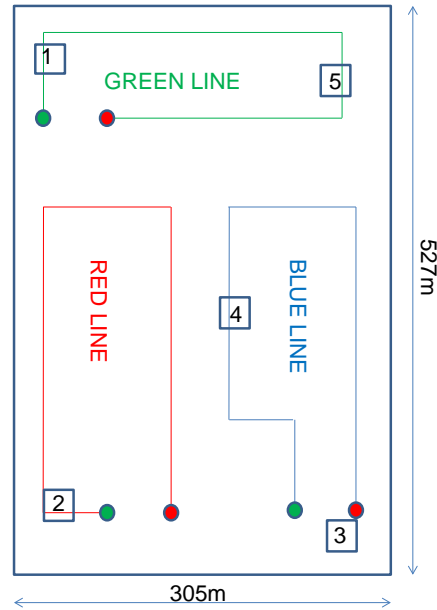


Figure 6.7: Depiction of conceptual paths on a DEP rectangular floor plan.

#### 6.4.1 Predicting Energy Profiles at Dagenham Engine Plant

At the DEP, the power density grid was created for each frequency point in the surveyed frequency spectrum (200 - 3000 GHz). Three paths are shown with respect to a rectangular floor plan of the DEP shown in Figure 6.7. For an RFEH operating at 2.4 GHz, the power profile can be obtained by first converting the received power density to received power using an effective antenna aperture of 100 cm<sup>2</sup>. In Table 6.4, the summary of the energy profiles for the paths travelled is shown.

Table 6.4: Summary of energy profile a pallet travelling a conceptual path at the DEP at 2.4 GHz

Line	Path distance (m)	Travel time (mins)	Energy accumulated (pJ)
Green	522	87.0	73.4
Red	622	103.6	90.0
Blue	642	107.0	95.4

## 6.4.2 Predicting Energy Profiles at Loughborough University workshop

The interpolation grid for the University workshop was obtained from the ten sampled points discussed in Chapter 4 for 2.4 GHz. In Tables 6.5 to 6.7 each grid point (representing 1 m) on the floor plan is shown. The overall distribution of the received power from the XY grid is shown in Figure 6.8. The received power at each receiver point in the XY grid is a combination of the transmit power (0 dBm) from the five transmitters discussed in Section 5.3. Applying use case Scenario 2, a conceptual path of a wearable device is depicted in Figure 6.9 with respect to the floor plan. At 2.4 GHz, the energy accumulated by the wearable device can be estimated as an integral sum of the grid power points over the device travel time. Assuming an average walking speed of 1.4 m/s, it will take 10 seconds to cover the path shown in Figure 6.9 with dash red lines. When comparing the exact inventory and the interpolated power grid, the effect of the MAPE becomes negligible, as the sum of powers along the path are of the same order. Using the same path, the sum of powers from the ray tracing model is 2.4 mW and 1.5 mW from the interpolated received power grid. This difference results to approximately 0.5 dBm. Based on the requirement of a COTS PMM like the BQ25504, a minimum of  $0.1\mu\text{W}$  is required at cold start. With the assumed RF-DC conversion efficiency, the ambient power from the workshop model is able to provide the required start up power for the PMM. Unlike the received power values from the DEP grid, the power distribution in the workshop model is sufficient for RF energy harvesting. Additionally, the Loughborough University workshop has a smaller floor plan area. While this estimate represents a best case scenario, additional signal attenuation can be experienced due to human presence.

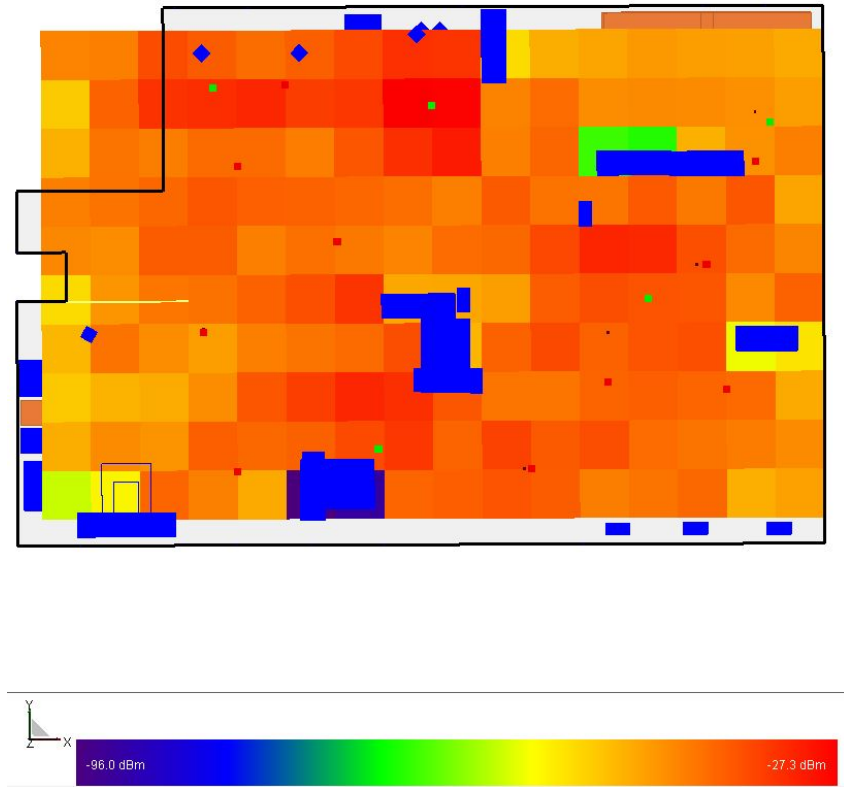


Figure 6.8: Received power distribution for Loughborough University workshop (XY grid). The blue shapes indicate the top view of the machines in the deterministic model

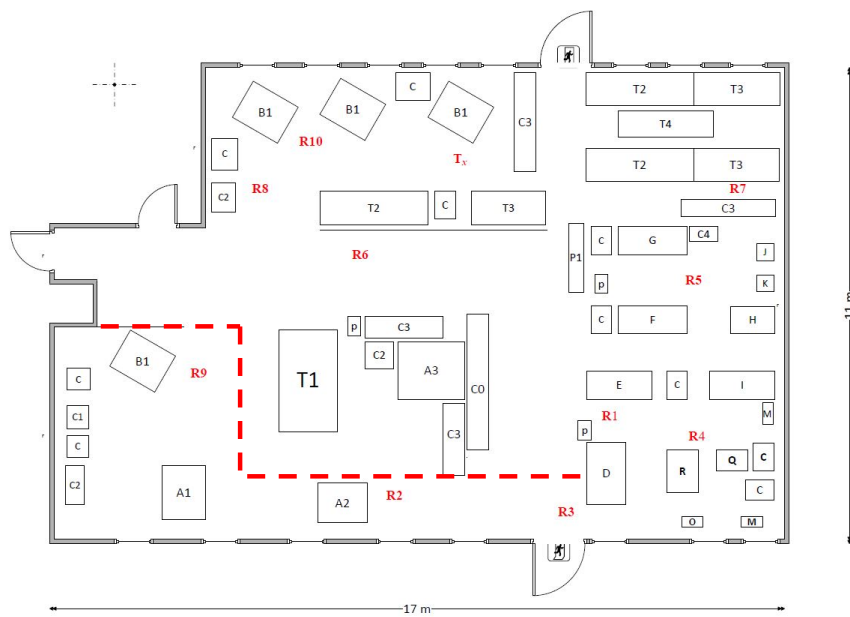


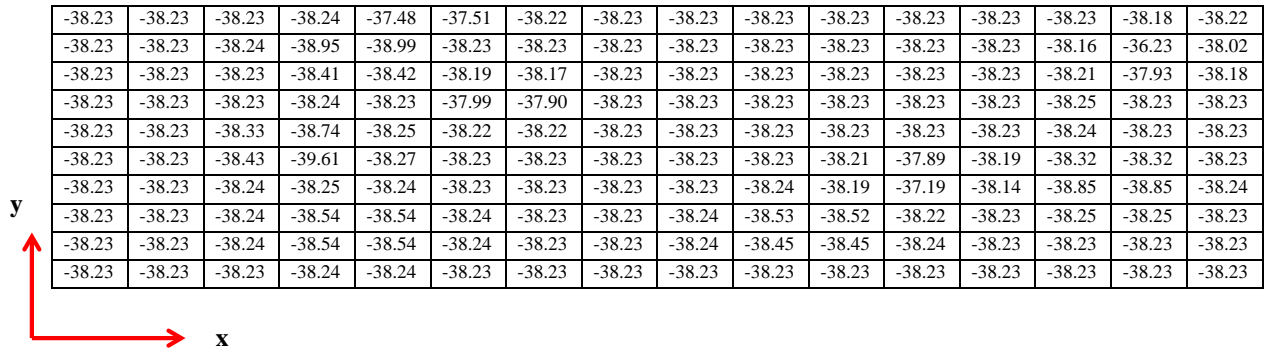
Figure 6.9: Scenario 2 use case energy path profile.

Table 6.5: XY received power grid for Loughborough University workshop using IDW ( $p = 2$ ). The grid shows 16 by 10 grid points which represent the receiver locations in the deterministic model



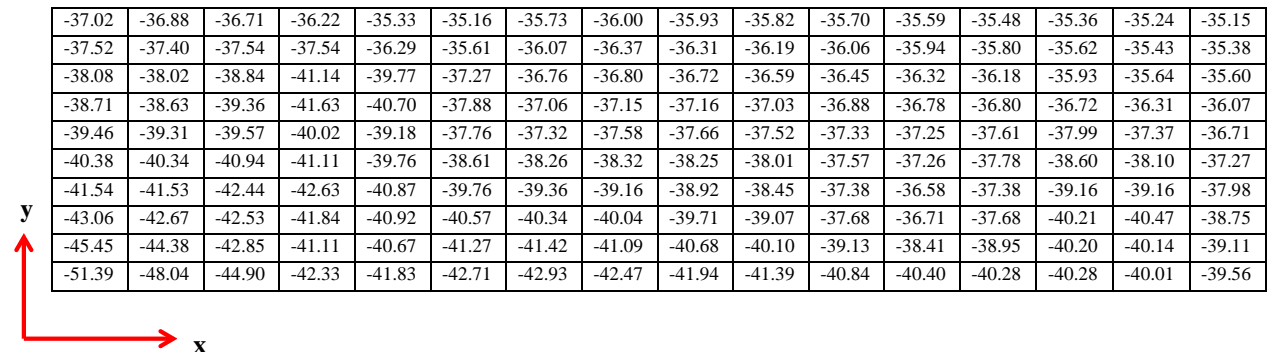
-38.23	-38.04	-37.67	-36.87	-35.76	-35.70	-36.44	-37.01	-37.32	-37.43	-37.41	-37.27	-37.04	-36.76	-36.58	-36.61
-38.52	-38.48	-38.41	-37.98	-36.06	-35.78	-36.67	-37.19	-37.44	-37.52	-37.47	-37.28	-36.94	-36.47	-36.14	-36.26
-38.84	-38.97	-39.39	-40.95	-40.32	-37.60	-37.39	-37.50	-37.60	-37.63	-37.56	-37.38	-37.03	-36.34	-35.72	-36.03
-39.16	-39.36	-39.71	-40.46	-39.84	-37.90	-37.55	-37.67	-37.75	-37.74	-37.67	-37.57	-37.45	-37.08	-36.30	-36.43
-39.49	-39.77	-40.06	-39.94	-38.94	-37.56	-37.41	-37.75	-37.88	-37.83	-37.73	-37.72	-37.89	-38.20	-37.74	-37.34
-39.78	-40.29	-41.16	-41.57	-39.78	-38.32	-37.94	-38.03	-38.05	-37.90	-37.65	-37.57	-37.91	-38.21	-38.22	-38.05
-39.95	-40.52	-41.53	-42.15	-40.46	-39.16	-38.60	-38.41	-38.29	-38.02	-37.40	-36.87	-37.61	-39.06	-39.39	-38.77
-39.96	-40.35	-40.77	-40.84	-40.35	-39.63	-39.05	-38.77	-38.69	-38.58	-37.67	-36.61	-37.56	-40.12	-40.34	-39.23
-39.90	-40.18	-40.48	-40.75	-40.69	-39.99	-39.35	-39.05	-39.18	-39.80	-39.49	-37.96	-38.13	-39.16	-39.49	-39.08
-39.81	-40.07	-40.38	-40.74	-40.70	-40.07	-39.47	-39.20	-39.35	-39.88	-39.76	-38.77	-38.50	-38.73	-38.89	-38.81

Table 6.6: XY received power grid for Loughborough University workshop using kriging Gaussian. The grid shows 16 by 10 grid points which represent the receiver locations in the deterministic model



-38.23	-38.23	-38.23	-38.24	-37.48	-37.51	-38.22	-38.23	-38.23	-38.23	-38.23	-38.23	-38.23	-38.23	-38.18	-38.22
-38.23	-38.23	-38.24	-38.95	-38.99	-38.23	-38.23	-38.23	-38.23	-38.23	-38.23	-38.23	-38.23	-38.16	-36.23	-38.02
-38.23	-38.23	-38.23	-38.41	-38.42	-38.19	-38.17	-38.23	-38.23	-38.23	-38.23	-38.23	-38.23	-38.21	-37.93	-38.18
-38.23	-38.23	-38.23	-38.24	-38.23	-37.99	-37.90	-38.23	-38.23	-38.23	-38.23	-38.23	-38.23	-38.25	-38.23	-38.23
-38.23	-38.23	-38.33	-38.74	-38.25	-38.22	-38.22	-38.23	-38.23	-38.23	-38.23	-38.23	-38.23	-38.24	-38.23	-38.23
-38.23	-38.23	-38.43	-39.61	-38.27	-38.23	-38.23	-38.23	-38.23	-38.23	-38.21	-37.89	-38.19	-38.32	-38.32	-38.23
-38.23	-38.23	-38.24	-38.25	-38.24	-38.23	-38.23	-38.23	-38.23	-38.24	-38.19	-37.19	-38.14	-38.85	-38.85	-38.24
-38.23	-38.23	-38.24	-38.54	-38.54	-38.24	-38.23	-38.23	-38.24	-38.53	-38.52	-38.22	-38.23	-38.25	-38.25	-38.23
-38.23	-38.23	-38.24	-38.54	-38.54	-38.24	-38.23	-38.23	-38.24	-38.45	-38.45	-38.24	-38.23	-38.23	-38.23	-38.23
-38.23	-38.23	-38.23	-38.24	-38.24	-38.23	-38.23	-38.23	-38.23	-38.23	-38.23	-38.23	-38.23	-38.23	-38.23	-38.23

Table 6.7: XY received power grid for Loughborough University workshop using RBF Gaussian. The grid shows 16 by 10 grid points which represent the receiver locations in the deterministic model



-37.02	-36.88	-36.71	-36.22	-35.33	-35.16	-35.73	-36.00	-35.93	-35.82	-35.70	-35.59	-35.48	-35.36	-35.24	-35.15
-37.52	-37.40	-37.54	-37.54	-36.29	-35.61	-36.07	-36.37	-36.31	-36.19	-36.06	-35.94	-35.80	-35.62	-35.43	-35.38
-38.08	-38.02	-38.84	-41.14	-39.77	-37.27	-36.76	-36.80	-36.72	-36.59	-36.45	-36.32	-36.18	-35.93	-35.64	-35.60
-38.71	-38.63	-39.36	-41.63	-40.70	-37.88	-37.06	-37.15	-37.16	-37.03	-36.88	-36.78	-36.80	-36.72	-36.31	-36.07
-39.46	-39.31	-39.57	-40.02	-39.18	-37.76	-37.32	-37.58	-37.66	-37.52	-37.33	-37.25	-37.61	-37.99	-37.37	-36.71
-40.38	-40.34	-40.94	-41.11	-39.76	-38.61	-38.26	-38.32	-38.25	-38.01	-37.57	-37.26	-37.78	-38.60	-38.10	-37.27
-41.54	-41.53	-42.44	-42.63	-40.87	-39.76	-39.36	-39.16	-38.92	-38.45	-37.38	-36.58	-37.38	-39.16	-39.16	-37.98
-43.06	-42.67	-42.53	-41.84	-40.92	-40.57	-40.34	-40.04	-39.71	-39.07	-37.68	-36.71	-37.68	-40.21	-40.47	-38.75
-45.45	-44.38	-42.85	-41.11	-40.67	-41.27	-41.42	-41.09	-40.68	-40.10	-39.13	-38.41	-38.95	-40.20	-40.14	-39.11
-51.39	-48.04	-44.90	-42.33	-41.83	-42.71	-42.93	-42.47	-41.94	-41.39	-40.84	-40.40	-40.28	-40.28	-40.01	-39.56

## 6.5 Summary

In this chapter, widely known and accepted interpolation techniques have been used to estimate RF power density levels at unsampled locations and the available energy profiles for low power devices has been estimated. The inverse distance weighting global interpolation method showed the least prediction error at both the DEP and the University workshop. Also the energy profile estimated in the University workshop showed that RF energy harvesting was feasible using IRs. This was accomplished by using five IRs simultaneously transmitting at 0 dBm over a floor plan area of 187 m<sup>2</sup>. Extending this power distance versus floor area relationship to a factory of similar dimension of the DEP (160,735 m<sup>2</sup>), about 4,297 active transmitters (0 dBm; 2 dBi) will be required to create a receive power threshold of -40 dBm across the entire floor area <sup>1</sup>. In the next chapter, the industrial application of this thesis is presented as well as ideas for future research.

---

<sup>1</sup>This value aligns with the Friis transmission formula assuming a circular coverage area for the transmitting antenna

# Chapter 7

## Conclusions and Future Work

### 7.1 Summary of Research Novelty

This thesis has presented ambient energy measurement data obtained from an automobile factory in the UK. The ambient energy domains characterized provide system design parameters regarding the energy profile obtainable at the plant. The results presented are representative of factories in the UK with most factories located on the outskirts of many cities or away from residential areas. Thus, the measurement data gathered can be reversed engineered to determine if a particular energy harvesting technique is suitable at a particular plant.

Also, this research work has characterized a machine workshop with respect to small-scale fading effects. Unlike most of the measurement data in the literature, the delay spread results obtained provide valuable time dispersion information for machine workshops and factory like environments. This time dispersion of the wireless channel can be used in designing efficient RF receivers that would be located in workshop areas.

In addition, this thesis presented a technique for obtaining delay spread in workshop environments without information of the inventory. The algorithm presented can be used in deterministically modelling machine workshops so as to obtain information about radio coverage and transceiver performance for wireless communication technologies. This technique provides a means of rapidly generating objects in a propagation software, which can then be used to obtain additional information relating to BER, throughput, carrier to interference ratio and signal to noise ratio prior to deploying the wireless com-

munication technology.

Furthermore, the suitability of spatial interpolation for predicting received power was investigated in this research. The error measures obtained from the interpolation techniques can be used to guide system designers in applying these techniques to wireless propagation. It was also shown that by using spatial interpolation, it is possible to rapidly obtain the distribution of received power by interpolating sparse control points. Using spatial interpolation methods, an overlaying grid of the received power was created in this thesis. This grid was used to mathematically estimate how much power a sensor device is exposed to during its time of flight. This method can be used to determine the applicability of a RFEH based on the RF coverage provided by the transmitter(s) in the location.

## **7.2 Industrial Applications**

The 3-D fractal overlay technique presented in this thesis shows a novel approach to populating floor spaces in deterministic wireless channel modelling. Deterministic modelling of the wireless channel requires that the floor space be correctly specified in the ray tracing software. In some scenarios, the exact information on the inventory is not available prior to deploying a wireless communication network. Using fractal overlays, commercial software vendors can include this feature in floor editing modules of ray tracing packages. Consequently, providing a means of allowing system designers to rapidly obtain approximate channel behaviour of floor spaces without inventory knowledge.

## **7.3 Suggestions for Future Work**

This thesis has focused on modelling the wireless communication channel in multipath prone environments. The model presented can be used to replicate multipath environments, which can then be used to mathematically compute the received power and probable harvestable ambient power. Based on the ability of the model to predict the time dispersion in the workshop models investigated, the following areas provide potential

and opportunities for future research work.

1. Investigating how the fractal overlay algorithm can be used to predict delay spread in residential and office environments. The communication channel in these environment presents different characteristics due to the type of inventory and floor space. Obtaining a fractal overlay algorithm that caters for more than one environment provides opportunities for adapting this technique in deterministic modelling.
2. Angular spread and small-scale fading parameters such as angle-of-arrival can be investigated to extend the suitability of the fractal overlaying model. While delay spread gives information on the time dispersion, the ability to model arrival angles allows the technique to be applied to MIMO and beamforming scenarios.
3. Carrying out ultra-wideband ray tracing simulations for similar workshop environments in order to evaluate the delay spread prediction ability of the fractal overlay model. This provides an opportunity to extend the capabilities of the fractal algorithm presented in this work.



# References

- [1] European Factories of the Future Research Association, “Factories 4.0: The Future of European Manufacturing.” [Online]. Available: <https://ec.europa.eu/digital-single-market/en/blog/factories-40-future-european-manufacturing>
- [2] G. Trade and Invest, “Industrie 4.0, Smart Manufacturing for the Future.” [Online]. Available: <https://www.gtai.de>
- [3] X. Lu, “Analysis and optimal design of micro-energy harvesting systems for wireless sensor nodes,” Ph.D. dissertation, Loughborough University, 2012. [Online]. Available: <https://dspace.lboro.ac.uk/dspace-jspui/handle/2134/11011>
- [4] V. Raghunathan, C. Schurgers, S. Park, and M. B. Srivastava, “Energy-aware wireless microsensor networks,” *IEEE Signal Processing Magazine*, vol. 19, no. 2, pp. 40–50, Mar 2002.
- [5] J. W. Matiko, N. J. Grabham, S. P. Beeby, and M. J. Tudor, “Review of the application of energy harvesting in buildings,” *Measurement Science and Technology*, vol. 25, no. 1, p. 012002, Jan. 2014. [Online]. Available: <http://stacks.iop.org/0957-0233/25/i=1/a=012002?key=crossref.55cc48502ddfb112bc50baf06a58d62>
- [6] S. P. Beeby, M. J. Tudor, and N. M. White, “Energy harvesting vibration sources for microsystems applications,” *Measurement Science and Technology*, vol. 17, no. 12, pp. R175–R195, Dec. 2006. [Online]. Available: <http://stacks.iop.org/0957-0233/17/i=12/a=R01?key=crossref.ff55f78e312657545b6c23c0fad808ad>

- [7] Zigbee Alliance, “Zigbee.” [Online]. Available: <http://www.zigbee.org/>
- [8] J. M. Rabaey, M. J. Ammer, J. L. da Silva, D. Patel, and S. Roundy, “Picoradio supports ad hoc ultra-low power wireless networking,” *Computer*, vol. 33, no. 7, pp. 42–48, Jul 2000.
- [9] R. J. M. Vullers, R. van Schaijk, I. Doms, C. Van Hoof, and R. Mertens, “Micropower energy harvesting,” *Solid-State Electronics*, vol. 53, no. 7, pp. 684–693, Jul. 2009. [Online]. Available: <http://linkinghub.elsevier.com/retrieve/pii/S0038110109000720>
- [10] P. D. Mitcheson, E. M. Yeatman, G. K. Rao, A. S. Holmes, and T. C. Green, “Human and Machine Motion for Wireless Electronic Devices,” *Proceedings of the IEEE*, vol. 96, no. 9, pp. 1457–1486, 2008.
- [11] S. J. Roundy, “Energy Scavenging for Wireless Sensor Nodes with a Focus on Vibration to Electricity Conversion,” Ph.D. dissertation, The University of California, Berkeley, 2003.
- [12] W. B. Heinzelman, A. P. Chandrakasan, S. Member, and H. Balakrishnan, “An Application-Specific Protocol Architecture for Wireless Microsensor Networks,” *IEEE Transaction on Wireless Communication*, vol. 1, no. 4, pp. 660–670, 2002.
- [13] A. Wang and A. Chandrakasan, “Energy-efficient dsps for wireless sensor networks,” *IEEE Signal Processing Magazine*, vol. 19, no. 4, pp. 68–78, Jul 2002.
- [14] R. Yan, H. Sun, and Y. Qian, “Energy-aware sensor node design with its application in wireless sensor networks,” *IEEE Transactions on Instrumentation and Measurement*, vol. 62, no. 5, pp. 1183–1191, May 2013.
- [15] J. Volakis, U. Olgun, and C.-C. Chen, “Design of an efficient ambient WiFi energy harvesting system,” *IET Microwaves, Antennas & Propagation*, vol. 6, no. 11, pp. 1200–1206, Aug. 2012. [Online]. Available: <http://digital-library.theiet.org/content/journals/10.1049/iet-map.2012.0129>

- [16] R. Jurdak, A. G. Ruzzelli, and G. M. P. O'Hare, "Radio sleep mode optimization in wireless sensor networks," *IEEE Transactions on Mobile Computing*, vol. 9, no. 7, pp. 955–968, July 2010.
- [17] Z. Popović, S. Korhummel, S. Dumbar, R. Scheeler, A. Dolgov, R. Zane, E. Falkenstein, and J. Hagerty, "Scalable RF energy harvesting," *IEEE Transactions on Microwave Theory and Techniques*, vol. 62, no. 4, pp. 1046–1056, 2014. [Online]. Available: <http://ecee.colorado.edu/microwave/docs/publications/2014/Popovic2014a.pdf>
- [18] P. Ltd, "Perpetuum pmg17," <http://www.perpetuum.com/pmg17.asp>.
- [19] H. J. Goldsmid, *The Physics of Thermoelectric Energy Conversion*, ser. 2053-2571. Morgan & Claypool Publishers, 2017. [Online]. Available: <http://dx.doi.org/10.1088/978-1-6817-4641-8>
- [20] J. A. Paradiso and T. Starner, "Energy scavenging for mobile and wireless electronics," *IEEE Pervasive Computing*, vol. 4, no. 1, pp. 18–27, Jan 2005.
- [21] M. H. Straughn and C.-C. Chen, "Efficient RF energy harvesting circuitry study," in *2016 10th European Conference on Antennas and Propagation (EuCAP)*, April 2016, pp. 1–4.
- [22] A. Wickenheiser and E. Garcia, "Combined Power Harvesting from AC and DC Sources," in *Proceedings of the SPIE*, M. Ahmadian and M. N. Ghasemi-Nejhad, Eds., vol. 7288, mar 2009, pp. 728 816–728 816–9. [Online]. Available: <http://proceedings.spiedigitallibrary.org/proceeding.aspx?articleid=822107>
- [23] D. Carli, D. Brunelli, L. Benini, and M. Ruggeri, "An effective multi-source energy harvester for low power applications," *2011 Design, Automation & Test in Europe*, pp. 1–6, mar 2011. [Online]. Available: <http://ieeexplore.ieee.org/lpdocs/epic03/wrapper.htm?arnumber=5763142>
- [24] A. Schlichting, R. Tiwari, and E. Garcia, "Passive multi-source energy harvesting schemes," *Journal of Intelligent Material Systems and Structures*, vol. 23, no. 17, pp. 1921–1935, 2012.

- [25] C. Park and P. Chou, "Ambimax: Autonomous energy harvesting platform for multi-supply wireless sensor nodes," *IEEE SECON*, pp. 168–177, 2006. [Online]. Available: [http://ieeexplore.ieee.org/xpls/abs\\_all.jsp?arnumber=4068119](http://ieeexplore.ieee.org/xpls/abs_all.jsp?arnumber=4068119)
- [26] A. Collado and A. Georgiadis, "Conformal Hybrid Solar and Electromagnetic (EM) Energy Harvesting Rectenna," *IEEE Transactions on Circuits and Systems I: Regular Papers*, vol. 60, no. 8, pp. 2225–2234, Aug 2013.
- [27] M. Cheffena, "Industrial indoor multipath propagation : A physical-statistical approach," in *IEEE 25th Annual International Symposium on Personal, Indoor, and Mobile Radio Communication (PIMRC)*, Sept 2014, pp. 68–72.
- [28] E. I. Adegoke, R. M. Edwards, W. Whittow, and A. Bindel, "RF Power Density Measurements for RF Energy Harvesting in Automobile Factories," in *Loughborough Antennas and Propagation Conference (LAPC)*, 2015.
- [29] E. Adegoke, R. Edwards, W. Whittow, A. Bindel, and M. Peca, "Opportunities for energy harvesting in automobile factories," in *SPIE Smart Structures and Materials+ Nondestructive Evaluation and Health Monitoring*. International Society for Optics and Photonics, 2016, pp. 97 992N–97 992N.
- [30] E. I. Adegoke, R. M. Edwards, W. Whittow, and A. Bindel, "Evaluating 2-D grid interpolation techniques for predicting ambient RF power density in automobile factories," in *The 10th European Conference on Antennas and Propagation (EuCAP)*, 2016.
- [31] A. Goldsmith, *Wireless Communications*. Cambridge University Press, 2005. [Online]. Available: [https://books.google.co.uk/books?id=mF7X\\_8D7\\_BIC](https://books.google.co.uk/books?id=mF7X_8D7_BIC)
- [32] CISCO, "Cisco Visual Networking Index: Global Mobile Data Traffic Forecast Update, 2016–2021 White Paper," <http://www.cisco.com/c/en/us/solutions/collateral/service-provider/visual-networking-index-vni/mobile-white-paper-c11-520862.html>.
- [33] Madison Technologies, "Reliable wireless communication for factory automation," <http://www.processonline.com.au/content/industrial-networks->

buses/article/reliable-wireless-communication-for-factory-automation-222560895.

- [34] T. Rappaport, *Wireless Communications: Principles and Practice*, 2nd ed. Upper Saddle River, NJ, USA: Prentice Hall PTR, 2001.
- [35] A. Molisch, *Wireless Communications*, ser. Wiley - IEEE. Wiley, 2012. [Online]. Available: <https://books.google.co.uk/books?id=877tFGeQo5oC>
- [36] K. Pahlavan and A. Levesque, *Wireless Information Networks*, ser. Wiley Series in Telecommunications and Signal Processing. Wiley, 2005. [Online]. Available: <https://books.google.co.uk/books?id=6vhSAAAAMAAJ>
- [37] T. S. Rappaport and C. D. McGillem, "UHF fading in factories," *IEEE Journal on Selected Areas in Communications*, vol. 7, no. 1, pp. 40–48, Jan 1989.
- [38] S. Y. Seidel and T. S. Rappaport, "Site-specific propagation prediction for wireless in-building personal communication system design," *IEEE transactions on Vehicular Technology*, vol. 43, no. 4, pp. 879–891, 1994.
- [39] A. A. M. Saleh and R. Valenzuela, "A statistical model for indoor multipath propagation," *IEEE Journal on Selected Areas in Communications*, vol. 5, no. 2, pp. 128–137, February 1987.
- [40] T. S. Rappaport, "Characterization of uhf multipath radio channels in factory buildings," *IEEE Transactions on Antennas and Propagation*, vol. 37, no. 8, pp. 1058–1069, 1989.
- [41] M. Z. Win, R. A. Scholtz, and M. A. Barnes, "Ultra-wide bandwidth signal propagation for indoor wireless communications," in *Communications, 1997. ICC'97 Montreal, Towards the Knowledge Millennium. 1997 IEEE International Conference on*, vol. 1. IEEE, 1997, pp. 56–60.
- [42] M. J. Feuerstein, K. L. Blackard, T. S. Rappaport, S. Y. Seidel, and H. H. Xia, "Path loss, delay spread, and outage models as functions of antenna height for microcellular system design," *IEEE Transactions on Vehicular Technology*, vol. 43, no. 3, pp. 487–498, 1994.

- [43] T. S. Rappaport, "Indoor radio communications for factories of the future," *IEEE Communications Magazine*, vol. 27, no. 5, pp. 15–24, 1989.
- [44] E. Tanghe, W. Joseph, L. Verloock, L. Martens, H. Capoen, K. Van Herwegen, and W. Vantomme, "The industrial indoor channel: large-scale and temporal fading at 900, 2400, and 5200 MHz," *IEEE Transactions on Wireless Communications*, vol. 7, no. 7, 2008.
- [45] N. Moraitis and P. Constantinou, "Indoor channel measurements and characterization at 60 GHz for wireless local area network applications," *IEEE Transactions on Antennas and Propagation*, vol. 52, no. 12, pp. 3180–3189, 2004.
- [46] N. Patwari and J. Wilson, "Rf sensor networks for device-free localization: Measurements, models, and algorithms," *Proceedings of the IEEE*, vol. 98, no. 11, pp. 1961–1973, 2010.
- [47] A. Ranjany, P. Misraz, B. Dwivediz, and H. B. Sahuy, "Channel modeling of wireless communication in underground coal mines," in *2016 8th International Conference on Communication Systems and Networks (COMSNETS)*, Jan 2016, pp. 1–2.
- [48] M. Boutin, A. Benzakour, C. Despins, and S. Affes, "Characterization and modeling of a wireless channel at 2.4 and 5.8 GHz in underground tunnels," in *2006 3rd International Symposium on Wireless Communication Systems*, Sept 2006, pp. 517–521.
- [49] B. Nkakanou, G. Y. Delisle, and N. Hakem, "Experimental characterization of ultra-wideband channel parameter measurements in an underground mine," *Journal of Computer Networks and Communications*, vol. 2011, 2011.
- [50] M. Boutin, A. Benzakour, C. L. Despins, and S. Affes, "Radio wave characterization and modeling in underground mine tunnels," *IEEE Transactions on Antennas and Propagation*, vol. 56, no. 2, pp. 540–549, Feb 2008.

- [51] M. Hata, "Empirical formula for propagation loss in land mobile radio services," *IEEE Transactions on Vehicular Technology*, vol. 29, no. 3, pp. 317–325, Aug 1980.
- [52] Y. Ebine, T. Takahashi, and Y. Yamada, "A study of vertical space diversity for a land mobile radio," *Electronics and Communications in Japan (Part I: Communications)*, vol. 74, no. 10, pp. 68–76, 1991. [Online]. Available: <http://dx.doi.org/10.1002/ecja.4410741007>
- [53] S. Y. Seidel, T. S. Rappaport, M. J. Feuerstein, K. L. Blackard, and L. Grindstaff, "The impact of surrounding buildings on propagation for wireless in-building personal communications system design," in *1992 Proceedings Vehicular Technology Society 42nd VTS Conference - Frontiers of Technology*, May 1992, pp. 814–818 vol.2.
- [54] M. Failli, *Cost 207 Digital Land Mobile Radio Communications: Final Réport*, 14 March 1984, 13 September 1988, ser. Euratom publications - EUR. Office for Office Publ. of the European Communities, 1989. [Online]. Available: <https://books.google.co.uk/books?id=nZbVPgAACAAJ>
- [55] H. Ling, R. C. Chou, and S. W. Lee, "Shooting and bouncing rays: calculating the RCS of an arbitrarily shaped cavity," *IEEE Transactions on Antennas and Propagation*, vol. 37, no. 2, pp. 194–205, Feb 1989.
- [56] Z. Yun and M. F. Iskander, "Ray tracing for radio propagation modeling: Principles and applications," *IEEE Access*, vol. 3, pp. 1089–1100, 2015.
- [57] M. F. Iskander and Z. Yun, "Propagation prediction models for wireless communication systems," *IEEE Transactions on Microwave Theory and Techniques*, vol. 50, no. 3, pp. 662–673, Mar 2002.
- [58] S. Y. Tan and H. S. Tan, "A microcellular communications propagation model based on the uniform theory of diffraction and multiple image theory," *IEEE Transactions on Antennas and Propagation*, vol. 44, no. 10, pp. 1317–1326, Oct 1996.

- [59] K. R. Schaubach, N. J. Davis, and T. S. Rappaport, "A ray tracing method for predicting path loss and delay spread in microcellular environments," in *[1992 Proceedings] Vehicular Technology Society 42nd VTS Conference - Frontiers of Technology*, May 1992, pp. 932–935 vol.2.
- [60] A. O. Kaya, L. J. Greenstein, and W. Trappe, "Characterizing indoor wireless channels via ray tracing combined with stochastic modeling," *IEEE Transactions on Wireless Communications*, vol. 8, no. 8, pp. 4165–4175, August 2009.
- [61] F. Mani, F. Quitin, and C. Oestges, "Accuracy of depolarization and delay spread predictions using advanced ray-based modeling in indoor scenarios," *EURASIP Journal on Wireless Communications and Networking*, vol. 2011, no. 1, p. 11, Jun 2011. [Online]. Available: <http://dx.doi.org/10.1186/1687-1499-2011-11>
- [62] S. Hur, S. Baek, B. Kim, J. Park, A. F. Molisch, K. Haneda, and M. Peter, "28 ghz channel modeling using 3d ray-tracing in urban environments," in *2015 9th European Conference on Antennas and Propagation (EuCAP)*, May 2015, pp. 1–5.
- [63] J. H. Kim, M. W. Jung, Y. K. Yoon, Y. J. Chong, and M. S. Song, "60 and 28 GHz delay spread measurements and simulation at indoor," in *2014 International Conference on Information and Communication Technology Convergence (ICTC)*, Oct 2014, pp. 148–150.
- [64] A. O. Kaya, D. Calin, and H. Viswanathan, "28 GHz and 3.5 GHz wireless channels: Fading, delay and angular dispersion," in *2016 IEEE Global Communications Conference (GLOBECOM)*, Dec 2016, pp. 1–7.
- [65] M. Gorlatova, A. Wallwater, and G. Zussman, "Networking low-power energy harvesting devices: Measurements and algorithms," in *The 30th IEEE International Conference on Computer Communications (IEEE INFOCOM)*, April 2011, pp. 1602–1610.
- [66] J. Gummesson, S. S. Clark, K. Fu, and D. Ganesan, "On the limits of effective hybrid micro-energy harvesting on mobile CRFID sensors," in *The*



- 8th International Conference on Mobile Systems, Applications, and Services*, ser. MobiSys '10. New York, NY, USA: ACM, 2010, pp. 195–208. [Online]. Available: <http://doi.acm.org/10.1145/1814433.1814454>
- [67] N. F. Tinsley, S. T. Witts, J. M. Ansell, E. Barnes, S. M. Jenkins, D. Raveendran, G. V. Merrett, and A. S. Weddell, “Enspect: A complete tool using modeling and real data to assist the design of energy harvesting systems,” in *Proceedings of the 3rd International Workshop on Energy Harvesting*, ser. ENSsys '15. New York, NY, USA: ACM, 2015, pp. 27–32. [Online]. Available: <http://doi.acm.org/10.1145/2820645.2820648>
- [68] O. Nizhnik, U. Maksudi, S. Okochi, K. Higuchi, and K. Maenaka, “The availability and statistical properties of ambient light for energy-harvesting for wearable sensor nodes,” in *The Sixth International Conference on Sensor Technologies and Applications (SENSORCOMM)*, 2012, pp. 119–122.
- [69] M. Gorlatova, A. Wallwater, and G. Zussman, “Networking low-power energy harvesting devices: Measurements and algorithms,” *IEEE Transactions on Mobile Computing*, vol. 12, no. 9, pp. 1853–1865, Sept 2013.
- [70] J. Sarik, K. Kim, M. Gorlatova, I. Kymissis, and G. Zussman, “More than meets the eye - a portable measurement unit for characterizing light energy availability,” in *Global Conference on Signal and Information Processing (GlobalSIP)*, 2013 *IEEE*, Dec 2013, pp. 387–390.
- [71] R. Denker and A. Muhtaroglu, “Feasibility analysis and proof of concept for thermoelectric energy harvesting in mobile computers,” *Journal of Renewable and Sustainable Energy*, vol. 5, no. 2, pp. 1–16, 2013. [Online]. Available: <http://scitation.aip.org/content/aip/journal/jrse/5/2/10.1063/1.4794751>
- [72] M. Wahbah, M. Alhawari, B. Mohammad, H. Saleh, and M. Ismail, “Characterization of human body-based thermal and vibration energy harvesting for wearable devices,” *IEEE Journal on Emerging and Selected Topics in Circuits and Systems*, vol. 4, no. 3, pp. 354–363, Sep. 2014.

- [73] Micropelt, “TGP 651/TGP 751 thermal generator datasheet,” [www.micropelt.com/products/thermogenerator.php](http://www.micropelt.com/products/thermogenerator.php).
- [74] M. Piñuela, P. D. Mitcheson, and S. Lucyszyn, “Ambient RF energy harvesting in urban and semi-urban environments,” *IEEE Transaction on Microwave Theory and Techniques*, vol. 61, no. 7, pp. 2715–2726, 2013.
- [75] S. M. Mann, T. G. Cooper, S. G. Allen, R. P. Blackwell, and A. J. Lowe, “NRPB-R321: Exposure to radio waves near mobile phone base stations,” National Radiological Protection Board (now part of Public Health England), Tech. Rep. June, 2000. [Online]. Available: <http://www.statesassembly.gov.je/ScrutinyReviewResearches/2007/9701-12777-1912007.pdf>
- [76] F. Apollonio, L. Ardoino, and E. Barbieri, “Definition and development of an automatic procedure for narrowband measurements,” *Radiation Protection Dosimetry*, vol. 97, no. 4, pp. 375–381, 2001. [Online]. Available: <http://rpd.oxfordjournals.org/content/97/4/375.short>
- [77] H. J. Visser, A. C. F. Reniers, and J. A. C. Theeuwes, “Ambient RF Energy Scavenging: GSM and WLAN Power Density Measurements,” in *Microwave Conference, 2008. EuMC 2008. 38th European*, Oct 2008, pp. 721–724.
- [78] T. G. Cooper, S. M. Mann, M. Khalid, and R. P. Blackwell, “Public exposure to radio waves near GSM microcell and picocell base stations.” *Journal of radiological protection : official journal of the Society for Radiological Protection*, vol. 26, no. 2, pp. 199–211, jun 2006. [Online]. Available: <http://www.ncbi.nlm.nih.gov/pubmed/16738416>
- [79] U. Bergqvist, G. Friedrich, Y. Hamnerius, and L. Martens, “Mobile telecommunication base stations – exposure to electromagnetic fields Report of a Short Term Mission within COST 244bis,” European Co-operative for Scientific and Technical Research, Tech. Rep., 2000.

- [80] A. Rahman and J. Kian, "Microwave radiation safety assessment near cellular base stations," in *1st International Conference on Computers, Communications, & Signal Processing with Special Track on Biomedical Engineering*, 2005, pp. 1–5.
- [81] V. Nitu, G. Lojewski, and S. Nitu, "Electromagnetic field evaluation on an antenna shared site," in *IEEE EUROCON*, 2009, pp. 70–75.
- [82] H. Ryser, "Measuring campaign for the assessment of the non-ionising radiation near GSM base stations," in *International Zurich Symposium on EMC, Zurich*, 2003, pp. 2–5.
- [83] K. Gudan, S. Chemishkian, and J. Hull, "Feasibility of wireless sensors using ambient 2.4 GHz RF energy," in *IEEE Sensors Conference*, 2012, pp. 2–5.
- [84] Kipp & Zonen Pyranometer, "SP Lite Pyranometer," <http://www.kippzonen.com/Product/9/SP-Lite2-Pyranometer#.VMFqHCusUfA>.
- [85] Grant Instruments, "Squirrel SQ2020," <http://www.grantinstruments.com/squirrel-sq2020-data-loggers/>.
- [86] G. by G24 Power, "Gcell dye sensitized solar cell," <http://gcell.com/dye-sensitized-solar-cells>.
- [87] Calex, "Calex pen style infrared thermometer," <http://uk.rs-online.com/web/p/ir-thermometers/3692006/>.
- [88] S. Miclaus and P. Bechet, "Estimated and measured values of the radiofrequency radiation power density around cellular base stations," *Romanian Journal of Physics*, vol. 52, no. July 2006, pp. 429–440, 2007. [Online]. Available: [http://www.nipne.ro/rjp/2007\\_52\\_3-4/0429\\_0441.pdf](http://www.nipne.ro/rjp/2007_52_3-4/0429_0441.pdf)
- [89] D. Bouchouicha, F. Dupont, M. Latrach, and L. Ventura, "Ambient RF energy harvesting," in *International Conference on Renewable Energies and Power Quality (ICREPPQ)*, 2010, pp. 2–6.

- [90] S. Keyrouz, H. J. Visser, and A. G. Tijhuis, "Multi-band simultaneous radio frequency energy harvesting," in *2013 7th European Conference on Antennas and Propagation (EuCAP)*, April 2013, pp. 3058–3061.
- [91] J. M. Barcak and H. P. Partal, "Efficient RF energy harvesting by using multiband microstrip antenna arrays with multistage rectifiers," in *2012 IEEE Subthreshold Microelectronics Conference (SubVT)*, Oct 2012, pp. 1–3.
- [92] V. Kuhn, C. Lahuec, F. Seguin, and C. Person, "A multi-band stacked RF energy harvester with rf-to-dc efficiency up to 84%," *IEEE Transactions on Microwave Theory and Techniques*, vol. 63, no. 5, pp. 1768–1778, May 2015.
- [93] A. Okba, A. Takacs, H. Aubert, S. Charlot, and P.-F. Calmon, "Multiband rectenna for microwave applications," *Comptes Rendus Physique*, vol. 18, no. 2, pp. 107 – 117, 2017, energy and radiosciences. [Online]. Available: <http://www.sciencedirect.com/science/article/pii/S1631070516301852>
- [94] M. T. Martinez-Ingles, D. P. Gaillot, J. Pascual-Garcia, J. M. Molina-Garcia-Pardo, M. Lienard, and J. V. Rodríguez, "Deterministic and experimental indoor mmw channel modeling," *IEEE Antennas and Wireless Propagation Letters*, vol. 13, pp. 1047–1050, 2014.
- [95] J. H. Jung, J. Lee, J. H. Lee, Y. H. Kim, and S. C. Kim, "Ray-tracing-aided modeling of user-shadowing effects in indoor wireless channels," *IEEE Transactions on Antennas and Propagation*, vol. 62, no. 6, pp. 3412–3416, June 2014.
- [96] R. Felbecker, W. Keusgen, and M. Peter, "Incabin millimeter wave propagation simulation in a wide-bodied aircraft using ray-tracing," in *2008 IEEE 68th Vehicular Technology Conference*, Sept 2008, pp. 1–5.
- [97] M. Peter, W. Keusgen, and R. Felbecker, "Measurement and ray-tracing simulation of the 60 ghz indoor broadband channel: Model accuracy and parameterization," in *The Second European Conference on Antennas and Propagation, EuCAP 2007*, Nov 2007, pp. 1–8.

- [98] F. Fuschini, H. El-Sallabi, V. Degli-Esposti, L. Vuokko, D. Guiducci, and P. Vainikainen, "Analysis of multipath propagation in urban environment through multidimensional measurements and advanced ray tracing simulation," *IEEE Transactions on Antennas and Propagation*, vol. 56, no. 3, pp. 848–857, March 2008.
- [99] X. H. Mao and Y. H. Lee, "UHF propagation along a cargo hold on board a merchant ship," *IEEE Transactions on Wireless Communications*, vol. 12, no. 1, pp. 22–30, January 2013.
- [100] S. Y. Seidel and T. S. Rappaport, "A ray tracing technique to predict path loss and delay spread inside buildings," in *Global Telecommunications Conference, 1992. Conference Record., GLOBECOM '92. Communication for Global Users., IEEE*, Dec 1992, pp. 649–653 vol.2.
- [101] T. S. Rappaport, "Characterization of UHF multipath radio channels in factory buildings," *IEEE Transactions on Antennas and Propagation*, vol. 37, no. 8, pp. 1058–1069, Aug 1989.
- [102] D. Cassioli and A. Durantini, "A time-domain propagation model of the UWB indoor channel in the FCC-compliant band 3.6 - 6 GHz based on PN-sequence channel measurements," in *2004 IEEE 59th Vehicular Technology Conference. VTC 2004-Spring (IEEE Cat. No.04CH37514)*, vol. 1, May 2004, pp. 213–217 Vol.1.
- [103] S. Deng, M. K. Samimi, and T. S. Rappaport, "28 GHz and 73 GHz millimeter-wave indoor propagation measurements and path loss models," in *2015 IEEE International Conference on Communication Workshop (ICCW)*, June 2015, pp. 1244–1250.
- [104] A. Dezfouliyan and A. M. Weiner, "Evaluation of time domain propagation measurements of UWB systems using spread spectrum channel sounding," *IEEE Transactions on Antennas and Propagation*, vol. 60, no. 10, pp. 4855–4865, Oct 2012.

- [105] G. R. Maccartney, T. S. Rappaport, S. Sun, and S. Deng, "Indoor office wideband millimeter-wave propagation measurements and channel models at 28 and 73 GHz for ultra-dense 5G wireless networks," *IEEE Access*, vol. 3, pp. 2388–2424, 2015.
- [106] S. Salous, S. M. Feeney, X. Raimundo, and A. A. Cheema, "Wideband mimo channel sounder for radio measurements in the 60 ghz band," *IEEE Transactions on Wireless Communications*, vol. 15, no. 4, pp. 2825–2832, April 2016.
- [107] C. R. Anderson and T. S. Rappaport, "In-building wideband partition loss measurements at 2.5 and 60 GHz," *IEEE Transactions on Wireless Communications*, vol. 3, no. 3, pp. 922–928, May 2004.
- [108] C. R. Anderson, T. S. Rappaport, K. Bae, A. Verstak, N. Ramakrishnan, W. H. Tranter, C. A. Shaffer, and L. T. Watson, "In-building wideband multipath characteristics at 2.5 and 60 GHz," in *Proceedings IEEE 56th Vehicular Technology Conference*, vol. 1, 2002, pp. 97–101 vol.1.
- [109] C. G. Spiliotopoulos and A. G. Kanatas, "Path-loss and time-dispersion parameters of uwb signals in a military airplane," *IEEE Antennas and Wireless Propagation Letters*, vol. 8, pp. 790–793, 2009.
- [110] J. Karedal, S. Wyne, P. Almers, F. Tufvesson, and A. F. Molisch, "A measurement-based statistical model for industrial ultra-wideband channels," *IEEE Transactions on Wireless Communications*, vol. 6, no. 8, pp. 3028–3037, August 2007.
- [111] E. Tanghe, W. Joseph, J. D. Bruyne, L. Verloock, and L. Martens, "The industrial indoor channel: Statistical analysis of the power delay profile," *AEU - International Journal of Electronics and Communications*, vol. 64, no. 9, pp. 806 – 812, 2010. [Online]. Available: <http://www.sciencedirect.com/science/article/pii/S1434841109001848>
- [112] Y. Ai, M. Cheffena, and Q. Li, "Power delay profile analysis and modeling of industrial indoor channels," in *2015 9th European Conference on Antennas and Propagation (EuCAP)*, May 2015, pp. 1–5.

- [113] S. J. Howard and K. Pahlavan, "Measurement and analysis of the indoor radio channel in the frequency domain," *IEEE Transactions on Instrumentation and Measurement*, vol. 39, no. 5, pp. 751–755, Oct 1990.
- [114] J. H. C. van den Heuvel, J. Romme, J. F. Dufour, G. Dolmans, N. F. Kiyani, K. Philips, and H. de Groot, "Uwb radio channel characterization and design for intra spacecraft communication," in *2013 IEEE International Conference on Communications (ICC)*, June 2013, pp. 5311–5316.
- [115] X. Raimundo, S. Salous, and K. Nasr, "UWB MIMO measurements in reverberation chamber and indoor environment," in *2012 International Symposium on Signals, Systems, and Electronics (ISSSE)*, Oct 2012, pp. 1–5.
- [116] H. Hashemi, "Impulse response modeling of indoor radio propagation channels," *IEEE Journal on Selected Areas in Communications*, vol. 11, no. 7, pp. 967–978, Sep 1993.
- [117] S. S. Ghassemzadeh, R. Jana, C. W. Rice, W. Turin, and V. Tarokh, "Measurement and modeling of an ultra-wide bandwidth indoor channel," *IEEE Transactions on Communications*, vol. 52, no. 10, pp. 1786–1796, Oct 2004.
- [118] J. He, Y. Geng, and K. Pahlavan, "Toward accurate human tracking: Modeling time-of-arrival for wireless wearable sensors in multipath environment," *IEEE Sensors Journal*, vol. 14, no. 11, pp. 3996–4006, Nov 2014.
- [119] S. Chiu, J. Chuang, and D. G. Michelson, "Characterization of uwb channel impulse responses within the passenger cabin of a boeing 737-200 aircraft," *IEEE Transactions on Antennas and Propagation*, vol. 58, no. 3, pp. 935–945, March 2010.
- [120] G. Zebrick, "Zigbee or Not Zigbee," 2004. [Online]. Available: <http://www.automatedbuildings.com/news/dec04/articles/kele/zebrick.htm>
- [121] Remcom, "Wireless InSite Propagation Software." [Online]. Available: <https://www.remcom.com/wireless-insite-em-propagation-software/>

- [122] M. Geach, M. Stokes, M. Telfer, A. Mather, R. Fyfe, and S. Lewin., “The application of geospatial interpolation methods in the reconstruction of quaternary landform records,” *Geomorphology*, vol. 216, no. Supplement C, pp. 234 – 246, 2014. [Online]. Available: <http://www.sciencedirect.com/science/article/pii/S0169555X14001706>
- [123] J. Li and A. D. Heap, “A review of comparative studies of spatial interpolation methods in environmental sciences: Performance and impact factors,” *Ecological Informatics*, vol. 6, no. 3, pp. 228 – 241, 2011. [Online]. Available: <http://www.sciencedirect.com/science/article/pii/S1574954110001147>
- [124] C. M. P. Ho and T. S. Rappaport, “Wireless channel prediction in a modern office building using an image-based ray tracing method,” in *Global Telecommunications Conference, 1993, including a Communications Theory Mini-Conference. Technical Program Conference Record, IEEE in Houston. GLOBECOM '93, IEEE*, Nov 1993, pp. 1247–1251 vol.2.
- [125] Crilly, A.J., Earnshaw Rae, Jones Huw, Ed., *Fractals and Chaos*. Springer, 1991. [Online]. Available: <http://www.springer.com/gp/book/9781461277705>
- [126] FractalFoundation, “What are Fractals?” [Online]. Available: <http://fractalfoundation.org/resources/what-are-fractals/>
- [127] F. Lefebvre, H. Benali, R. Gilles, E. Kahn, and R. Di Paola, “A fractal approach to the segmentation of microcalcifications in digital mammograms,” *Medical Physics*, vol. 22, no. 4, pp. 381–390, 1995. [Online]. Available: <http://dx.doi.org/10.1118/1.597473>
- [128] C. B. Caldwell, S. J. Stapleton, D. W. Holdsworth, R. A. Jong, W. J. Weiser, G. Cooke, and M. J. Yaffe, “Characterisation of mammographic parenchymal pattern by fractal dimension,” *Physics in Medicine & Biology*, vol. 35, no. 2, p. 235, 1990. [Online]. Available: <http://stacks.iop.org/0031-9155/35/i=2/a=004>
- [129] C. E. Priebe, J. L. Solka, R. A. Lorey, G. W. Rogers, W. L. Poston, M. Kallergi, W. Oian, L. P. Clarke, and R. A. Clark, “The



- application of fractal analysis to mammographic tissue classification,” *Cancer Letters*, vol. 77, no. 2, pp. 183 – 189, 1994, computer applications for early detection and staging of cancer. [Online]. Available: <http://www.sciencedirect.com/science/article/pii/0304383594901015>
- [130] A. Napolitano, S. Ungania, and V. Cannata, “Fractal dimension estimation methods for biomedical images,” in *MATLAB - A Fundamental Tool for Scientific Computing and Engineering Applications - Volume 3*, V. N. Katsikis, Ed. Rijeka: InTech, 2012, ch. 07. [Online]. Available: <http://dx.doi.org/10.5772/48760>
- [131] N. M., M. B. M., and G. T., “Quantification of echodensities in tuberculous pericardial effusion using fractal geometry: a proof of concept study,” *Cardiovascular Ultrasound*, vol. 10, no. 30, 2012. [Online]. Available: <https://www.ncbi.nlm.nih.gov/pmc/articles/PMC3464936/>
- [132] M. Chakraborty, T. Das, and D. Ghosh, “Non-linear fractal analysis of ecg signal collected from maternal and normal sinus women,” in *2016 3rd International Conference on Recent Advances in Information Technology (RAIT)*, March 2016, pp. 123–127.
- [133] N. Cohen, “Fractal antenna applications in wireless telecommunications,” in *Professional Program Proceedings. Electronic Industries Forum of New England*, May 1997, pp. 43–49.
- [134] K. J. Vinoy, K. A. Jose, V. K. Varadan, and V. V. Varadan, “Hilbert curve fractal antenna: A small resonant antenna for vhf/uhf applications,” *Microwave and Optical Technology Letters*, vol. 29, no. 4, pp. 215–219, 2001. [Online]. Available: <http://dx.doi.org/10.1002/mop.1136>
- [135] D. Li and J. f. Mao, “A koch-like sided fractal bow-tie dipole antenna,” *IEEE Transactions on Antennas and Propagation*, vol. 60, no. 5, pp. 2242–2251, May 2012.
- [136] B. S. Dhaliwal, S. S. Pattnaik, and J. Boparai, “A cross-stitch geometry-based multiband fractal antenna,” *Microwave and Optical Technol-*

- ogy Letters, vol. 56, no. 3, pp. 667–671, 2014. [Online]. Available: <http://dx.doi.org/10.1002/mop.28177>
- [137] V. V. Reddy and N. V. S. N. Sarma, “Compact circularly polarized asymmetrical fractal boundary microstrip antenna for wireless applications,” *IEEE Antennas and Wireless Propagation Letters*, vol. 13, pp. 118–121, 2014.
- [138] V. V. Reddy and N. Sarma, “Triband circularly polarized koch fractal boundary microstrip antenna,” *IEEE Antennas and Wireless Propagation Letters*, vol. 13, pp. 1057–1060, 2014.
- [139] L. Tang, K. C. Wang, Y. Huang, and F. Gu, “Channel characterization and link quality assessment of IEEE 802.15.4-compliant radio for factory environments,” *IEEE Transactions on Industrial Informatics*, vol. 3, no. 2, pp. 99–110, May 2007.
- [140] Wolfram, “Sierpinski Carpet Interactive Demonstration.” [Online]. Available: <http://mathworld.wolfram.com/SierpinskiCarpet.html>
- [141] Boston University Department of Mathematics, “Boston University Math homepage.” [Online]. Available: <http://math.bu.edu/DYSYS/chaos-game/node2.html>
- [142] The University of Georgia, “Matematics Education Progam.” [Online]. Available: <http://jwilson.coe.uga.edu/EMAT6680Fa11/Frailey/FractalEssay.htm>
- [143] A. F. Molisch, “Ultra-wide-band propagation channels,” *Proceedings of the IEEE*, vol. 97, no. 2, pp. 353–371, Feb 2009.
- [144] A. F. Molisch, K. Balakrishnan, C.-C. Chong, S. Emami, A. Fort, J. Karedal, J. Kunisch, H. Schantz, U. Schuster, and K. Siwiak, “IEEE 802.15. 4a channel model-final report,” *IEEE P802*, vol. 15, no. 04, p. 0662, 2004.
- [145] M. Toeltsch, J. Laurila, K. Kalliola, A. F. Molisch, P. Vainikainen, and E. Bonek, “Statistical characterization of urban spatial radio channels,” *IEEE Journal on Selected Areas in Communications*, vol. 20, no. 3, pp. 539–549, Apr 2002.

- [146] L. Vuokko, P. Vainikainen, and J. Takada, "Clusters extracted from measured propagation channels in macrocellular environments," *IEEE Transactions on Antennas and Propagation*, vol. 53, no. 12, pp. 4089–4098, Dec 2005.
- [147] V. Erceg, L. Schumacher, P. Kyritsi, A. Molisch, and D. S. Baum, "TGn Channel Models, IEEE P802.11 Wireless LANs," Tech. Rep., 2004. [Online]. Available: <http://www.802wirelessworld.com:8802/>
- [148] H. Yan, Z. Yu, Y. Du, J. He, X. Zou, D. Steer, and G. Wang, "Comparison of large scale parameters of mmwave wireless channel in 3 frequency bands," in *2016 International Symposium on Antennas and Propagation (ISAP)*, Oct 2016, pp. 606–607.
- [149] A. F. Molisch, J. R. Foerster, and M. Pendergrass, "Channel models for ultrawideband personal area networks," *IEEE Wireless Communications*, vol. 10, no. 6, pp. 14–21, Dec 2003.
- [150] R. Flowerdew, M. Green, and E. Kehris, "Using areal interpolation methods in geographic information systems," *Papers in Regional Science*, vol. 70, no. 3, pp. 303–315, Jul 1991. [Online]. Available: <https://doi.org/10.1007/BF01434424>
- [151] M. A. Oliver and R. Webster, "Kriging: a method of interpolation for geographical information systems," *International Journal of Geographical Information Systems*, vol. 4, no. 3, pp. 313–332, 1990.
- [152] L. Anselin and A. Getis, "Spatial statistical analysis and geographic information systems," *The Annals of Regional Science*, vol. 26, no. 1, pp. 19–33, Mar 1992. [Online]. Available: <https://doi.org/10.1007/BF01581478>
- [153] A. Vansarochana, N. K. Tripathi, and R. Clemente, "Finding appropriate interpolation techniques for topographic surface generation for mudslide risk zonation," *Geocarto International*, vol. 24, no. 4, pp. 313–332, 2009. [Online]. Available: <http://dx.doi.org/10.1080/10106040802547735>

- [154] R. W. Parrott, M. R. Styzt, P. Amburn, and D. Robinson, "Towards statistically optimal interpolation for 3d medical imaging," *IEEE Engineering in Medicine and Biology Magazine*, vol. 12, no. 3, pp. 49–59, Sept 1993.
- [155] S. Ramani, P. Thevenaz, and M. Unser, "Regularized interpolation for noisy images," *IEEE Transactions on Medical Imaging*, vol. 29, no. 2, pp. 543–558, Feb 2010.
- [156] S. M. U. Talha, T. Mairaj, W. Khan, S. M. Baqar, M. Talha, and M. Hassan, "Interpolation based enhancement of sparse-view projection data for low dose fbp reconstruction," in *2017 International Conference on Innovations in Electrical Engineering and Computational Technologies (ICIEECT)*, April 2017, pp. 1–6.
- [157] P. Hurtik and N. Madrid, "Bilinear interpolation over fuzzified images: Enlargement," in *2015 IEEE International Conference on Fuzzy Systems (FUZZ-IEEE)*, Aug 2015, pp. 1–8.
- [158] Y. Sa, "Improved bilinear interpolation method for image fast processing," in *2014 7th International Conference on Intelligent Computation Technology and Automation*, Oct 2014, pp. 308–311.
- [159] D. Zhou, X. Shen, and W. Dong, "Image zooming using directional cubic convolution interpolation," *IET Image Processing*, vol. 6, no. 6, pp. 627–634, August 2012.
- [160] J. K. Chae, J. Y. Lee, M. H. Lee, J. K. Han, T. Q. Nguyen, and W. Y. Yeo, "Cubic convolution scaler optimized for local property of image data," *IEEE Transactions on Image Processing*, vol. 24, no. 12, pp. 4796–4809, Dec 2015.
- [161] Y.-R. Wang, S.-J. Horng, and H.-C. Chan, "Fast all nearest neighbor algorithms from image processing perspective," in *19th IEEE International Parallel and Distributed Processing Symposium*, April 2005, pp. 9a–9a.
- [162] R. Webster and M. Oliver, *Geostatistics for Environmental Scientists*, ser. Statistics in Practice. Wiley, 2007. [Online]. Available: <https://books.google.co.uk/books?id=WBwSyvIvNY8C>

- [163] L. Jin and A. D. Heap, “A review of spatial interpolation methods for environmental scientists,” Geoscience Australia, Tech. Rep., 2008. [Online]. Available: <https://pdfs.semanticscholar.org/686c/29a81eab59d7f6b7e2c4b060b1184323a122.pdf>
- [164] J. Li and A. D. Heap, “Spatial interpolation methods applied in the environmental sciences: A review,” *Environmental Modelling and Software*, vol. 53, pp. 173 – 189, 2014. [Online]. Available: <http://www.sciencedirect.com/science/article/pii/S1364815213003113>
- [165] P. Burrough and R. McDonnell, *Principles of Geographical Information Systems*, ser. Spatial Information Systems and Geostatistics. Oxford University Press, 2000. [Online]. Available: <https://books.google.co.uk/books?id=PAzBnQEACAAJ>
- [166] D. Shepard, “A two-dimensional interpolation function for irregularly-spaced data,” in *ACM Annual Conference/Annual Meeting*, 1968, pp. 517–524.
- [167] M. Buhmann, *Radial Basis Functions: Theory and Implementations*, ser. Cambridge Monographs on Applied and Computational Mathematics. Cambridge University Press, 2003. [Online]. Available: <https://books.google.co.uk/books?id=TRMf53opzlsC>
- [168] B. J. C. Baxter, “The Interpolation Theory of Radial Basis Functions,” Ph.D. dissertation, Cambridge University, 1992. [Online]. Available: <https://arxiv.org/pdf/1006.2443.pdf>
- [169] G. B. Wright, “Radial Basis Function Interpolation: Numerical and Analytical Development,” Ph.D. dissertation, University of Colorado, 2003. [Online]. Available: <https://amath.colorado.edu/faculty/fornberg/Docs/GradyWrightThesis.pdf>
- [170] ARCGIS, “How Kriging works.” [Online]. Available: <http://pro.arcgis.com/en/pro-app/tool-reference/spatial-analyst/how-kriging-works.htm>

- [171] K. Azpurua, M. and Dos Ramos, “A comparison of spatial interpolation methods for estimation of average electromagnetic field magnitude,” *Progress In Electromagnetics Research*, vol. 14, no. 9, pp. 135–145, 2010.
- [172] W. C. M. van Beers and J. P. C. Kleijnen, “Kriging for interpolation in random simulation,” *The Journal of the Operational Research Society*, vol. 54, no. 3, pp. 255–262, 2003. [Online]. Available: <http://www.palgrave-journals.com/doi/10.1057/palgrave.jors.2601492>
- [173] ARCGIS, “ARCGIS-DESKTOP HELP.” [Online]. Available: REF <http://help.arcgis.com/EN/arcgisdesktop/10.0/help/index.htm>
- [174] W. Schwanghart, “Ordinary Kriging,” 2010. [Online]. Available: <http://www.mathworks.com/matlabcentral/fileexchange/29025-ordinary-kriging>
- [175] A. Chirokov, “Scattered Data Interpolation and Approximation using Radial Base Functions,” 2006. [Online]. Available: <http://uk.mathworks.com/matlabcentral/fileexchange/10056-scattered-data-interpolation-and-approximation-using-radial-base-functions>
- [176] H. Wackernagel, *Multivariate geostatistics : An introduction with applications*. New York: Springer, 2003.

# **Appendices**

# Appendix A

## Irradiance Measurements at HSSMI and 5GRC

In Figure A.1, indoor irradiance values measured at HSSMI main office space is presented. The main office space has one out of four sides open to external lighting. It is evident from the magnitude of indoor irradiance values that the predominant source of indoor light at HSSMI was via fluorescent tubes<sup>1</sup>. The average irradiance and standard deviation of the measurement was  $1.53 \pm 0.10 \text{ W/m}^2$ . This measurement at was taken on the 11<sup>th</sup> of May, 2015, 3 meters away from the glass windows. The weather on that day was sunny at mid day and overcast in the early and late hours of the day.

---

<sup>1</sup>Outdoor values were two orders more



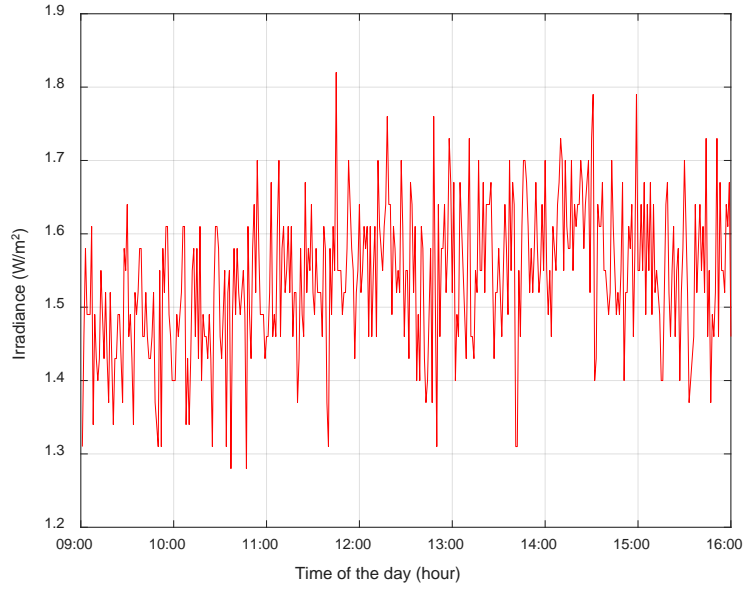


Figure A.1: Irradiance measurement at HSSMI main office

Additional measurements were also taken at the 5G Research Center, Loughborough University on the 8<sup>th</sup> of December, 2014. The average irradiance and standard deviation at the center was  $1.96 \pm 0.59 \text{ W/m}^2$ . In Figure A.2, the irradiance from the center is presented. Rapid fluctuations can be observed in the Figure, this was due to the movement of cloud. The measurement setup was placed on a desk near the window and the dimensions of the measurement site were 11 m by 4 m.

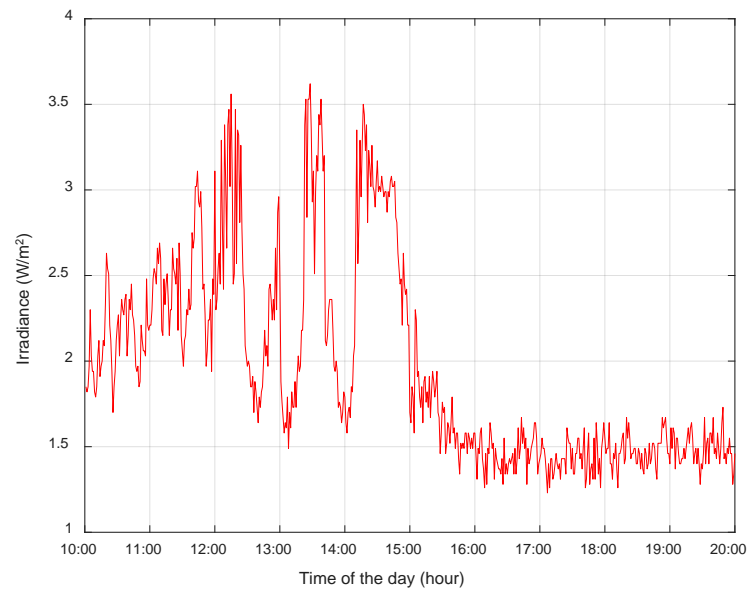


Figure A.2: Irradiance measurement at 5GRC, Loughborough University

## Appendix B

# Horizontal and Vertical Polarization Power Density Measurements

This appendix presents the horizontal and vertical components of the input RF power density measured at the DEP. In Figure B.1 and Figure B.2, the average and max-hold measurements at Location 1 are shown.

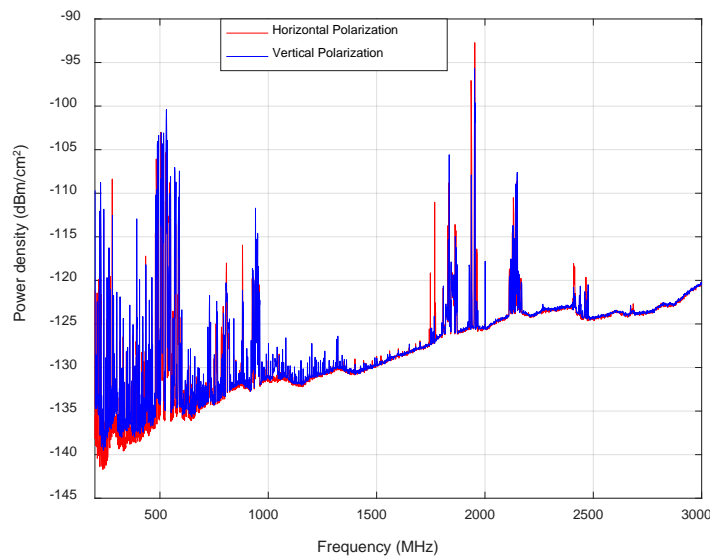


Figure B.1: Horizontal and vertical polarization measurements for average mode at the DEP (Location 1)

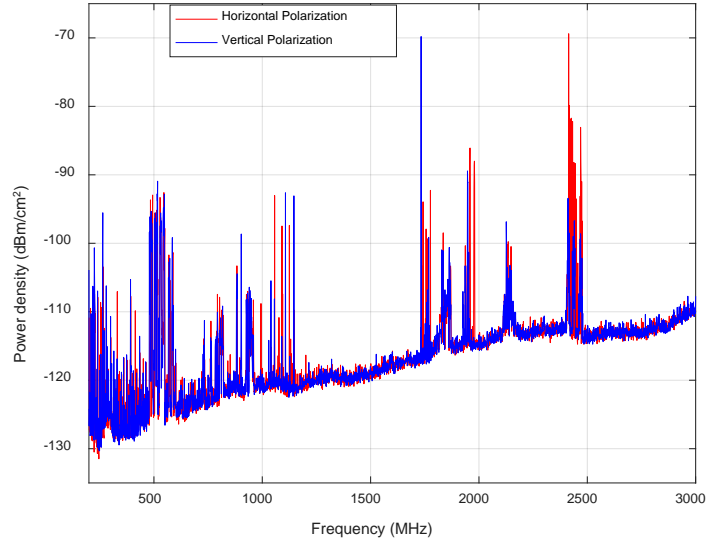


Figure B.2: Horizontal and vertical polarization measurements for max-hold at the DEP (Location 1)

In Figures B.3 and B.4, the average and max-hold measurements at Location 2 are shown.

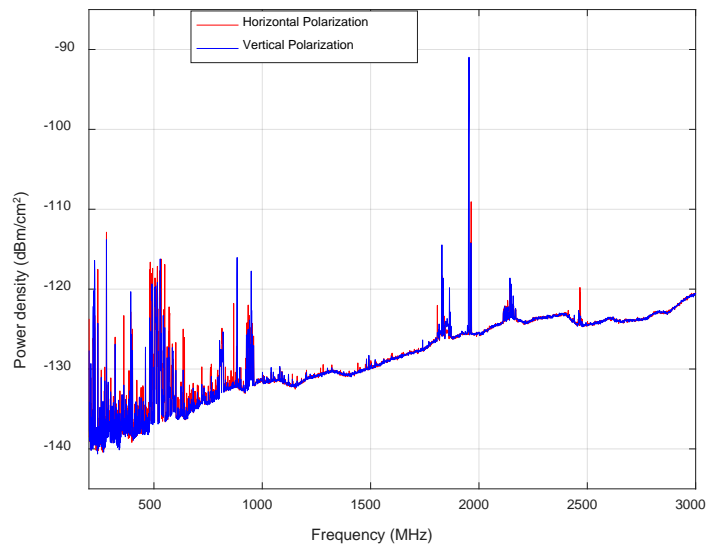


Figure B.3: Horizontal and vertical polarization measurements for average mode at the DEP (Location 2)

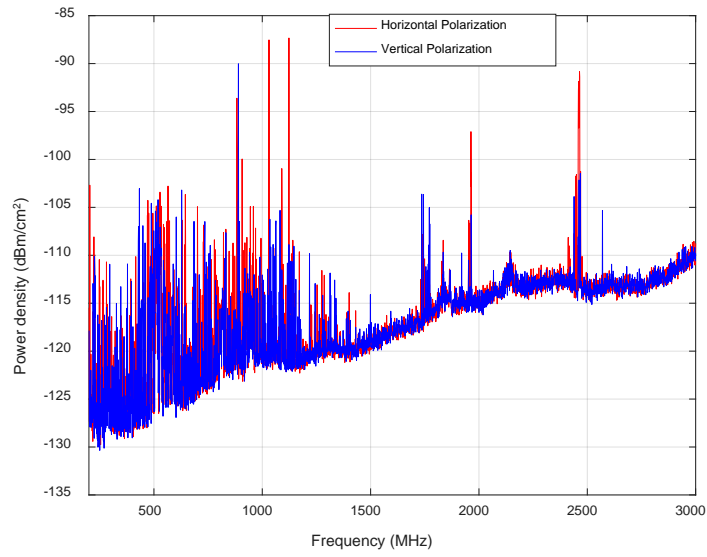


Figure B.4: Horizontal and vertical polarization measurements for max-hold at the DEP (Location 2)

In Figures B.5 and B.6, the average and max-hold measurements at Location 3 are shown.

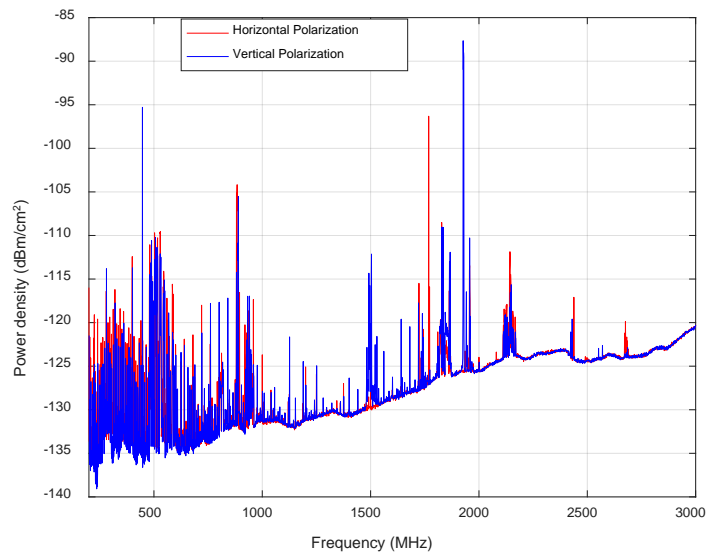


Figure B.5: Horizontal and vertical polarization measurements for average mode at the DEP (Location 3)

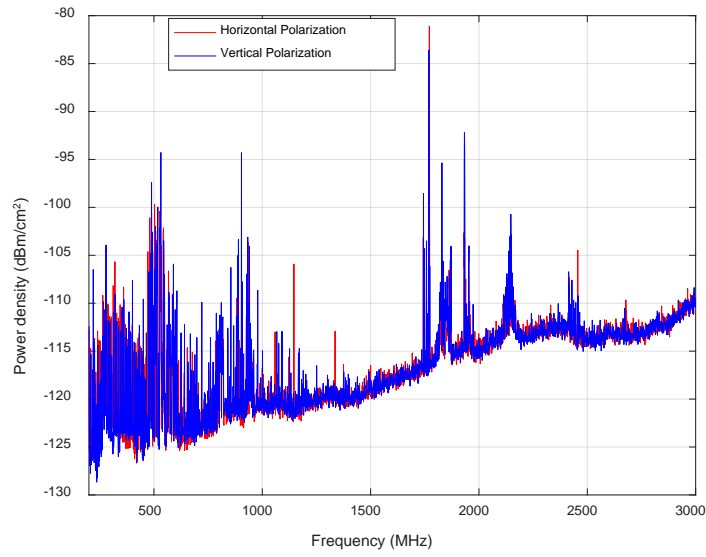


Figure B.6: Horizontal and vertical polarization measurements for max-hold at the DEP (Location 3)

In Figures B.7 and B.8, the average and max-hold measurements at Location 4 are shown.

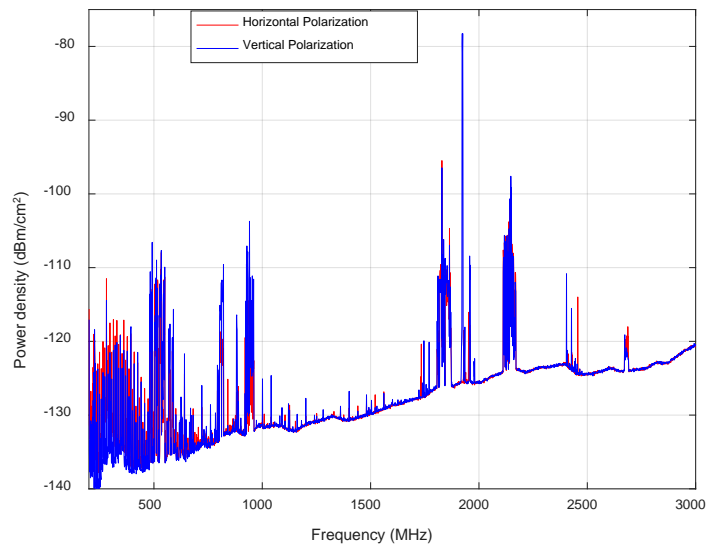


Figure B.7: Horizontal and vertical polarization measurements for average mode at the DEP (Location 4)

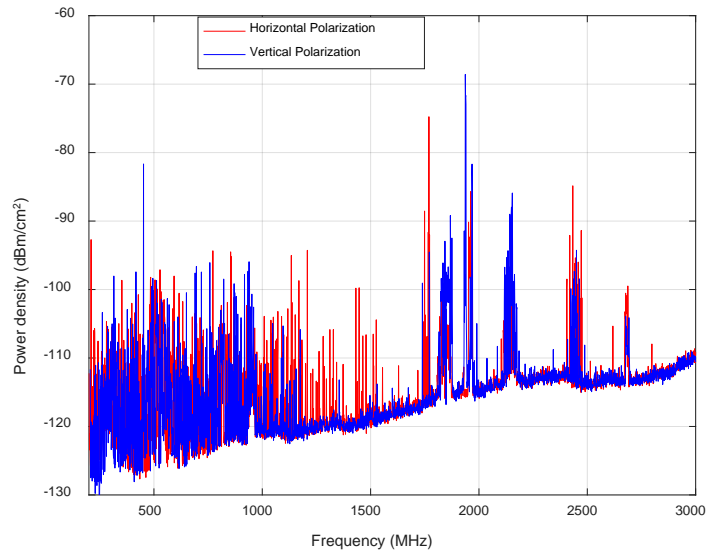


Figure B.8: Horizontal and vertical polarization measurements for max-hold at the DEP (Location 4)

In Figures B.9 and B.10, the average and max-hold measurements at Location 5 are shown.

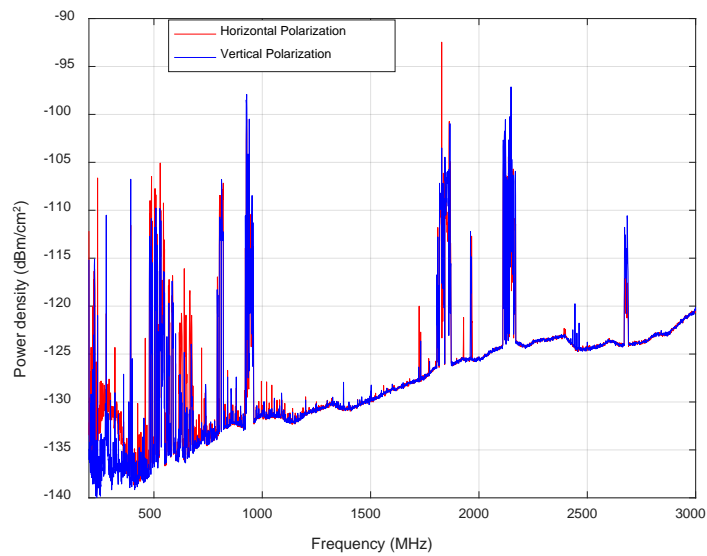


Figure B.9: Horizontal and vertical polarization measurements for average mode at the DEP (Location 5)

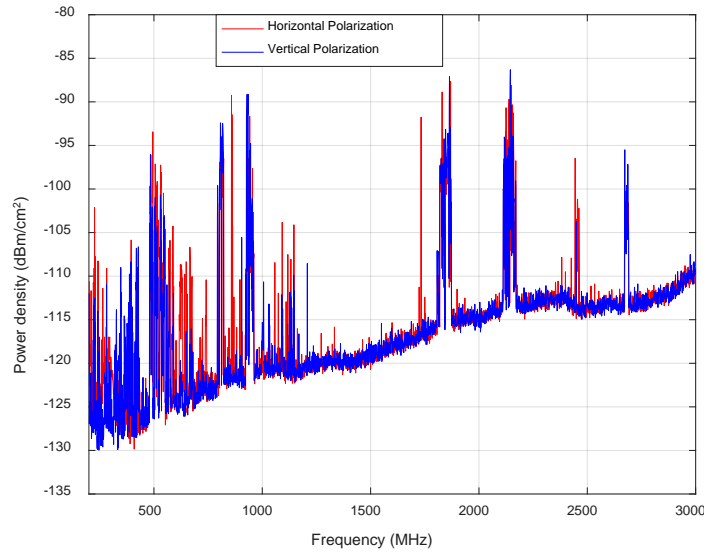


Figure B.10: Horizontal and vertical polarization measurements for max-hold at the DEP (Location 5)

Supplementary RF power density measurements were carried out at HSSMI and CEME reception area. Both measurement locations are in the CEME building, with the reception area on the ground floor and HSSMI on the second floor. The measurements at the CEME reception was taken close to the Cafe during lunch time, while the measurement at HSSMI was taken on the same day one hour apart. At both locations, the antenna was facing the entrance. The front of the CEME building is made with see through reinforced glass. In Figures B.11 to B.14, the max-hold and average power density results for horizontal and vertical polarization at CEME and HSSMI are presented.



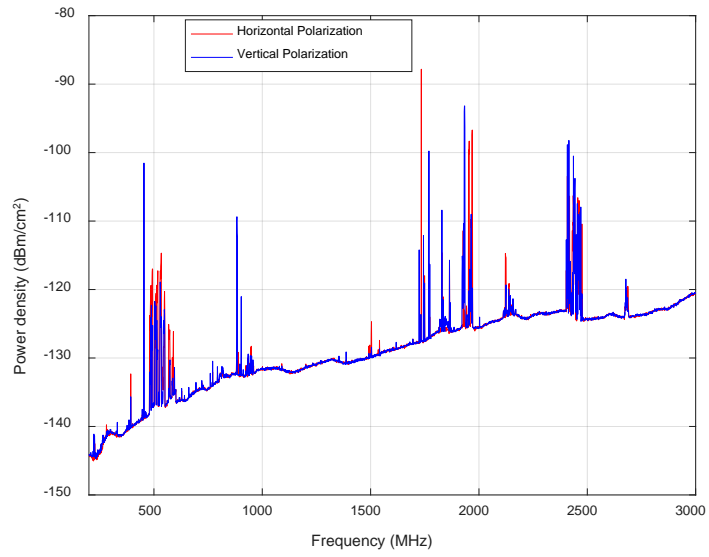


Figure B.11: Horizontal and vertical polarization measurements for average mode at CEME reception

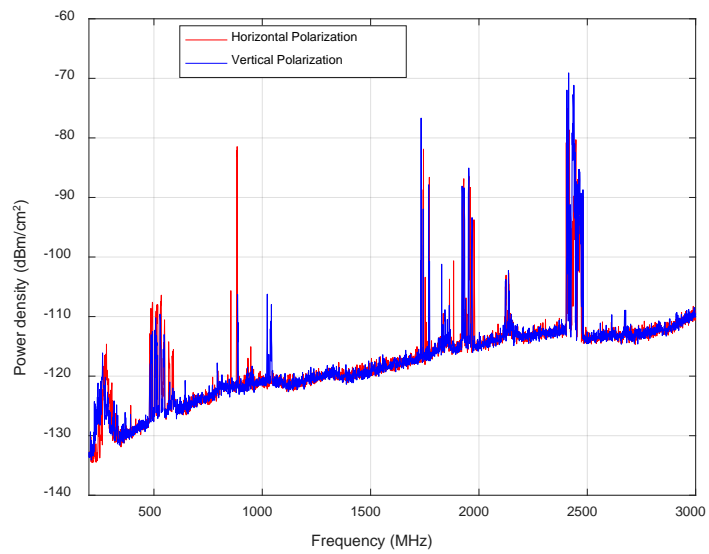


Figure B.12: Horizontal and vertical polarization measurements for max-hold at CEME reception

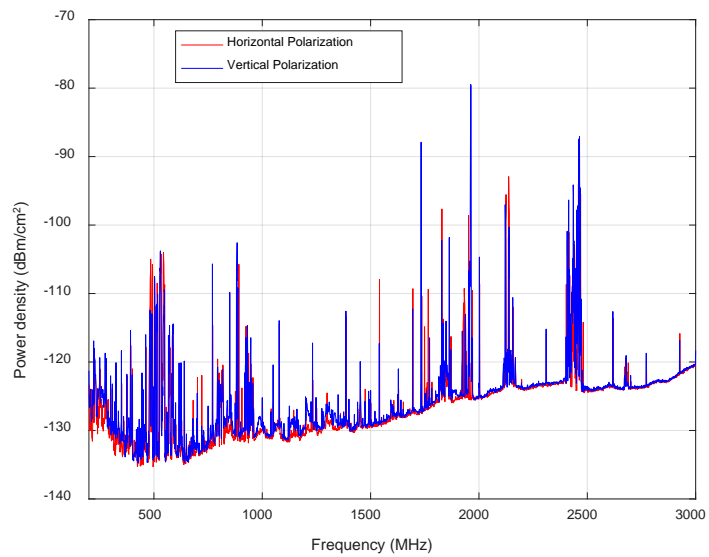


Figure B.13: Horizontal and vertical polarization measurements for average mode at CEME reception

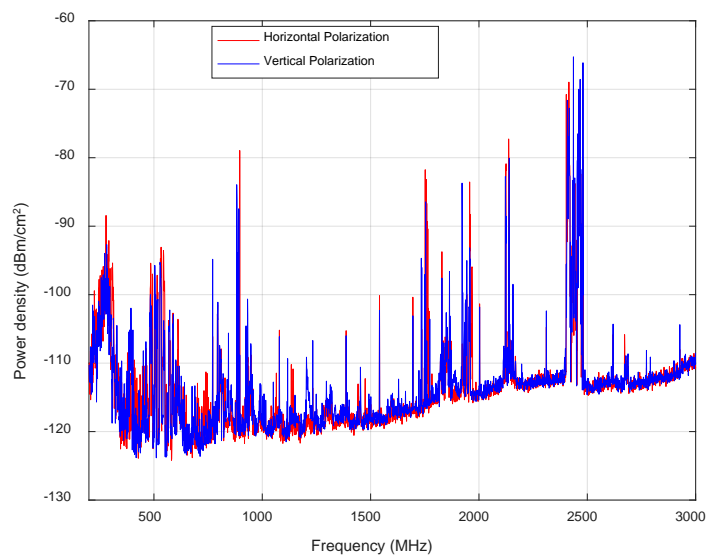


Figure B.14: Horizontal and vertical polarization measurements for max-hold at CEME reception

# Appendix C

## Measurement Cable and Antenna Parameters

This appendix shows the antenna gain and factors of the EM 6116 omni-directional antenna.

Table C.1: Electro-Metrics EM6116

Frequency (MHz)	Antenna Factor (dB/m)	Gain (dBi)
2000	34.05	2.22
2500	37.00	1.21
3000	38.83	0.96
3500	38.86	2.27
4000	38.51	3.78
4500	40.39	2.92
5000	41.07	3.16
5500	41.63	3.42
6000	42.76	3.05
6500	43.74	2.76
7000	43.44	3.71
7500	43.81	3.94
8000	44.24	4.07
8500	45.07	3.76
9000	46.71	2.62
9500	46.79	23.01
10000	47.85	2.40

In Figure C.1 to C.3, the frequency loss graphs for the three MW cables used are presented.

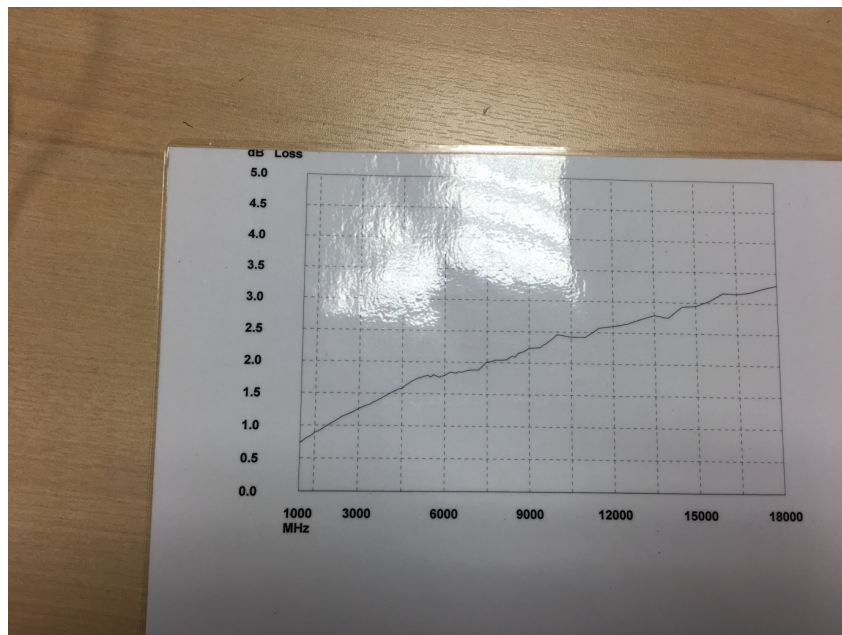


Figure C.1: Frequency vs dB loss for 3 m MW cable

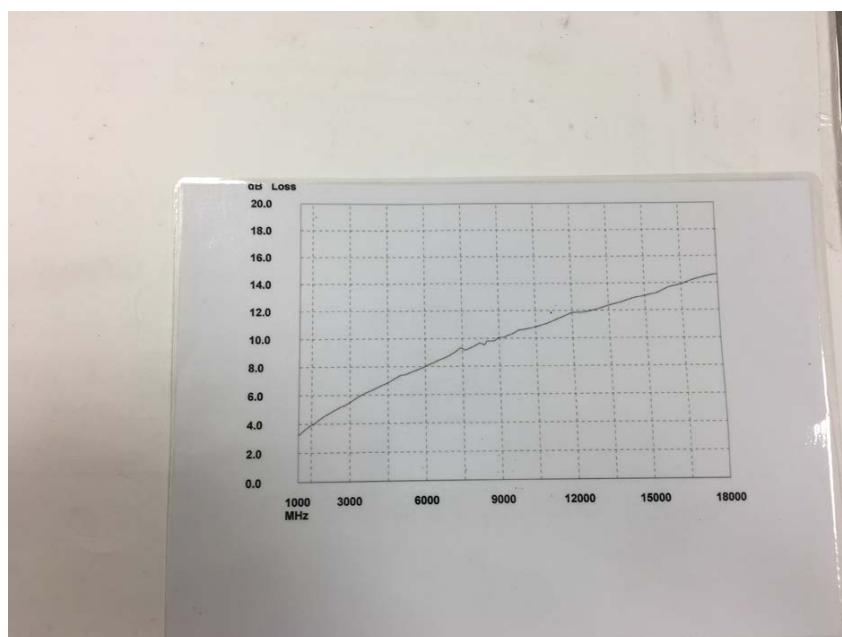


Figure C.2: Frequency vs dB loss for 13 m MW cable

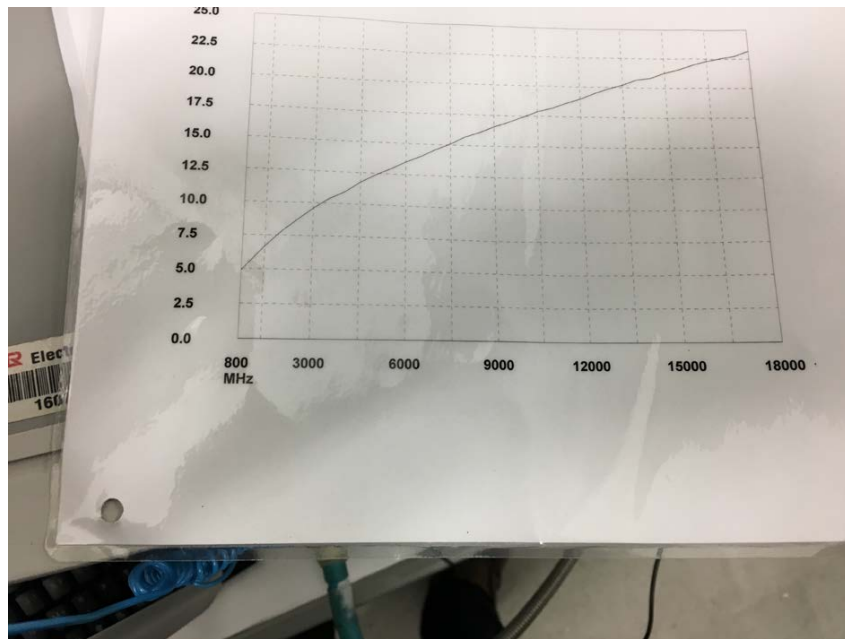


Figure C.3: Frequency vs dB loss for 20 m MW cable

# Appendix D

## Inventory of Loughborough University Machine Workshop

This appendix lists the inventory present in the Loughborough University workshop in no particular order.

Table D.1: Workshop inventory

Label	Description
D	Edwards 3.25mm Truecut
E	M300 Harisson
F	Colchester Student
G	Colchester Triump
I	Startite 24-T-1Q
H	Metal saw
T2,T3	Wooden shelf 2m high
T4	Wooden table
C3	PEC shelf 2m high
M,O	Electrical motors
C0	PEC shelf (2.2m high) with tools
B1	SMX SLV Machine tool
A1	Cut 20P
A2	Haas milling machine
C2	PEC boxes(0.5m high)
P	Pillars
T1	Work bench with tools

## Appendix E

# Power Delay Profiles for Computing Delay Spread

This appendix presents the individual power delay profiles measured and modelled at the receiver locations. These profiles are imported to MATLAB for time dispersion computation. The measurement profiles are displayed up to 600 ns, as this exceeds the delay in large factory environments.

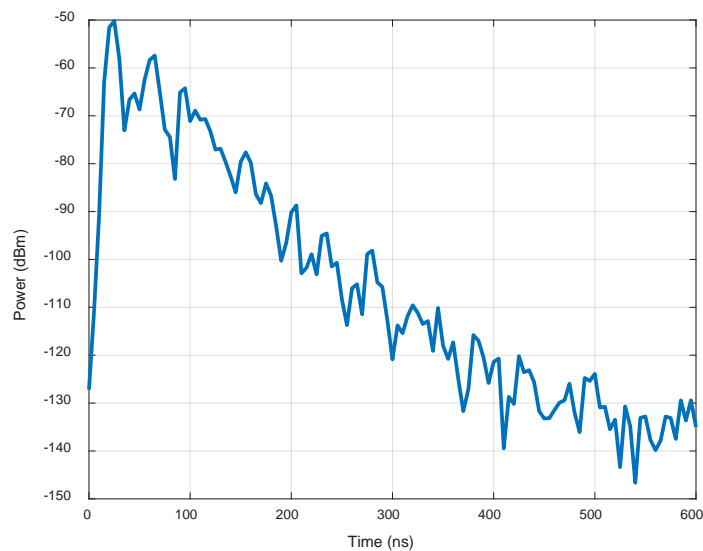


Figure E.1: Measurement power delay profile at receiver location  $L_1$

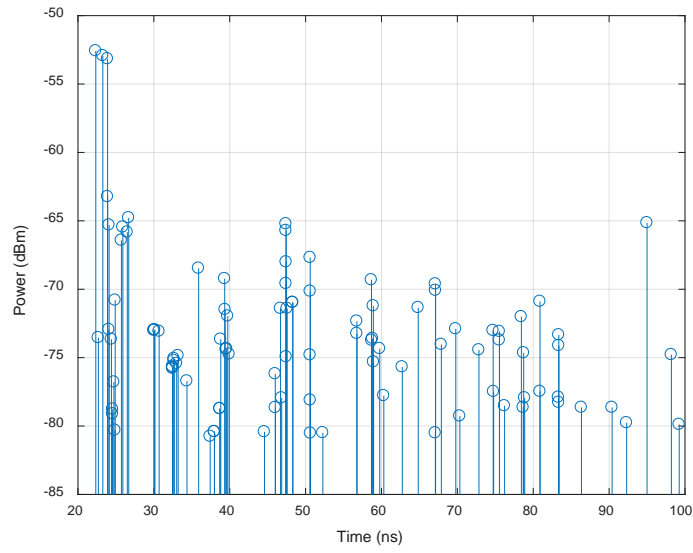


Figure E.2: Ray tracing profile at receiver location  $L_1$

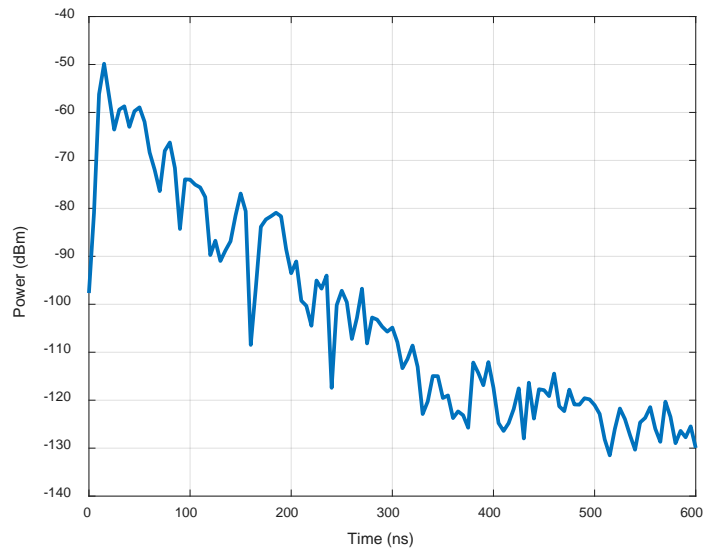


Figure E.3: Measurement power delay profile at receiver location  $L_2$



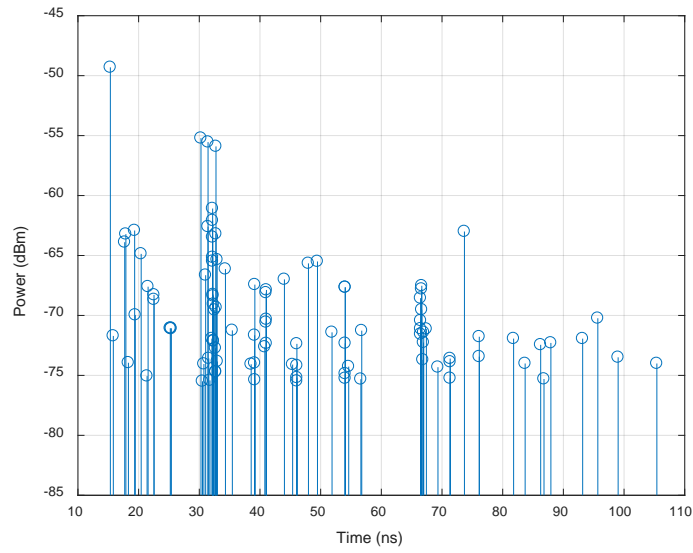


Figure E.4: Ray tracing profile at receiver location  $L_2$

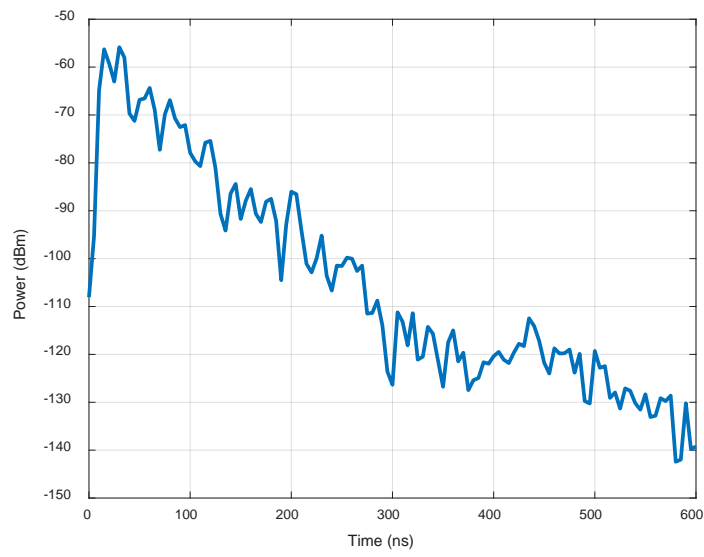


Figure E.5: Measurement power delay profile at receiver location  $L_3$

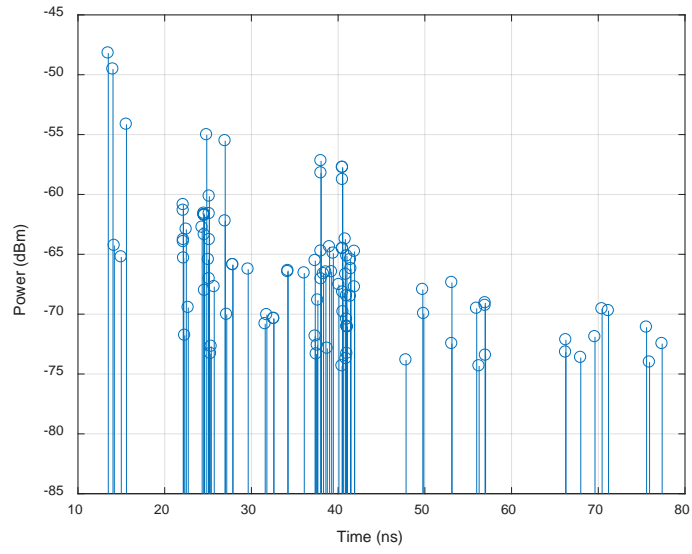


Figure E.6: Ray tracing profile at receiver location  $L_3$

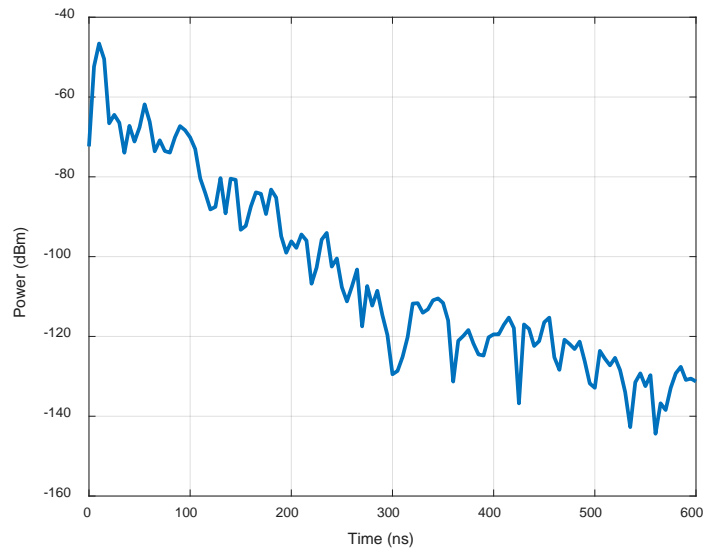


Figure E.7: Measurement power delay profile at receiver location  $L_4$

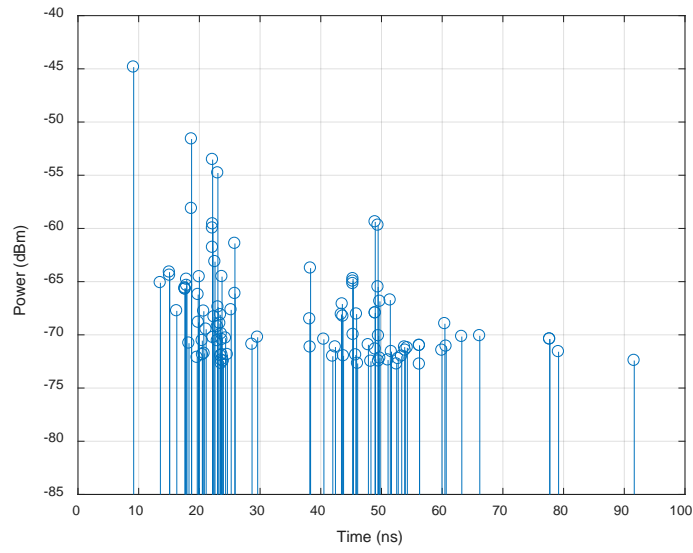


Figure E.8: Ray tracing profile at receiver location  $L_4$

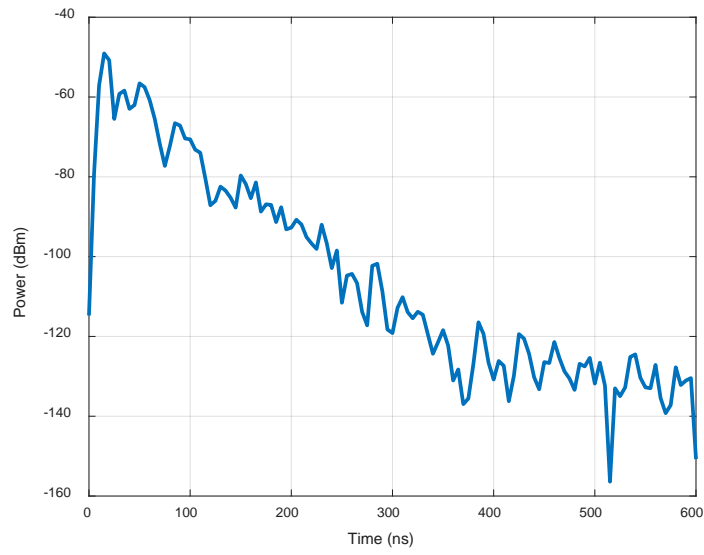


Figure E.9: Measurement power delay profile at receiver location  $L_5$

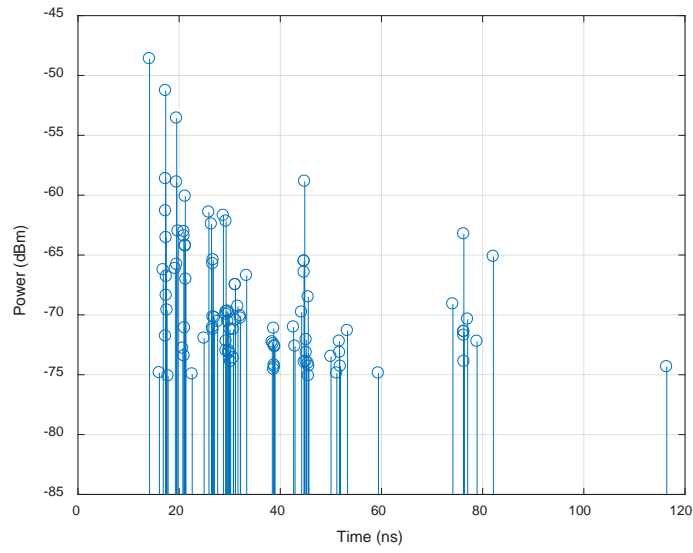


Figure E.10: Ray tracing profile at receiver location  $L_5$

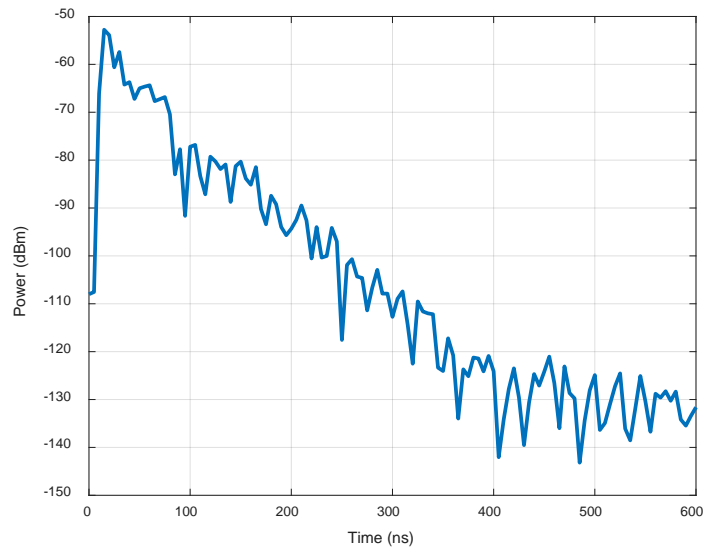


Figure E.11: Measurement power delay profile at receiver location  $L_6$

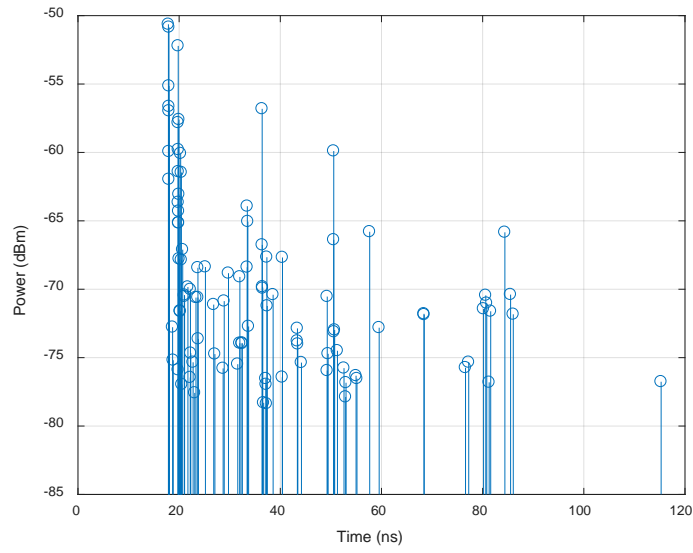


Figure E.12: Ray tracing profile at receiver location  $L_6$

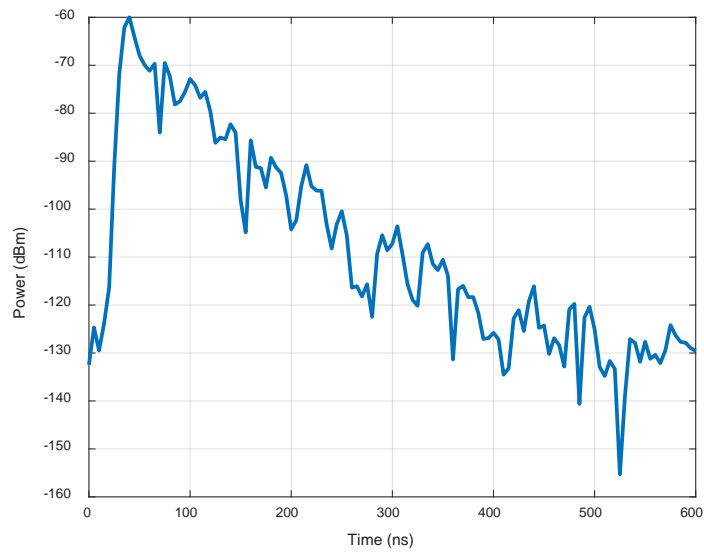


Figure E.13: Measurement power delay profile at receiver location  $N_1$

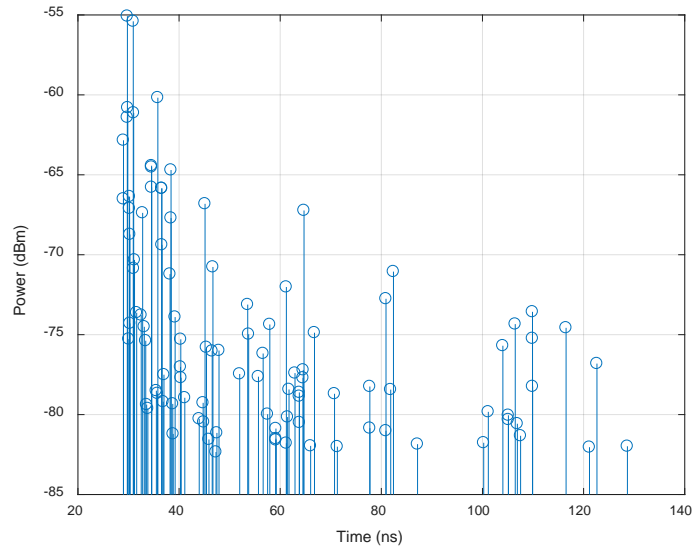


Figure E.14: Ray tracing profile at receiver location  $N_1$

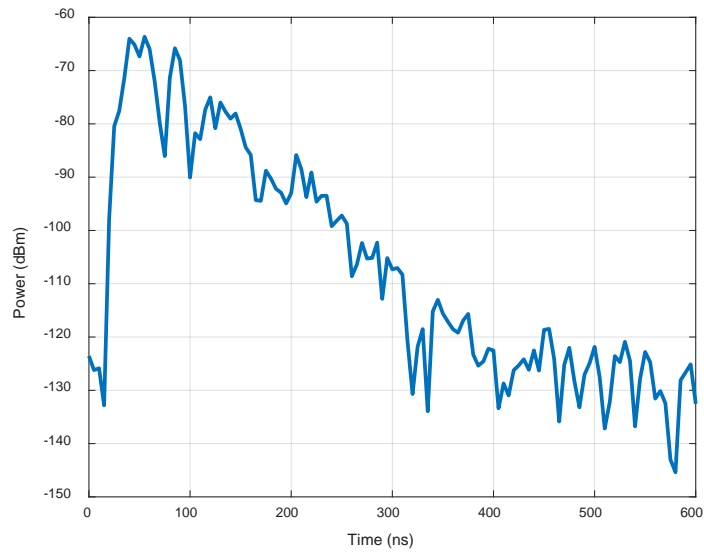


Figure E.15: Measurement power delay profile at receiver location  $N_2$

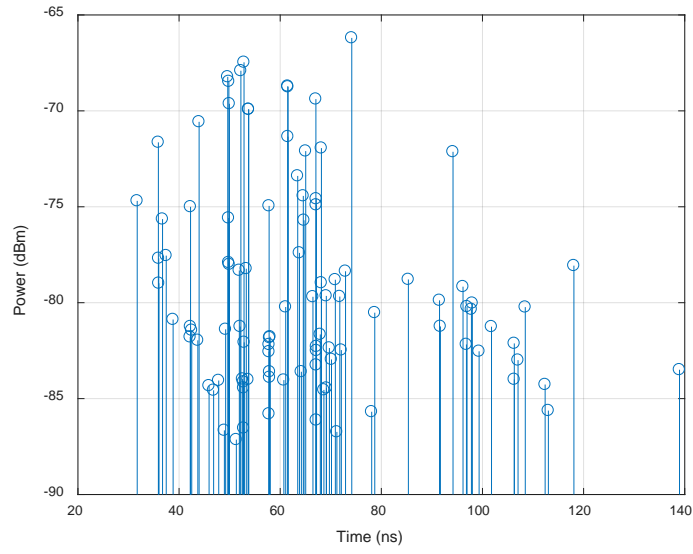


Figure E.16: Ray tracing profile at receiver location  $N_2$

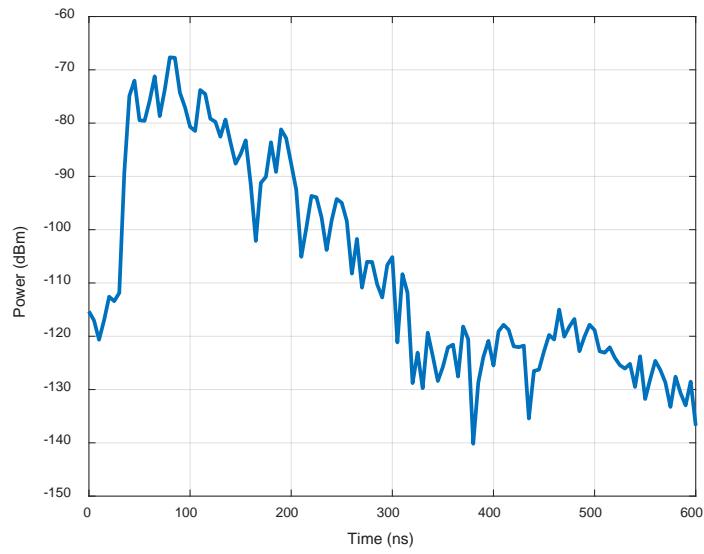


Figure E.17: Measurement power delay profile at receiver location  $N_3$

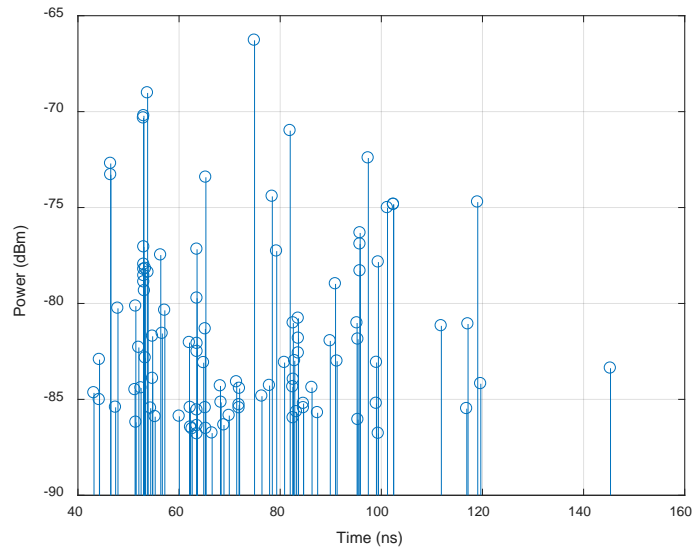


Figure E.18: Ray tracing profile at receiver location  $N_3$

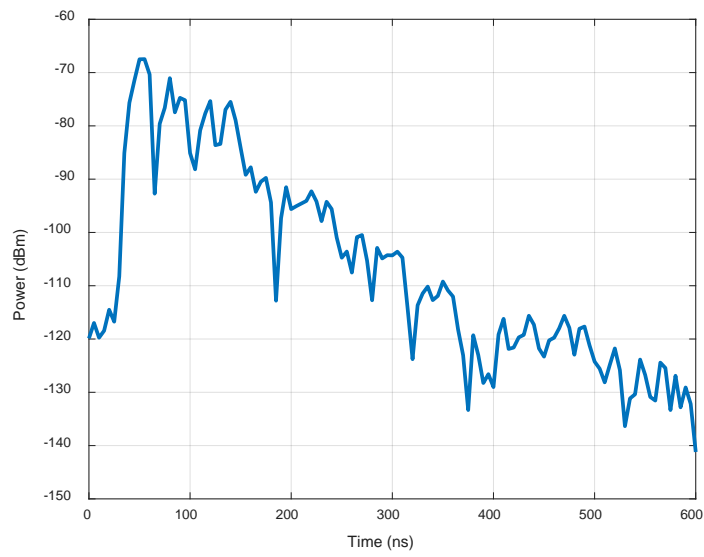


Figure E.19: Measurement power delay profile at receiver location  $N_4$



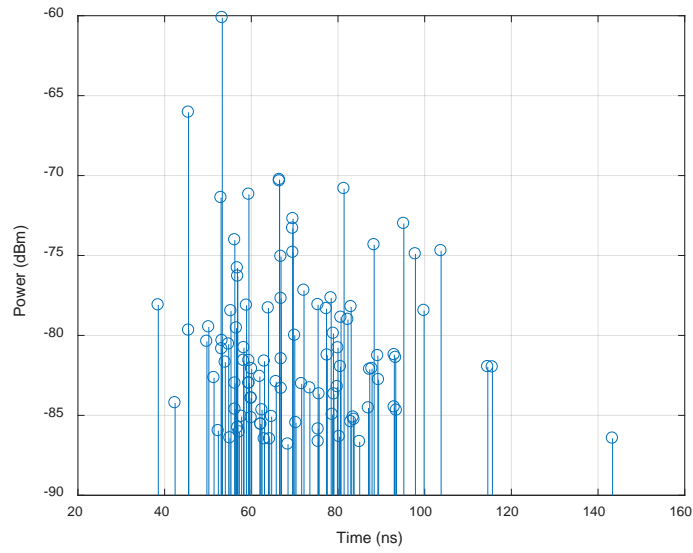


Figure E.20: Ray tracing profile at receiver location  $N_4$

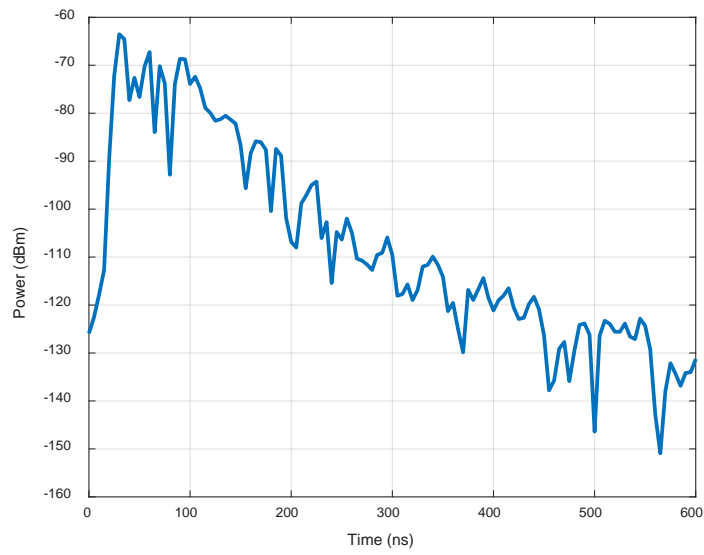


Figure E.21: Measurement power delay profile at receiver location  $N_5$

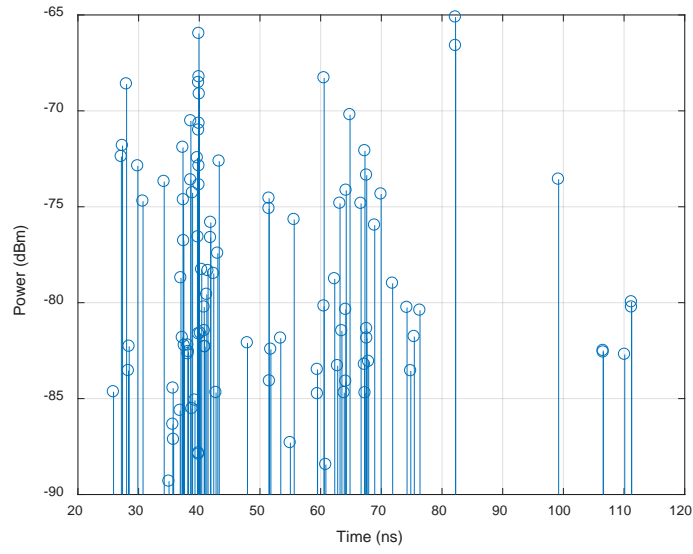


Figure E.22: Ray tracing profile at receiver location  $N_5$

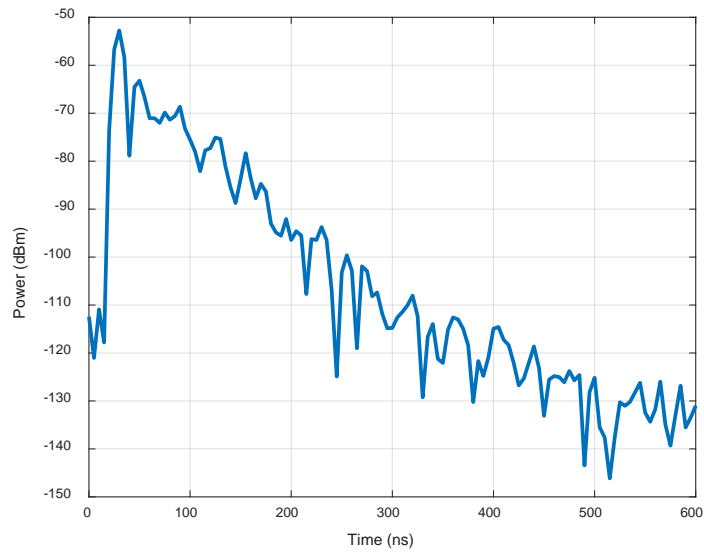


Figure E.23: Measurement power delay profile at receiver location  $N_6$

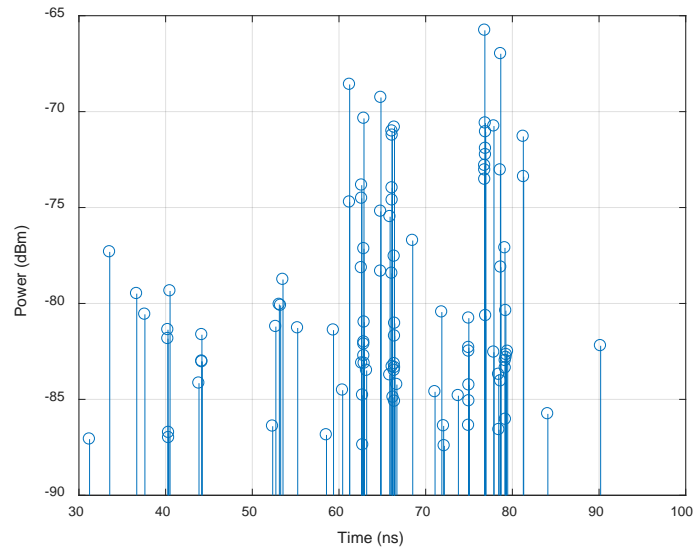


Figure E.24: Ray tracing profile at receiver location  $N_6$

## **Appendix F**

### **APDPs Obtained from Virtual Arrays for Fractal Overlay Model**

This appendix shows the APDPs obtained from the virtual arrays at 2.4 and 60 GHz. The APDP figures also highlight the visually identified clusters (in black lines) through which the S-V model parameters were obtained. The dark lines only depict the clusters and do not represent the slope of the regression line.

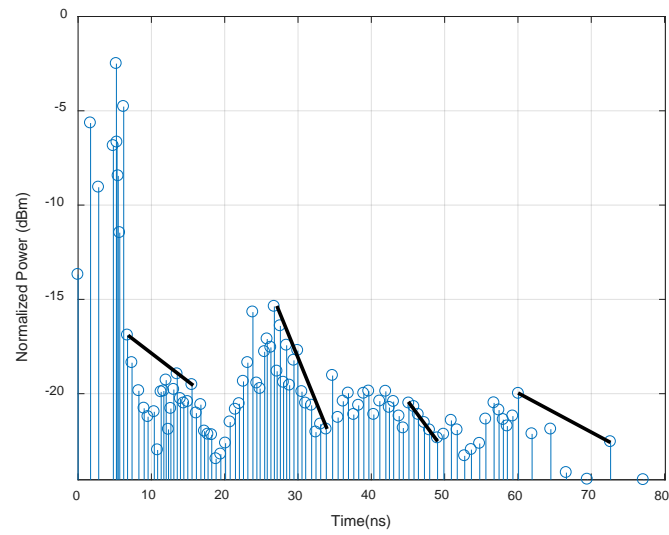


Figure F.1: APDP at receiver location 1 (2.4 GHz).

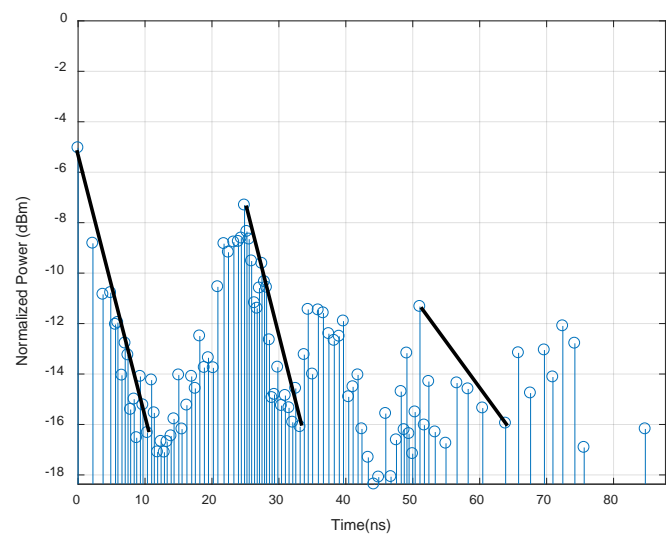


Figure F.2: APDP at receiver location 2 (2.4 GHz).

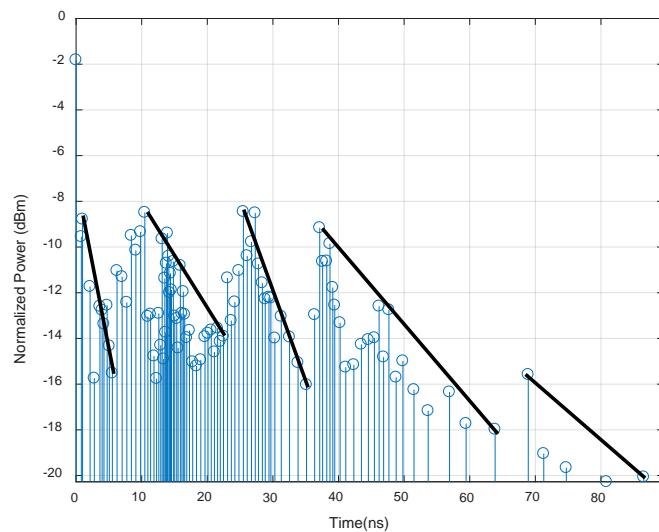


Figure F.3: APDP at receiver location 3 (2.4 GHz).

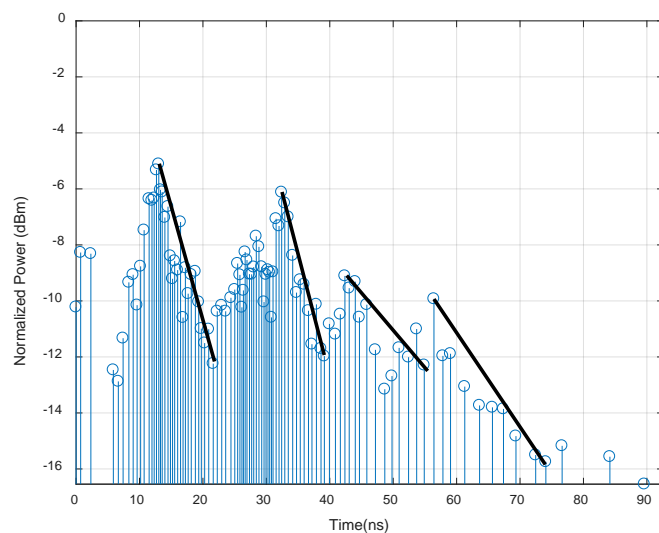


Figure F.4: APDP at receiver location 4 (2.4 GHz).

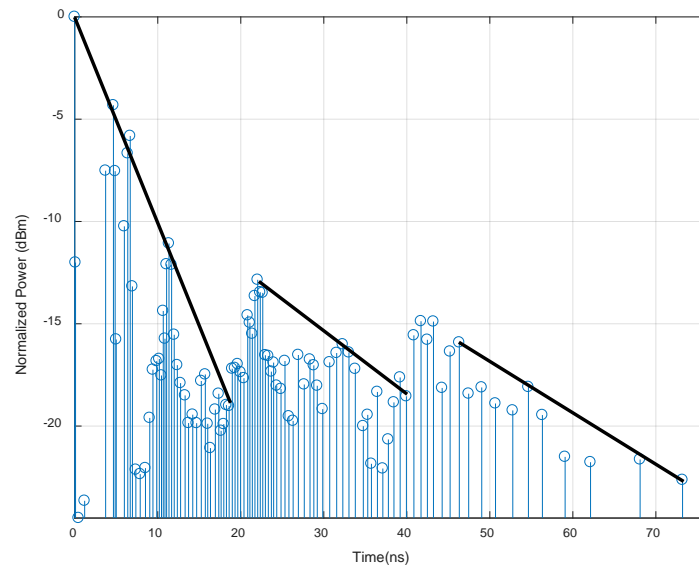


Figure F.5: APDP at receiver location 5 (2.4 GHz).

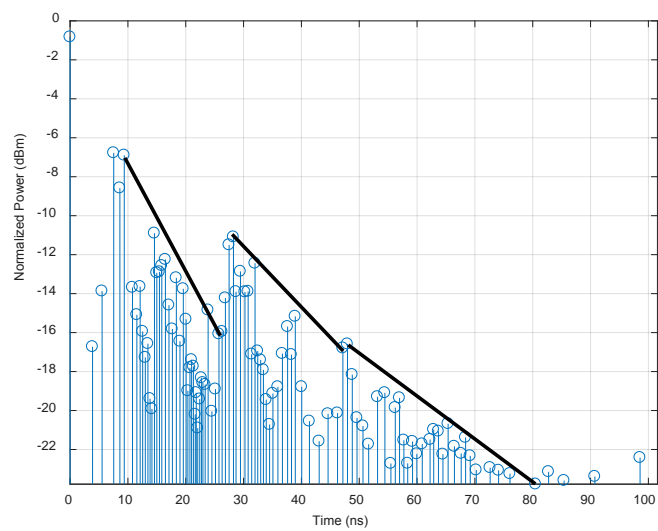


Figure F.6: APDP at receiver location 6 (2.4 GHz).

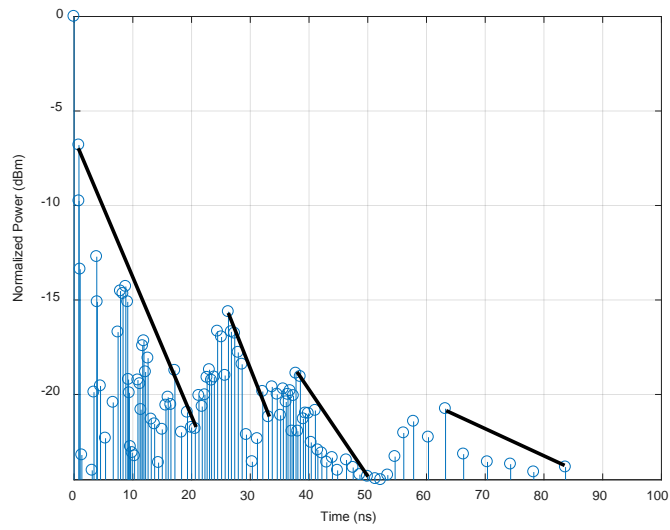


Figure F.7: APDP at receiver location 7 (2.4 GHz).

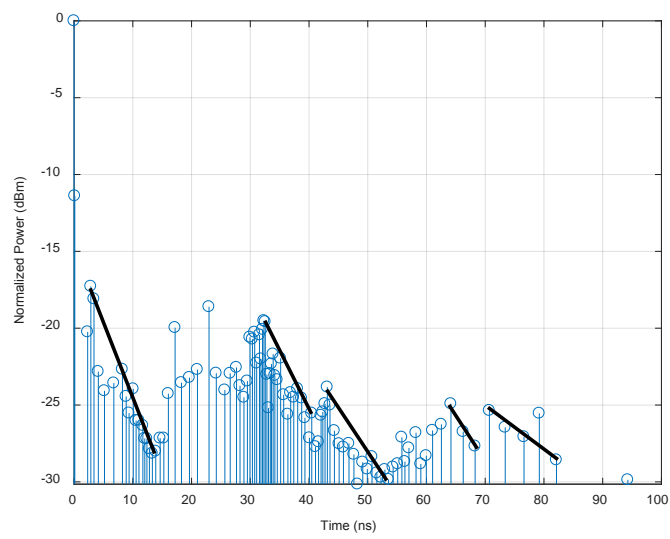


Figure F.8: APDP at receiver location 8 (2.4 GHz).



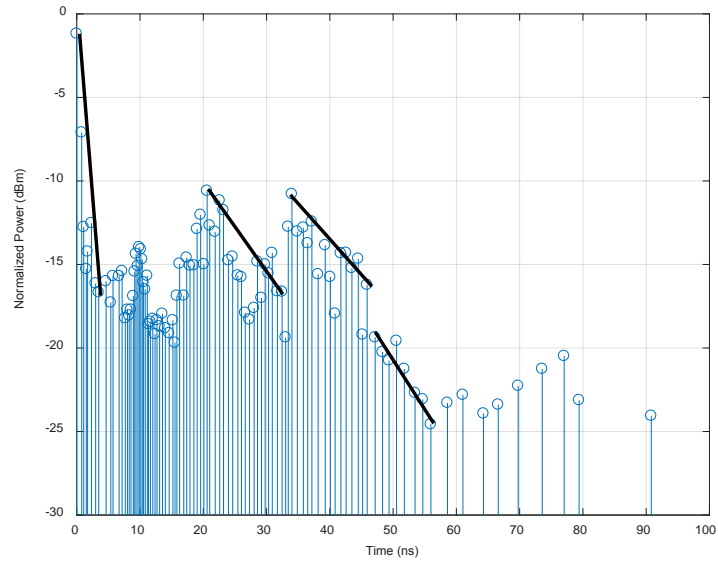


Figure F.9: APDP at receiver location 9 (2.4 GHz).

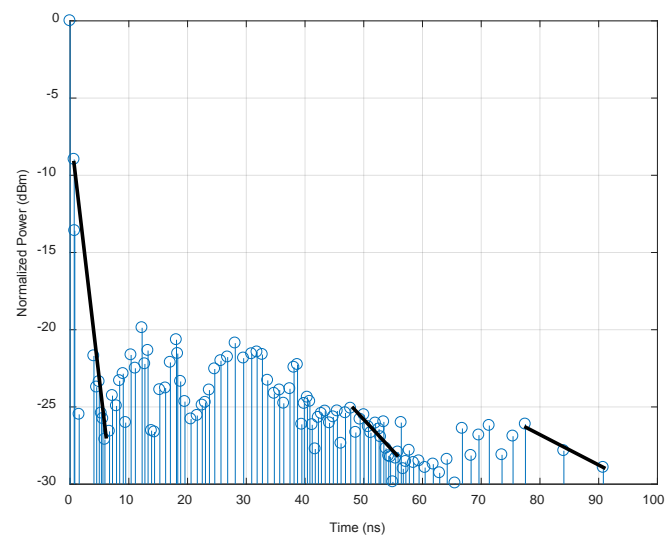


Figure F.10: APDP at receiver location 10 (2.4 GHz).

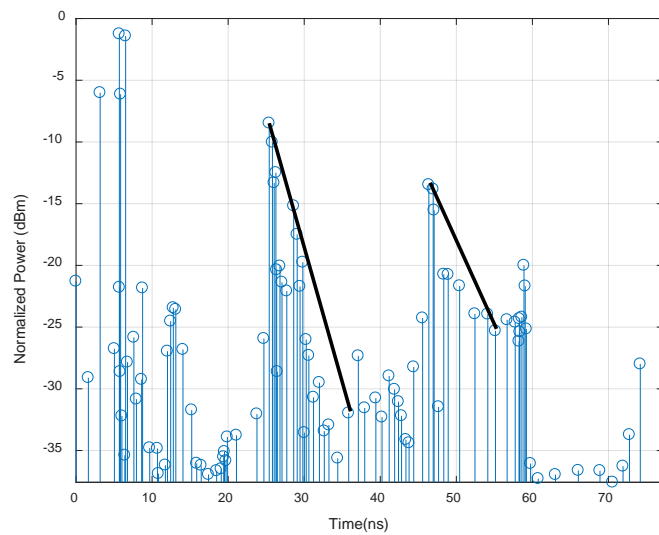


Figure F.11: APDP at receiver location 1 (60 GHz).

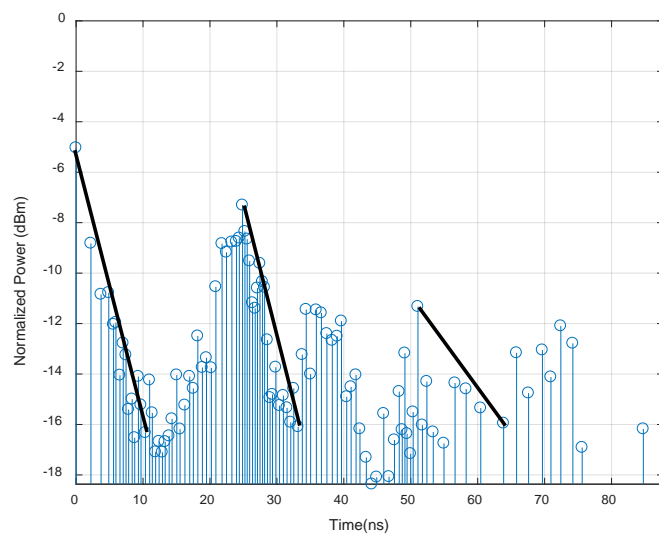


Figure F.12: APDP at receiver location 2 (60 GHz).

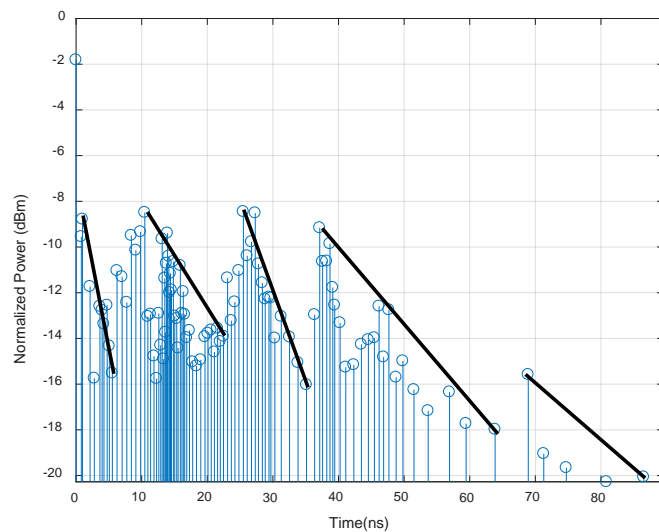


Figure F.13: APDP at receiver location 3 (60 GHz).

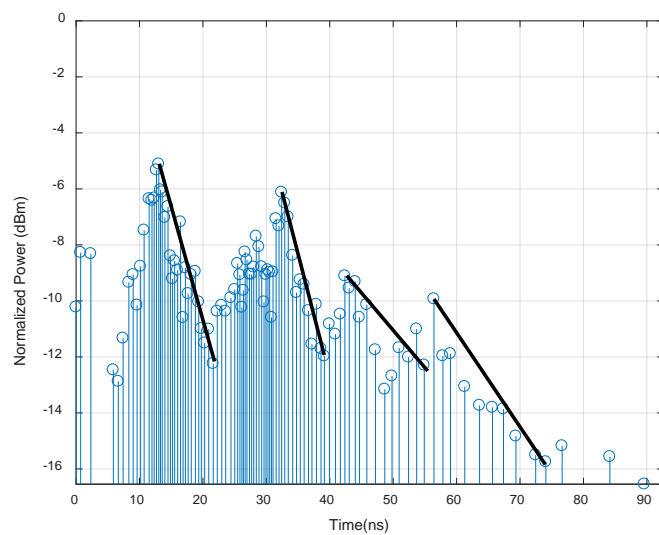


Figure F.14: APDP at receiver location 4 (60 GHz).

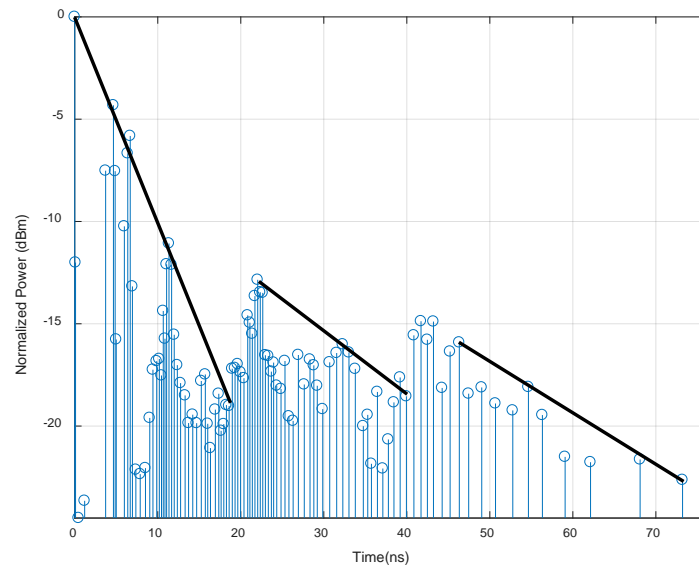


Figure F.15: APDP at receiver location 5 (60 GHz).

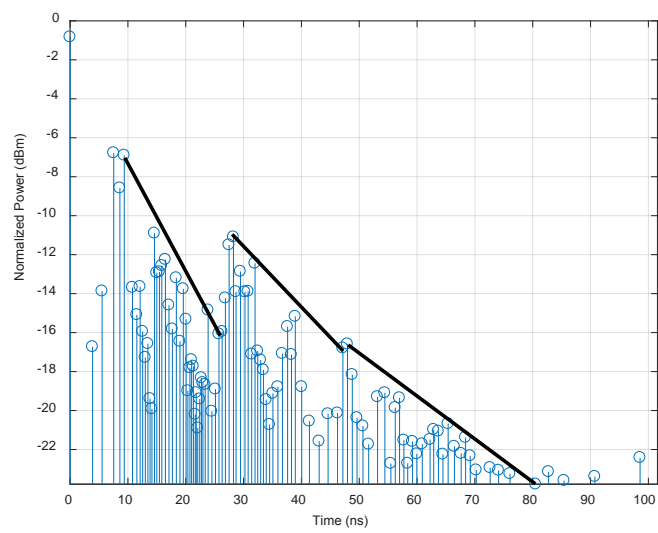


Figure F.16: APDP at receiver location 6 (60 GHz).

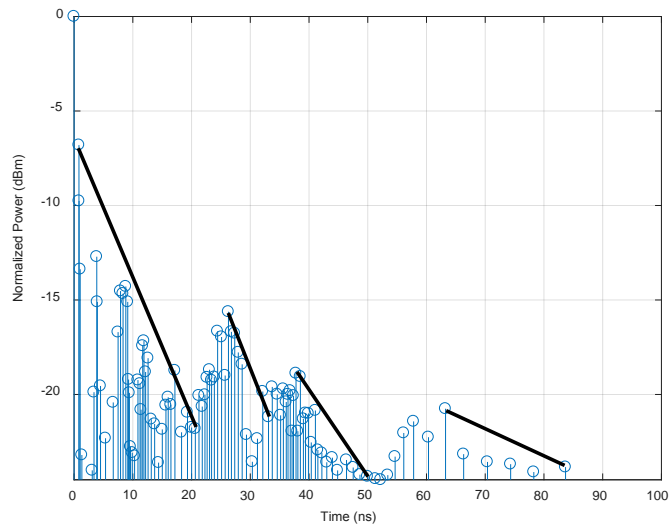


Figure F.17: APDP at receiver location 7 (60 GHz).

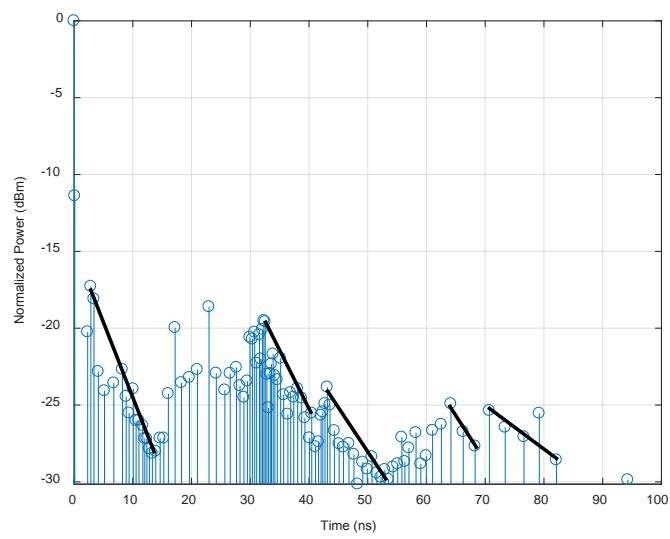


Figure F.18: APDP at receiver location 8 (60 GHz).

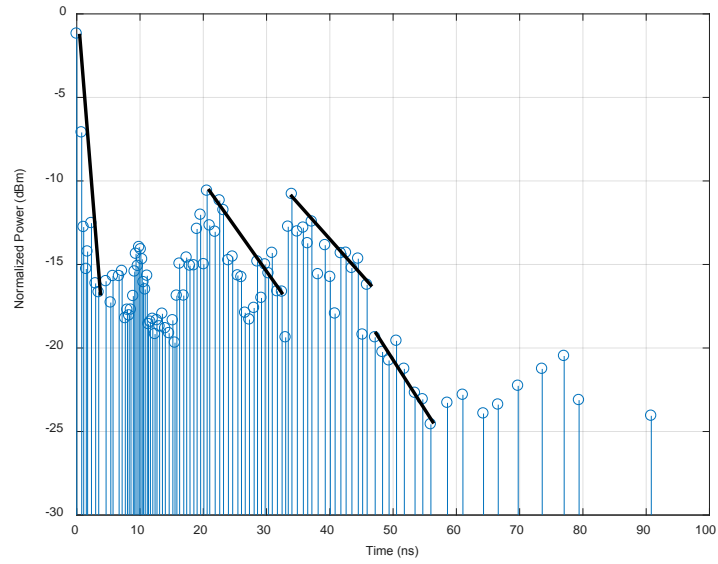


Figure F.19: APDP at receiver location 9 (60 GHz).

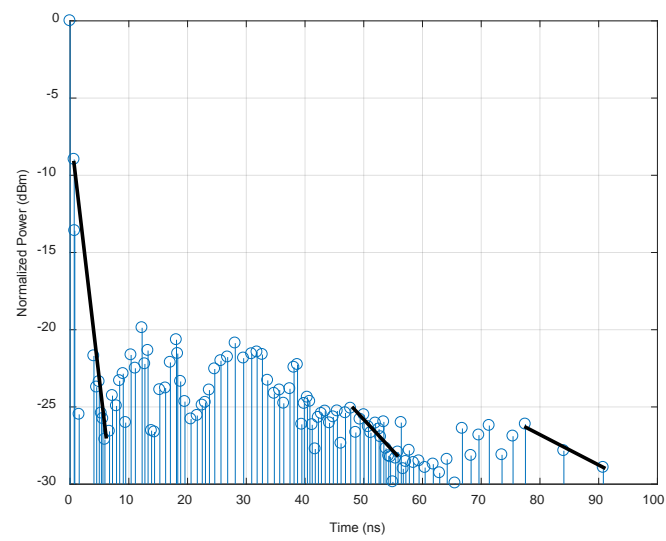


Figure F.20: APDP at receiver location 10 (60 GHz).